Fall 2019

Study of Amorphous Boron Carbide and Hydrogenated Boron Carbide Materials Using Molecular Dynamics and Hybrid Reverse Monte Carlo

Rajan Khadka
Missouri State University, Rajan882@live.missouristate.edu

STUDY OF AMORPHOUS BORON CARBIDE AND HYDROGENATED BORON CARBIDE MATERIALS USING MOLECULAR DYNAMICS AND HYBRID REVERSE MONTE CARLO

A Master's Thesis

Presented to

The Graduate College of

Missouri State University

In Partial Fulfillment

Of the Requirements for the Degree

Master of Science, Materials Science

By

Rajan Khadka

December 2019

STUDY OF AMORPHOUS BORON CARBIDE AND HYDROGENATED BORON CARBIDE MATERIALS USING MOLECULAR DYNAMICS AND HYBRID REVERSE MONTE CARLO

Physics, Astronomy and Materials Science

Missouri State University, December 2019

Master of Science

Rajan Khadka

ABSTRACT

We present a computational study of amorphous boron carbide (a-B_xC) models using Molecular Dynamics (MD) studied with Stillinger-Weber (SW) and ReaxFF potential. The atomic structure factor (*S(Q)*), radial distribution function (RDF) and bond lengths comparison with other experimental and *ab initio* models shows that a random arrangement of icosahedra (B_{12}, $B_{11}C$) interconnected by chains (CCC, CBC) are present in a-B_xC. Afterward, Hybrid Reverse Monte Carlo (HRMC) technique is used to recreate a-B_xC structures. The existing SW potential parameters of Boron are optimized for the α-rhombohedral (Icosahedral B_{12}) boron structure using potential energy minimization and incorporated into HRMC. The a-B_xC modeled from MD simulation is used as a sample for experimental input parameters like RDF, *S(Q)*, coordination environments (CO), bond angle distribution (*B(θ)*) and bond length (BL) to guide initial configuration and simulation in HRMC. An accurate agreement of structural information between HRMC and MD generated models was found. Also, we have modeled the amorphous hydrogenated boron carbide (a-$B_xC:H_y$) material using MD simulation to determine the structural characteristics of experimentally prepared a-$B_xC:H_y$ using plasma-enhanced chemical vapor deposition (PECVD) technique. The simulated a-$B_xC:H_y$ models are characterized for RDF, *S(Q)*, *B(θ)*, CO, Structural units (SU), and CO information. The key structural features of a-$B_xC:H_y$ is mapped out with the density, hydrogen concentration and the stoichiometry of experimentally prepared films prepared using single-source precursor *ortho*-carborane.

KEYWORDS: α-rhombohedral boron, amorphous boron carbide, hydrogenated boron carbide, molecular dynamics, HRMC, Stillinger-Weber potential, ReaxFF, short-range order

STUDY OF AMORPHOUS BORON CARBIDE AND HYDROGENATED BORON CARBIDE MATERIALS USING MOLECULAR DYNAMICS AND HYBRID REVERSE MONTE CARLO

By

Rajan Khadka

A Master's Thesis
Submitted to the Graduate College
Of Missouri State University
In Partial Fulfillment of the Requirements
For the Degree of Master of Science, Materials Science

December 2019

Approved:

Ridwan Sakidja, Ph.D., Thesis Committee Chair

Kartik C. Ghosh, Ph.D., Committee Member

Tiglet Besara, Ph.D., Committee Member

Julie Masterson, Ph.D., Dean of the Graduate College

ACKNOWLEDGEMENTS

First of all, I would like to express my special thanks to my supervisor Prof. Dr. Ridwan Sakidja for his boundless and uninterrupted support during my two years of Master's Journey. He introduced me to this exciting world of atomic-scale simulation, and I am glad to be part of it. I will always be indebted to him for the research skills I have learned through his constant mentoring, guidance and availability.

A very special thanks to Prof. Dr. Kartik Ghosh for always being there as a fatherly figure during the entire process. I am also grateful to the head of department Prof. Dr. Robert Mayanovic for his critical remarks and suggestions regarding my research outcomes and Dr. Tiglet Besara for kindly serving in my thesis committee. I would like to extend my thanks to all the members of Sakidja Research Group (SRG). I am surely going to miss my time with you all.

I am very much thankful to NSF (DMREF-1729176) for the research grant support and Department of Energy (DOE) National Energy Research Scientific Computing Center's (NERSC) for providing their supercomputing facility under ERCAP0007777 computational project.

Finally, I am very much grateful to the Department of Physics, Astronomy and Materials Science, Missouri State University for believing in me and providing me with this opportunity for graduate studies here.

I dedicate this thesis to Mohan Bdr. Khadka (dad), Nil Kumari Khadka (mom), and Milan Khadka (brother).

TABLE OF CONTENTS

Introduction Page 1
- Boron Page 2
- Boron Carbide Page 5
- Closo-Carboranes ($C_2B_{10}H_{12}$) Page 7
- PECVD - Amorphous Hydrogenated Boron Carbide Page 10

Methodology Page 12
- Molecular Dynamics (MD) Simulation Page 12
- Stillinger-Weber (SW) Interatomic Potential Page 15
- Reactive Force Field (ReaxFF) Interatomic Potential Page 16
- Energy Minimization Page 19
- Hybrid Reverse Monte Carlo (HRMC) Technique Page 20

Computational Details Page 23
- SW-Potential Optimization Page 23
- Amorphous Boron Carbide - MD Page 25
- Amorphous Boron Carbide - HRMC Page 26
- Amorphous Hydrogenated Boron Carbide - MD Page 29

Results and Discussion Page 32
- SW Parameters Page 32
- Structure of Amorphous Boron Carbide - MD Page 40
- Structure of Amorphous Boron Carbide - HRMC Page 57
- Structure of Amorphous Hydrogenated Boron Carbide - MD Page 61

Conclusion Page 99

References Page 102

Appendix Page 118

LIST OF TABLES

Table 1. Crystal structure parameters of the pure elemental boron polymorphs. Where LP stands for the lattice parameter. Page 3

Table 2. Amorphous hydrogenated boron carbide models and their stoichiometry and density. Where LC = Linker CH_2, AP = Applied pressure, Calc = Calculated, Exp = Experimental. Page 30

Table 3. Average bond lengths of boron clusters calculated using Old SW, New SW and Ab initio generated structures. Where n = Boron clusters, OSW = Old SW, NSW = New SW. Page 33

Table 4. SW potential parameters for B_{12}-(CCC) used in LAMMPS. The values of three variables *p*, *q*, and *tol* after B are all zero except for the first four rows where p values are equal to 4.00. Page 35

Table 5. SW potential parameters for B_{12}-(CBC) used in LAMMPS. Angular cutoff: C-B-B = 117°, B-B-C= 122°, C-B-C absent so 109.47° used a cutoff, C-C-C and B-C-C are chain structures and 180° used although C-C-C was absent in this crystal structure. Page 35

Table 6. SW potential parameters for $B_{11}C_p$-(CBC) used in LAMMPS. Angular cutoff: C-B-C = Absent, B-C-C chain = 180°, All the three-body interaction C-B-B, B-B-C, C-B-C, C-C-B, and B-C-B distributed around the tetrahedral angle. So, the tetrahedral cutoff is used for all. Page 36

Table 7. Average bond length comparison of B_{12}, B_{12}-(CCC), B_{12}-(CBC), B_{12}-(CBC) and $B_{11}C_p$-(CBC) predicted using DFT, ReaxFF, New and Old SW potential. Page 37

Table 8. The density of the amorphous models using ReaxFF and New SW potential. Page 40

Table 9. Percentage of the angular type present in the amorphous models of boron carbide samples prepared using New SW and ReaxFF potential. Page 41

Table 10. The linear correlation coefficient of structural characteristics of a-B_xC:H_y models with their stoichiometry, simulation parameter, and density. All the correlation coefficient higher than 0.8 are highlighted in the table. Page 64

Table 11. The linear correlation coefficient of the bond angle distribution intensity peaks of a-B_xC:H_y models with their stoichiometry, simulation parameter, and density. All the correlation coefficient higher than 0.5 are highlighted in the table. Page 69

Table 12. The linear correlation coefficient of the *g(r)* of a-B_xC:H_y models with their stoichiometry, simulation parameter, and density. All the correlation coefficient higher than 0.8 are highlighted in the table. Page 82

Table 13. The linear correlation coefficient of *S(Q)* and coordination environments of a-B_xC:H_y models with their stoichiometry, simulation parameter, and density. Page 91

LIST OF FIGURES

Figure 1. Crystal structures of pure elemental boron polymorphs: (a) α-B_{12}, (b) β-B_{106}, (c) γ-B_{28}. Page 4

Figure 2. Icosahedral geometry. Page 4

Figure 3. Crystal structures of boron carbide: (a) B_{12}-(CCC), (b) B_{12}-(CBC), (c) $B_{11}C_p$-(CBC). Page 6

Figure 4. Molecular structure of icosahedral closo-carboranes: (a) 1, 2-$C_2B_{10}H_{12}$, (b) 1, 7- $C_2B_{10}H_{12}$, (c) 1, 12-$C_2B_{10}H_{12}$. (Green = B, Brown = C, White = H). Page 9

Figure 5. ortho-carborane structure: (a) IUPAC numbering of the ortho-carborane atoms, (b) Molecular geometry radius of atoms in ortho-carborane, (c) three body bonding environment of B and C atoms in ortho-carborane (Green = B, Brown = C, White = H). Page 9

Figure 6. (a) Periodic table showing the elements with ReaxFF parameter sets and (b) ReaxFF tree [109]. Page 18

Figure 7. A general working algorithm for HRMC simulation [6]. Page 21

Figure 8. Force norm variation with the no. of iterations. Both the axis are expressed in log scales. Page 24

Figure 9. A flow chart for modeling the amorphous boron carbide using MD and HRMC. Page 25

Figure 10. Flow chart showing the MD approach used for generating amorphous boron carbide using New SW and ReaxFF. Page 27

Figure 11. Pressure scheme applied for generating amorphous boron carbide models using New SW potential. Page 27

Figure 12. Densification scheme applied for generating amorphous hydrogenated boron carbide models. Page 31

Figure 13. The difference in average bond length of SW minimized α-boron structure with the variation of the SW potential σ parameter. Page 32

Figure 14. Stillinger-Weber potential two-body energy for B-B, B-C and C-C bonds comparison between Old SW and New SW parameters. Page 36

Figure 15. Old SW and New SW potential optimized structure of $B_{11}C_p$-(CBC). The icosahedral structure opened up during the minimization process for Old SW. Open icosahedral cages are circled red, Closed icosahedral cages are circled blue and C-C bond circled purple. Page 39

Figure 16. Bond angle distribution of DFT optimized structure compared to New SW minimized boron carbide crystal structure. Page 39

Figure 17. B-B-B and B-B-C type bond angle distribution comparison of a-B_{12}-(CCC) structure between New SW potential and ReaxFF. Page 42

Figure 18. B-B-B and B-B-C angular type comparison between New SW and ReaxFF generated a-B_{12}-(CBC) and a-$B_{11}C_p$-(CBC) amorphous models. Page 43

Figure 19. B-B-C angle in the ReaxFF made a-B_{12}-(CCC) model. Green atoms and bonds are the boron and brown atom and bonds are carbon. The red bond shows C atom bonding with B12 icosahedron's forming B-B-C angle. Page 45

Figure 20. The radial distribution function of a-B_{12}-(CCC) prepared using a) New SW b) ReaxFF and c) comparison between New SW and ReaxFF generated total RDF. Page 46

Figure 21. Nearest neighbor distances present in the B_{12} icosahedra. Here red, green and yellow colored boron atoms are used to show the first, second and third nearest neighbor distances respectively present in B_{12} icosahedra. Here, B_R-B_R = 1st neighbor, B_G-B_G = 2nd neighbor and B_Y-B_Y = 3rd neighbor. Page 47

Figure 22. Radial distribution function of a-B_{12}-(CBC) (left) and a-$B_{11}C_p$-(CBC) (right) prepared using a) New SW b) ReaxFF and c) comparison between New SW and ReaxFF generated total RDF. Page 48

Figure 23. Total structure factor of amorphous boron carbide a-B_{12}-(CCC) prepared using New SW (black line) and ReaxFF (red line) and their comparison with the (a) S(Q) of Random B_{12} (blue line) (b) DFT a-$B_{2.5}C$ [142] (blue line). Page 51

Figure 24. Total structure factor of amorphous boron carbide prepared using New SW (black line) and ReaxFF (red line) (a) a-B_{12}-(CCC) (b) a-B_{12}-(CBC) (c) a-$B_{11}C_p$-(CBC). Page 53

Figure 25. Some of the boron centered local structural environments present in the boron carbide crystal. Here green atoms are boron and

brown atoms are carbon. The dotted circle is used to show the first neighbor environment around the boron center marked as C. Page 54

Figure 26. Boron centered prominent local environment present in the amorphous boron carbide models prepared using New SW and ReaxFF potential. (a) a-B_{12}-(CCC) (b) a-B_{12}-(CBC) and (c) a-$B_{11}C_p$-(CBC). Page 56

Figure 27. Bond angle distribution comparison between the amorphous models generated by MD and HRMC both using New SW potential. (a) a-B_{12}-(CCC) (b) a-B_{12}-(CBC) (c) a-$B_{11}C_p$-(CBC). Page 57

Figure 28. Radial distribution function comparison between the amorphous models generated by MD and HRMC both using New SW potential. (a) a-B_{12}-(CCC) (b) a-B_{12}-(CBC) (c) a-$B_{11}C_p$-(CBC). Page 59

Figure 29. Static structure factor comparison between the amorphous models generated by MD and HRMC both using New SW potential. (a) a-B_{12}-(CCC) (b) a-B_{12}-(CBC) (c) a-$B_{11}C_p$-(CBC). Page 60

Figure 30. Boron centered prominent local environment present in the amorphous boron carbide models generated using MD and HRMC both using New SW potential (a) a-B_{12}-(CCC) (b) a-B_{12}-(CBC) and (c) a-$B_{11}C_p$-(CBC. Page 61

Figure 31. Coordination distributions of Boron atoms in the amorphous models in MD and HRMC. (a) a-B_{12}-(CCC) (b) a-B_{12}-(CBC) (c) a-$B_{11}C_p$-(CBC). Page 62

Figure 32. (a) Hydrogen concentration variation on the models of a-B_xC:H_y. (b) Variation of calculated and experimental density. Page 62

Figure 33. No. of boron, carbon, hydrogen bonds present in the a-B_xC:H_y models. Page 63

Figure 34. Percentage of the partial bond angle distribution present in the different models of a-B_xC:H_y ranging from Model-D11 to Model-B3. Page 67

Figure 35. Total bond angle distribution of all the amorphous hydrogenated boron carbide models. Page 70

Figure 36. B-B-B bond angle distribution present in the amorphous hydrogenated boron carbide models. Page 70

Figure 37. B-B-C bond angle distribution present in the amorphous hydrogenated boron carbide models. Page 71

Figure 38. B-B-H bond angle distribution present in the amorphous hydrogenated boron carbide models. Page 72

Figure 39. B-C-C bond angle distribution present in the amorphous hydrogenated boron carbide models. Page 74

Figure 40. B-C-H bond angle distribution present in the amorphous hydrogenated boron carbide models. Page 74

Figure 41. C-B-B bond angle distribution present in the amorphous hydrogenated boron carbide models. Page 77

Figure 42. C-B-C bond angle distribution present in the amorphous hydrogenated boron carbide models. Page 78

Figure 43. C-B-H bond angle distribution present in the amorphous hydrogenated boron carbide models. Page 78

Figure 44. C-C-H bond angle distribution present in the amorphous hydrogenated boron carbide models. Page 79

Figure 45. The radial distribution function of all the amorphous a-B_xC:H_y models. Page 80

Figure 46. Boron to boron partial radial distribution function for all the a-B_xC:H_y models. Page 83

Figure 47. Boron to carbon partial radial distribution function for all the a-B_xC:H_y models. Page 83

Figure 48. C_2B_{10} icosahedral structure in the a-B_xC:H_y models (a) At 0 ps, (b) After 1 ps. (Green = boron, Brown = carbon, H-atoms are removed for the better visualization) Page 85

Figure 49. Orthocarborane with the second nearest neighbor distance for B-H and C-H. (Green = boron, Brown = carbon, White = hydrogen atoms.) Page 85

Figure 50. Boron to hydrogen partial radial distribution function for all the a-B_xC:H_y models. Page 86

Figure 51. Carbon to carbon partial radial distribution function for all the a-B_xC:H_y models. Page 87

Figure 52. Carbon to hydrogen partial radial distribution function for all the a-$B_xC:H_y$ models. Page 87

Figure 53. Hydrogen to hydrogen partial radial distribution function for all the a-$B_xC:H_y$ models. Page 88

Figure 54. Orthocarborane with the nearest neighbor distance for H-atom. (Green = boron, Brown = carbon, White = hydrogen atoms.) Page 89

Figure 55. Structure factor *S(Q)* comparison for all the a-$B_xC:H_y$ models. Page 90

Figure 56. Boron centered structural units present in the a-$B_xC:H_y$ models. Page 92

Figure 57. Boron centered structural units present in the a-$B_xC:H_y$ models. Page 93

Figure 58. Boron centered structural units present in the a-$B_xC:H_y$ models. Page 93

Figure 59. Boron centered structural units present in the a-$B_xC:H_y$ models. Page 94

Figure 60. Carbon centered structural units present in the a-$B_xC:H_y$ models. Page 95

Figure 61. Carbon centered structural units present in the a-$B_xC:H_y$ models. Page 96

Figure 62. Hydrogen centered structural units present in the a-$B_xC:H_y$ models. Page 97

Figure 63. Boron and carbon-centered average structural units present in the a-$B_xC:H_y$ models. Page 97

Figure 64. Coordination distribution of boron, carbon, hydrogen present in the a-$B_xC:H_y$ models. Page 98

INTRODUCTION

Boron has the unique ability to form caged structures of different sizes [1]. These inherent nature of boron cage structure are present in the boron carbide crystal structures, in their amorphous forms as well as the *closo*-carboranes. A large variety of boron carbide structure exists depending upon the B/C stoichiometric ratio (from B_4C to $B_{10}C$) in the structure dictated by carbon concentration [2]. Boron carbide material is considered as one of the extremely hardest (hardness 30 GPa) materials [3]. It has a high melting point of approximately ~ 2450^oC [4] and a low density of 2.52 g/cm^3[5]. It is a material of choice for harsh environments because of its extreme hardness, wear-resistant, thermal stability, high melting point and chemical inertness [6]. It is used as lightweight body armor, as a neutron absorber in the nuclear reactors [7] and as a shielding material [6].

Another class of material, particularly of our interest, containing caged boron structure is the amorphous hydrogenated boron carbide (a-B_xC: H_y) materials prepared from *closo*-carboranes. The a-B_xC:H_y thin film materials are widely used as a wear-resistant coating for mechanical systems [8] and hard disks [9]. They are thermally stable up to ~ 1200 K temperature making it a suitable material of choice for thermal shock resistance.[10] The a-B_xC:H_y films are chemically inert and resists erosion [11,12] and have also displayed surprisingly high hydrogen sorption properties [13]. The a-B_xC:H_y material is found to be superior to a-SiOC:H films with a higher value of Young's modulus and good thermal conductivity [12,14]. Other than the excellent thermal, chemical and mechanical properties boron-rich materials in recent years have started to emerge as a viable alternative to silicon technology [15]. Plasma-enhanced chemical vapor deposition (PECVD) deposited a-B_5C:H is p-type semiconductors [16] which when doped

with Ni showed eightfold increase in the electrical conductivity at room temperature displaying n-type semiconducting behavior making it possible to create boron-based homojunction diode [15]. Very recently, a-$B_xC:H_y$ films is shown to be useful for interlayer dielectric application due to its ultra-low dielectric constant (<2.5) [12,14,17]. The high electrical conductivity, low leakage current and high breakdown voltage characteristics of a-$B_xC:H_y$ films has made boron-rich materials useful for electronic applications [10,14,18]. Boron carbide materials has already been fabricated as heterojunction diode [19–21], heteroisomeric diode of p-type *ortho*-carborane (*o*-$C_2B_{10}H_{12}$) and n-type *meta*-carborane (*m*-$C_2B_{10}H_{12}$) [22], solid-state neutron detection devices [17,23], junction field-effect transistor (JFET) [19] and, many more electronics devices.

To completely understand the amorphous characteristics of a-B_xC and a-$B_xC:H_y$ class of materials it is important to discern their crystal structures the remanence of which is found in their amorphous forms. The following sub-section describes the crystal structures of boron, boron carbide, and *closo*-carboranes.

Boron

The crystal structure of the pure elemental boron has three different kinds of polymorphs based on the B_{12} icosahedral subunit [24]. They are namely α-rhombohedral boron (α-B_{12})[25], β-rhombohedral boron (β-B_{105}) [26], and the high-pressure phase γ-boron (γ-B_{28}) [27] as shown in Figure 1. All the structures of Figure 1 can clearly show that all these structures have icosahedral based motif B_{12} as a building block. Table 1 shows the crystal structure properties of these polymorphs. The primitive unit cell of α-B_{12} consists of a 12-atom system in a rhombohedral lattice which is the smallest among all the elemental boron polymorphs. Similarly, β-B_{105} boron has 105 atoms in the rhombohedral unit cell which can be separated into B_{84} and

B_{10}-B-B_{10} [28]. The γ-B_{28} containing 28 atoms in an orthorhombic cell is thermodynamically favorable in between a higher pressure region of 19-89 Gpa at absolute temperature. The γ-B_{28}

Table 1. Crystal structure parameters of the pure elemental boron polymorphs. Where LP stands for the lattice parameter.

Name	Structure	No. of sites	Space group	Density (g/cm^3)	LP (Å)	Inter-axial Angles (°)
α-B_{12}	Rhombohedral	12	$R\bar{3}m$	2.48	5.050	58.039
β-B_{105}	Rhombohedral	105	$R\bar{3}m$	2.31	10.123	65.244
γ-B_{28}	Orthorhombic	28	*Pnnm*	2.57	5.0430	90.000

has sodium chloride type structure with icosahedral B_{12} in place of Cl^- and B_2 in place of Na^+. [27] The γ-B_{28} is the densest phase among all and has different space-group Pnnm compared to other two polymorphs which have $R\bar{3}m$ [29]. All these polymorphs exhibits the Vickers hardness above 40 Gpa and boron is the only element to possess this unique super hardness property on all its polymorphs [30]. The order of hardness among these polymorphs is found to be α-B_{12}<β-B_{105}<γ-B_{28} making γ-B_{28} to be the super hard polymorphs among them [30]. Ab-initio studies had shown that among all the polymorphs β-B_{105} is the thermodynamically stable structure at ambient conditions [30] whereas α-B_{12} structure is the stable ground state structure for elemental boron [24].

The icosahedral framework in α-B_{12} structure is similar to the boron framework found in the crystalline boron carbide structure with the difference of the chain atoms. The intra-icosahedral B-B bonding in α-B_{12} is 1.77 Å [31,32] which is close to that found in the B_4C crystal structure [25,33]. Also, both the structures have threefold rhombohedral symmetry. The similarity of α-B_{12} and B_4C crystal is such that α-B_{12} can be transformed into B_4C with the

widening of inter-axial angle from ~ 58° to ~ 65° and replacing three center Δ-bonds to include the chain atoms [33]. Figure 2 shows the regular icosahedral geometry which contains 12 vertices (represented by green balls) and 20 equilateral triangles. It is a convex polyhedron having fivefold rotations about its vertices, 60 proper rotations, and 120 symmetry operations represented with I_h symmetry [33].

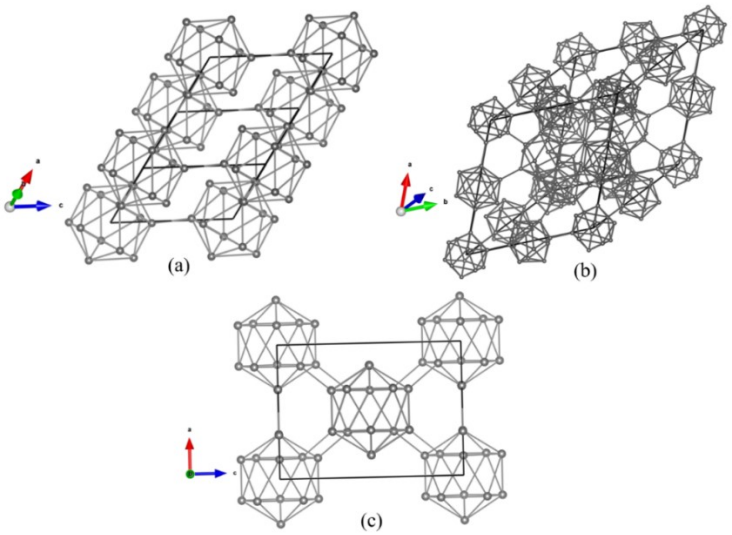

Figure 1. Crystal structures of pure elemental boron polymorphs: (a) α-B_{12}, (b) β-B_{106}, (c) γ-B_{28}.

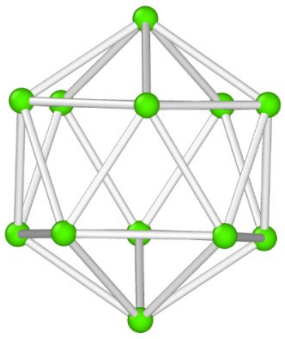

Figure 2. Icosahedral geometry.

Boron Carbide

The crystal structure of boron carbide has a primitive unit cell which consists of a 15-atom system with a 12-atom icosahedral cage having a rhombohedral lattice of trigonal symmetry ($R\bar{3}m$ space group) and linear chain of 3-atoms connecting icosahedra along the (111) rhombohedral axis as shown in Figure 3 [34]. Different variants of boron carbide have been studied and proposed based on symmetry considerations: i) Carbon-rich B_4C ($B_{12}C_3$) as shown in Figure 3 (a) [35], having the structural configuration of B_{12}-(CCC), is the electron-precise form of boron carbide [2] and band calculation suggests this variant be a semiconductor [36]. ii) Boron-rich $B_{6.5}C$ ($B_{13}C_2$) [35] has the structural configuration of B_{12}-(CBC) as shown in Figure 3(b) with, calculations suggesting a metallic nature [37] which is contrary to experimentally formed boron carbide which is a semiconductor for a wide range of carbon concentration [2]. iii) B_4C having a structural configuration as $B_{11}C_p$-(CBC) as shown in Figure 3 (c) is finally suggested as the most energetically stable variant by theoretical energy minimization [38,39], where p-stands for the polar site in the icosahedral structure which forms intra-icosahedral bonding with neighboring icosahedra's. It has been theoretically and experimentally agreed upon that $B_{11}C_p$-(CBC) is the atomic configuration for the stoichiometry of the B_4C and $R\bar{3}m$ space group [34].

Small scale *ab-initio* generated structures of amorphous boron carbide suggests the presence of B_{12}, $B_{11}C$, and $B_{10}C_2$ icosahedra embedded in the amorphous matrix of boron and carbon [5,40]. Experimentally prepared amorphous boron carbide via chemical vapor deposition (CVD) [5] confirmed the presence of distorted icosahedrons in their sample. Short-range order (SRO) study of a-B_4C thin film deposited by radio frequency (RF) magnetron sputtering assessed

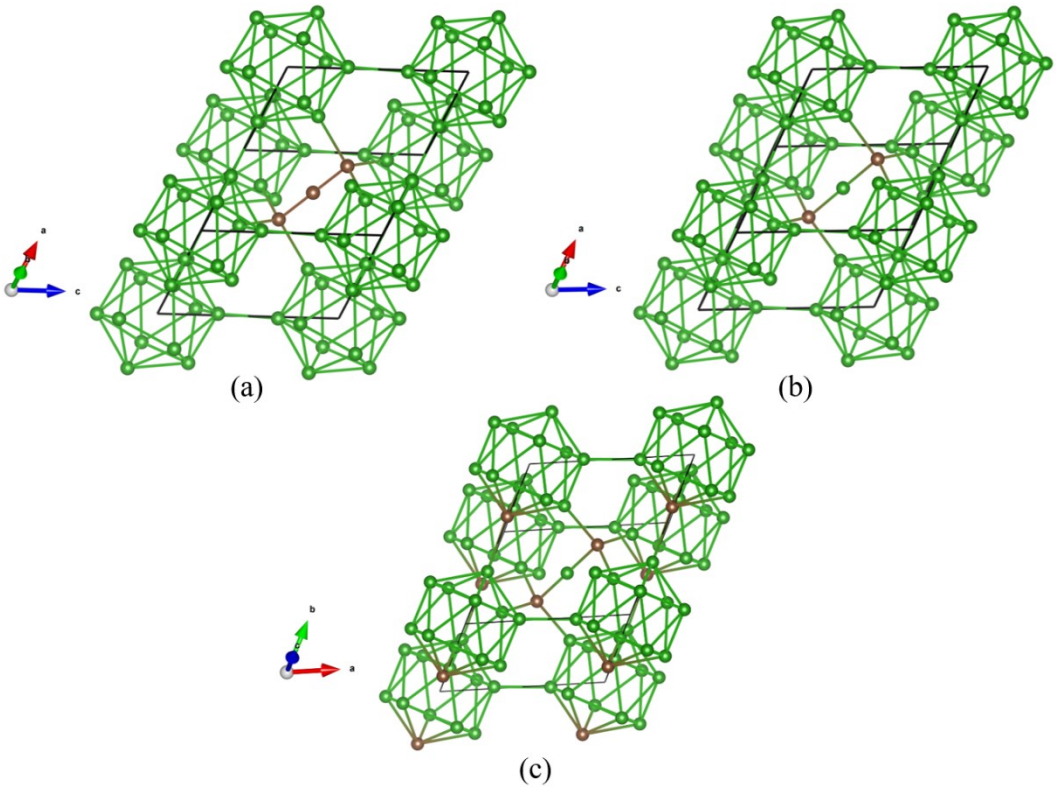

Figure 3. Crystal structures of boron carbide: (a) B_{12}-(CCC), (b) B_{12}-(CBC), (c) $B_{11}C_p$-(CBC).

using Fourier transform infrared (FTIR) spectra and pair distribution function (PDF) analysis also verified icosahedral presence [41]. Other experimental a-B_xC thin films studied using x-ray absorption near-edge spectroscopy (XANES) [42] and IR & Raman spectroscopy [43] found a random network of icosahedral structure residing inside thin films. Similarly, strain-induced amorphous boron carbide studied using Raman spectroscopy [44,45] indicated the collapse of the unit cell into icosahedrons and fragments of C and B atoms.

Ab-initio MD studies of the SRO of a-B_xC have been done for small scale systems of 120, 135 atoms [40] and 216 atoms [5] but fewer efforts have been made to characterize larger systems due to the limitation of size and computational cost associated with first-principle calculations. Short-range ordering of amorphous boron carbide materials for larger models is

needed to fully understand the presence of a network of icosahedrons embedded inside the boron and carbon matrix.

In the present work, the short-range ordering of a-B_xC is studied using Molecular Dynamics. Larger amorphous models of boron carbides of size 10935 atoms as compared to previous ab-initio studies [5,40] are prepared and studied. The amorphous models associated with B_{12}-(CCC), B_{12}-(CBC) and $B_{11}C_p$-(CBC) are prepared using the Stillinger-Weber (SW) and ReaxFF potentials. The existing SW potential of the B-C system [46] was further modified for icosahedral B-C systems to create these models. Potential energy minimization of α-rhombohedral boron and crystalline B_xC is used to modify the length scaling parameter (σ) and angular cutoffs. Amorphous models generated using the newly parameterized SW and ReaxFF potentials are compared among and with other experimental and first-principle studies. In addition, Hybrid Reverse Monte Carlo (HRMC) equipped with the new SW potential parameters is used to further study the structure of amorphous boron carbide. Realspace, reciprocal space and angular information of the new SW generated MD models of amorphous boron carbide is used as structural constraints to guide the HRMC simulation.

Closo-Carboranes ($C_2B_{10}H_{12}$)

Closo-carboranes with the stoichiometry of $C_2B_{10}H_{12}$ have only three different types of isomers namely *ortho*-, *meta*-, and *para*- [47,48]. Earlier x-ray diffraction studies have shown that these carborane isomers are made up of slightly distorted inner C_2B_{10} icosahedra [49]. Figure 4 shows the molecular structure of these isomers which consists of two C-atom and ten B-atom icosahedra with twelve radially outward-pointing H-atom [50]. They are packed as a molecular crystal with four molecules in a face-centered cubic (FCC) structure at room

temperature [47,49]. These isomers vary from each other based on the C-atom position within the *inner*-icosahedral cage structure. Figure 4 (a) is an *ortho*-carborane molecule that has a carbon position as C_1 and C_2 hence the name 1, 2-$C_2B_{10}H_{12}$. Similarly, Figure 4 (b) is a *meta*-carborane that has carbon positions C_1 and C_7 thus called 1, 7- $C_2B_{10}H_{12}$ whereas *para*-carborane in Figure 4 (c) has carbon positions at the two opposite end of inner icosahedra. These *closo*-carboranes has a unit cell length of 9.86 Å and the nearest neighbor intermolecular distance of 6.97 Å [49]. The *ortho*- and *meta*-carborane has same point group C_{2v} whereas *para*-carborane has D_{5d} point group symmetry. *Ab-initio*, as well as experimental studies, have shown *para*-carborane to be the most stable isomer where *ortho*-carborane is found to be the least stable one [48,51]. The *ortho*-carborane isomer rearranges to form *meta*-carborane at 873 K and *meta*-carborane isomerizes to *peta*-carborane at 973 K [52].

The *ortho*-carborane molecule is widely used as a gaseous precursor for the fabrication of a-B_xC:H_y thin films using the PECVD process as detailed in the later section. Figure 5 (a) shows the *ortho*-carborane icosahedral cage structure with an international union of pure and applied chemistry (IUPAC) numbering. In the *ortho*-carborane molecule, the molecular geometry radius of boron atom (r_B) is 1.665 Å which is greater than that of carbon (r_C=1.5275 Å) indicating the distorted icosahedral geometry. The molecular geometry radius of radially outward-pointing H-atom varies from r_C+C-H to r_B+B-H [47,49] as shown in Figure 5 (b). The density functional theory (DFT) geometry optimization and diffraction experiment characterized *ortho*-carborane molecule have C-C pair bond length lie in the range 1.610 - 1.653 Å, C-B pairs in the range 1.69-1.72 Å, B-B pairs in the range 1.77-1.83 Å, B-H pairs in the range 1.192-1.196 Å and, C-H pairs as 1.093 Å [50,51,53]. Bond length of *ortho*-carborane molecule follows the order C-H < B-H < C-C < C-B < B-B with C-H being the smallest and B-B being the longest bond present in the

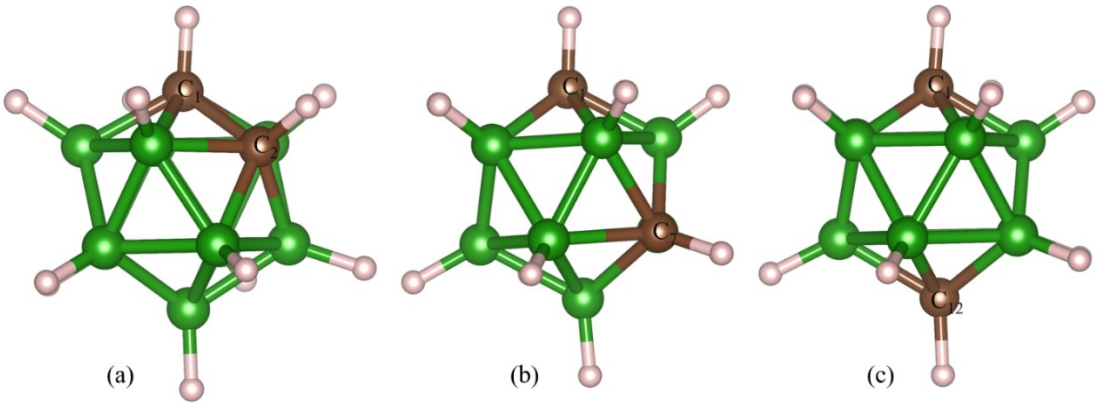

Figure 4. Molecular structure of icosahedral *closo*-carboranes: (a) 1, 2-$C_2B_{10}H_{12}$, (b) 1, 7-$C_2B_{10}H_{12}$, (c) 1, 12-$C_2B_{10}H_{12}$. (Green = B, Brown = C, White = H).

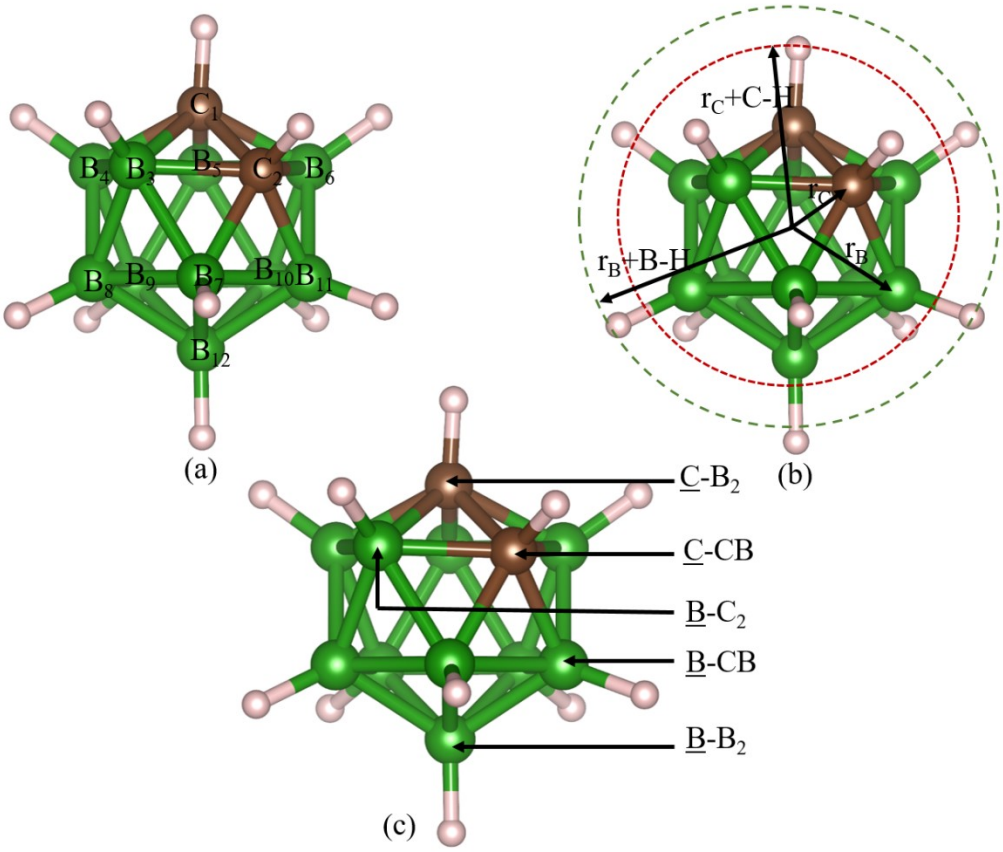

Figure 5. *ortho*-carborane structure: (a) IUPAC numbering of the *ortho*-carborane atoms, (b) Molecular geometry radius of atoms in *ortho*-carborane, (c) three body bonding environment of B and C atoms in *ortho*-carborane (Green = B, Brown = C, White = H).

structure. The three-body type bonding environment of boron and carbon in the *ortho*-carborane molecule is shown in Figure 5 (c). There are three different types of three-body boron bonding environments namely B-B_2, B-CB and B-C_2 with the binding energies in the order of B-B_2 < B-CB < B-C_2 and two types of carbon bonding environment namely C-B_2 and C-CB [54]. For a typical PECVD deposition process high pressure and low temperature of ~ 373 K is desirable [55]. *Ortho*-carborane has a low melting point of ~ 567-569 K [56] and a high value of saturated vapor pressure of ~ 4000 Pa at the temperature as low as 423 K [57] making it a suitable precursor for PECVD deposition process.

PECVD – Amorphous Hydrogenated Boron Carbide

Experimentally amorphous hydrogenated boron carbide (a-B_xC:H_y) films has been extensively studied using PECVD process using variety of precursors such as 1) toxic diborane (B_2H_6) or *nido*-pentaborane (B_5H_9) or *nido*-decaborane ($B_{10}H_{14}$) in combination with methane (CH_4) and, hydrogen (H_2) as a working gas [8,10,20,58–62] 2) decomposition of harmless single-source precursor *ortho*-carborane (*o*-$C_2B_{10}H_{12}$) [12,15–19,21,57,63–71] or in presence of pyridine (C_5H_5N) [72] or methane (CH_4) [14] 3) Single-source precursor trimethyl boron ($B(CH_3)_3$) [73] or triethyl boron ($B(C_2H_5)_3$) 4) mixture of *meta*-carborane (*m*-$C_2B_{10}H_{12}$) with aniline ($C_6H_5NH_2$) [74]. Here, we will focus primarily on a-B_xC:H_y thin films widely prepared using the *o*-$C_2B_{10}H_{12}$ PECVD process which allows fabrication of high-temperature boron carbide materials at low temperature. The a-B_xC:H_y thin films developed using *o*-$C_2B_{10}H_{12}$ is an ecologically safe precursor and yields unique transport properties due to its 3-dimensional icosahedral based geometry [15]. Since the late 90's *o*-$C_2B_{10}H_{12}$ precursor PECVD process has

been used for *in-situ* boronization of tokamak chambers [57] over previously used toxic diboranes [10] as the a-$B_xC:H_y$ films are chemically resistant and heat-proof [70].

During the PECVD growth process of a-$B_xC:H_y$ films the experimental processing and growth parameter such as temperature, power, total flow rate, partial flow rate, and, growth time dictates the films atomic H % and B/C stoichiometry in the film which in turn gives rise to different mechanical, dielectric, electronic and charge transport properties [12,14,17,18]. In spite of successful device fabrication, an atomistic structural bonding environment giving rise to film properties is yet not completely well understood [9,15,18,61,75,76]. Experimentally, it is difficult to get the detailed atomic arrangement measurements even with the use of transmission electron microscopy (TEM) and x-ray diffraction (XRD) [65]. Tentative assignment of certain stretching modes during the peak overlapping in the spectrum [14,18], hypothetical and inconsistent fitting of the experimentally obtained spectrum is problematic to understand the chemical bonding environment of the structures. Knowledge of the structural ordering of PECVD fragments and decomposed icosahedral boron carbide cage in the thin film is of central importance to comprehend the resulting electrical, mechanical and chemical properties of boron rich materials. In this study, we have attempted to understand the structural properties such as radial distribution function (RDF), structure factor (*S(Q)*), bond angle distribution (*B(θ)*), bond counts, coordination number, structural environment of PECVD prepared a-$B_xC:H_y$ films using single-source precursor *o*-$C_2B_{10}H_{12}$ and their correlation with the structures atomic H %, B/C stoichiometry and density.

METHODOLOGY

Molecular Dynamics (MD) Simulation

MD simulations are used to study the properties and the phenomenon of materials that are beyond the *ab-initio* calculations. *Ab-initio* calculations though accurate are limited to only the very small number of atoms typically in hundreds. MD considers only the atomic interactions and neglects the effects of nuclei and electrons. This is the reason why we cannot obtain the electromagnetic properties of the material using this technique. The interactions between the atoms are guided by the empirical potential function which is fitted against the *ab-initio* calculations. Once we know the potential parameters for the interacting system and providing initial atomic coordinates and the velocities we can obtain the time evolution of the atomic system. The trajectories of evolving systems are obtained by integrating Newton's equations of motion. The mathematical formulation for Newton's second law can be written as

$$\boldsymbol{F}_i(t) = m_i \boldsymbol{a}_i(t) = m_i \frac{d\boldsymbol{v}_i(t)}{dt} = m_i \frac{d^2\boldsymbol{r}_i(t)}{dt^2}$$

Where m_i is the mass, $\boldsymbol{r}_i$ is the position vector, and $\boldsymbol{F}_i(t)$ is the force acting on i^{th} atom at instantaneous time t. The force acting on an isolated system can also be expressed as the negative gradient of the potential with respect to the particle's position as

$$\boldsymbol{F}_i(t) = -\nabla U(r_i)$$

Where $U(r_i)$ is the potential as a function of particle position. So, having $U(r_i)$ we can calculate the forces on the atoms. With the force information, we can integrate the above equations to calculate particle velocity $\boldsymbol{v}_i(t)$ from the single integration and particle position $\boldsymbol{r}_i(t)$ from the double integration.

In 1957 Alder and Wainwright for the first time used the hard-sphere model to calculate the equation of state with the square well potentials [77]. Later, in 1964 Rahman used continuous potential (Lennard-Jones [78]) to calculate the self-diffusion in liquid argon system consisting of 864 particles [79]. MD simulation using continuous potential is a many-body problem that cannot be solved analytically and a finite difference method is essential [80]. The finite difference method breaks the problem into small steps with the timestep of δt. Assuming we know the potential function the total force on an atom at any time t is calculated solving the above equations for the interactions with other atoms. Then, acceleration $\boldsymbol{a}_i(t) = \boldsymbol{F}_i(t)/m_i$, velocity $\boldsymbol{v}_i(t)$, and position $\boldsymbol{r}_i(t)$ can be calculated. Now, the force on new atomic co-ordinates is calculated to generate particles acceleration, velocity, and position for the time $t+\delta t$ is calculated using finite difference method. All the finite difference methods use Taylor series expansion to approximate the $\boldsymbol{a}(t+\delta t)$, $\boldsymbol{v}(t+\delta t)$, and $\boldsymbol{r}(t+\delta t)$ as

$$\boldsymbol{r}(t+\delta t) = \boldsymbol{r}(t) + \frac{d\boldsymbol{r}(t)}{dt}\delta t + \frac{1}{2!}\frac{d^2\boldsymbol{r}(t)}{dt^2}\delta t^2 + \frac{1}{3!}\frac{d^3\boldsymbol{r}(t)}{dt^3}\delta t^3 + \cdots$$

$$\boldsymbol{v}(t+\delta t) = \boldsymbol{v}(t) + \frac{d\boldsymbol{v}(t)}{dt}\delta t + \frac{1}{2!}\frac{d^2\boldsymbol{v}(t)}{dt^2}\delta t^2 + \frac{1}{3!}\frac{d^3\boldsymbol{v}(t)}{dt^3}\delta t^3 + \cdots$$

$$\boldsymbol{a}(t+\delta t) = \boldsymbol{a}(t) + \frac{d\boldsymbol{a}(t)}{dt}\delta t + \frac{1}{2!}\frac{d^2\boldsymbol{a}(t)}{dt^2}\delta t^2 + \frac{1}{3!}\frac{d^3\boldsymbol{a}(t)}{dt^3}\delta t^3 + \cdots$$

Different algorithms such as the Verlet algorithm [81], leap-frog algorithm [82], velocity-Verlet [83], Beeman's algorithm [84] and predictor-corrector method [79] are used in MD simulations to perform integration of the equation of motion. Among all velocity-Verlet doesn't compromise the accuracy and is one of the most commonly used algorithms to approximate $\boldsymbol{a}(t+\delta t)$, $\boldsymbol{v}(t+\delta t)$, and $\boldsymbol{r}(t+\delta t)$. Here, velocity is approximated every half time step $\boldsymbol{v}(t+\delta t/2)$ and position is calculated at every full step $\boldsymbol{r}(t+\delta t)$ using $\boldsymbol{v}(t+\delta t/2)$ [83].

$$\boldsymbol{v}\left(t+\frac{\delta t}{2}\right)=\boldsymbol{v}(t)+\frac{d\boldsymbol{v}(t)}{dt}\left(\frac{\delta t}{2}\right)$$

$$\boldsymbol{r}(t+\delta t)=\boldsymbol{r}(t)+\boldsymbol{v}\left(t+\frac{\delta t}{2}\right)\delta t$$

The force between the atoms are determined with the updated position and then acceleration $\boldsymbol{a}(t+\delta t)$ is given by

$$\boldsymbol{a}(t+\delta t)=\frac{F(t+\delta t)}{m}=-\frac{\nabla \mathrm{U}(t+\delta t)}{m}$$

Finally, the velocity at full-time step $\boldsymbol{v}(t+\delta t)$ is computed making use of $\boldsymbol{a}(t+\delta t)$ as

$$\boldsymbol{v}(t+\delta t)=\boldsymbol{v}\left(t+\frac{\delta t}{2}\right)+\frac{1}{2}\boldsymbol{a}(t+\delta t)$$

MD simulation performed in this way can be used to calculate the structural and mechanical properties, thermal expansion coefficients, melting points, phase diagrams, diffusion coefficients, grain boundary structure, dislocation dynamics, shock wave propagation and many more properties. This process is extremely faster than *ab-initio* calculation and can perform the large scale simulations of thousands of atoms. MD simulation is highly dependent upon the availability of the interatomic potentials. And the availability of the multi-element system interatomic potential is very limited, also the analysis of the resulting outcome from the MD simulation relies upon the accuracy and fitting of the empirical potential function. One should always be careful while choosing the specific potential and must ensure the transferability of the potential. A more detailed description regarding the MD simulation can be found in these References [80,85–87]. For our research purpose, we have performed our MD calculations using the Large-Scale Atomic/Molecular Massively Parallel Simulator (LAMMPS) [88]. There are other MD simulation codes in existence like Groningen Machine for Chemical Simulations (GROMACS) [89], General Utility Lattice Program (GULP) [90], ITAP Molecular Dynamics

(IMD) [91], Molecular Dynamics code for Avogadro Challenge Project (MDACP) [92], Nanoscale Molecular Dynamics (NAMD) [93] and more which can be used depending upon one's need.

Stillinger-Weber (SW) Interatomic Potential

Stillinger and Weber pioneered the empirical form of the interaction potential to describe the condensed phases of silicon which produced the structural and vibrational properties of amorphous silicon [94]. Since then SW potential has been successfully used in modeling single element and multi-element covalent solids like C [95,96], B [97], B-C [46], B-N [98], Si-N-H [99], In-Ga-N [100], Zn-Cd-Hg-S-Se-Te [101] and many more.

The Stillinger–Weber total energy model is given by the sum of the two-body and three-body interaction terms [94] as

$$E = \sum_i \sum_{j>i} V_2(r_{ij}) + \sum_i \sum_{j\neq i} \sum_{k>j} V_3(r_{ij}, r_{ik}, \theta_{ijk})$$

The two-body interaction functional form is written as

$$V_2(r_{ij}) = \varepsilon_{ij} A_{ij} \left[B_{ij} \left(\frac{\sigma_{ij}}{r_{ij}}\right)^{p_{ij}} - \left(\frac{\sigma_{ij}}{r_{ij}}\right)^{q_{ij}} \right] exp\left(\frac{\sigma_{ij}}{r_{ij} - \sigma_{ij} a_{ij}}\right)$$

Where $a\sigma$ is the cutoff distance for which V_2 vanishes. The three-body interaction potential form as used in LAMMPS [102] is

$$V_3(r_{ij}, r_{ik}, \theta_{ijk}) = \varepsilon_{ijk} \lambda_{ijk} exp\left(\frac{\gamma_{ij}\sigma_{ij}}{r_{ij} - \sigma_{ij} a_{ij}} + \frac{\gamma_{ik}\sigma_{ik}}{r_{ik} - \sigma_{ik} a_{ik}}\right) \left[cos\theta_{ijk} - cos\theta_{0ijk}\right]^2$$

Here, the subscripts *ij* represents pair interaction and *ijk* represents the three-body term. r_{ij} and r_{ik} are the interatomic distances and θ_{ijk} is the angle between bonds *ij* and *ik* with *i* being the central atom. Angle θ_{0ijk} is the angular cutoff for which three-body interaction term vanishes. For

the ideal tetrahedral system, θ_{0ijk} is 109.47°. Parameters ε and σ are energy and length scaling parameters to tune cohesive energy and lattice constant of elements under study [103]. Two body and three-body interactions are tuned using *A, B, p, q,* λ, and γ. Two body interaction is invariant upon exchange of indices *i* and *j* and three-body interaction term is invariant upon the exchange of second and third indices of *ijk* [99].

Reactive Force Field (ReaxFF) Interatomic Potential

ReaxFF potential is a bond-order based empirical force field (EFF) for the reactive chemical system which offers the accuracy close to the *ab-initio* calculation for the molecular dynamics simulation with the very less computational expense [104–109]. Quantum mechanical (QM) level calculation is limited to the small atomic system but ReaxFF potential well fitted with QM generated force and energy information can accurately describe the reactive events in solid, liquid and gas phase interfaces [109]. In 2001, Duin et al. first formulated the functional form of the ReaxFF potential [104]. Since then it has been modified over the years but the current version adopted in LAMMPS is the 2008 functional form by Chenoweth et al. [106]. For our research purpose we have adopted the ReaxFF force field parameters trained exclusively for boron carbide (B_4C) and *ortho*-carborane ($C_2B_{10}H_{12}$) by An et al. [110]. ReaxFF includes all the non-bonded interactions, covalent interactions, van der Waals and Columbic interactions as a summation in the total energy of system [104,106]. The total energy of any system $\left(E_{sys}\right)$ in ReaxFF formalism [107] is written as

$$E_{sys} = E_{bond} + E_{over} + E_{under} + E_{lp} + E_{val} + E_{tors} + E_{vdWaals} + E_{Coulomb}$$

Here, E_{bond} = Bond forming energy

E_{over} = Over-coordination energy

E_{under} = Under-coordination energy

E_{lp} = Lone-pair energy

E_{val}= Valence angle energy

E_{tors}= Torsion angle energy

$E_{vdWaals}$= van der Waals interaction energy

$E_{Coulomb}$= Coulomb interaction energy

ReaxFF calculates the bond order between the pairs *ij* from their interatomic distance (r_{ij}). ReaxFF differentiates between the σ, π, and $\pi\pi$ bonding environment. So, the bond-order BO'_{ij} between atomic pair is written as [106]

$$BO'_{ij} = BO^{\sigma}_{ij} + BO^{\pi}_{ij} + BO^{\pi\pi}_{ij}$$

A detailed description regarding the ReaxFF formalism can be found in these references [104,106,107].

Above mentioned ReaxFF functional form is trained against the QM-based training set which normally includes bond dissociation energies, transition states, the heat of formation, equation of states (EOS), reaction energies and geometry of the molecules (bond angle, bond lengths) [108]. Thus derived parameter set is shown to have accurately described the bond breaking and bond formation process during the MD simulation [106]. Most of the ReaxFF parameter sets in existence are fitted using a single-parameter optimization method [111] to minimize the cost function error

$$\chi^2 = \sum_{i=1}^{n} \left(\frac{x_{i,training\ set} - x_{i,calc}}{\sigma} \right)^2$$

Where $x_{i,training\ set}$ are the QM derived values, $x_{i,calc}$ are the ReaxFF calculated values and σ is the acceptance criterion which controls the total error function χ^2 during the fitting

process. Thus generated ReaxFF parameters are highly transferable across all the phases e.g. oxygen parameters for solid oxide phase, gas phase (O_2), and liquid phase (H_2O) remain the same [109]. Figure 6 (a) shows all the elements whose parameter sets have been developed as of 2016. It is important to note however that the ReaxFF parameters are non-transferable across the different branches of the ReaxFF tree as shown in Figure 6 (b).

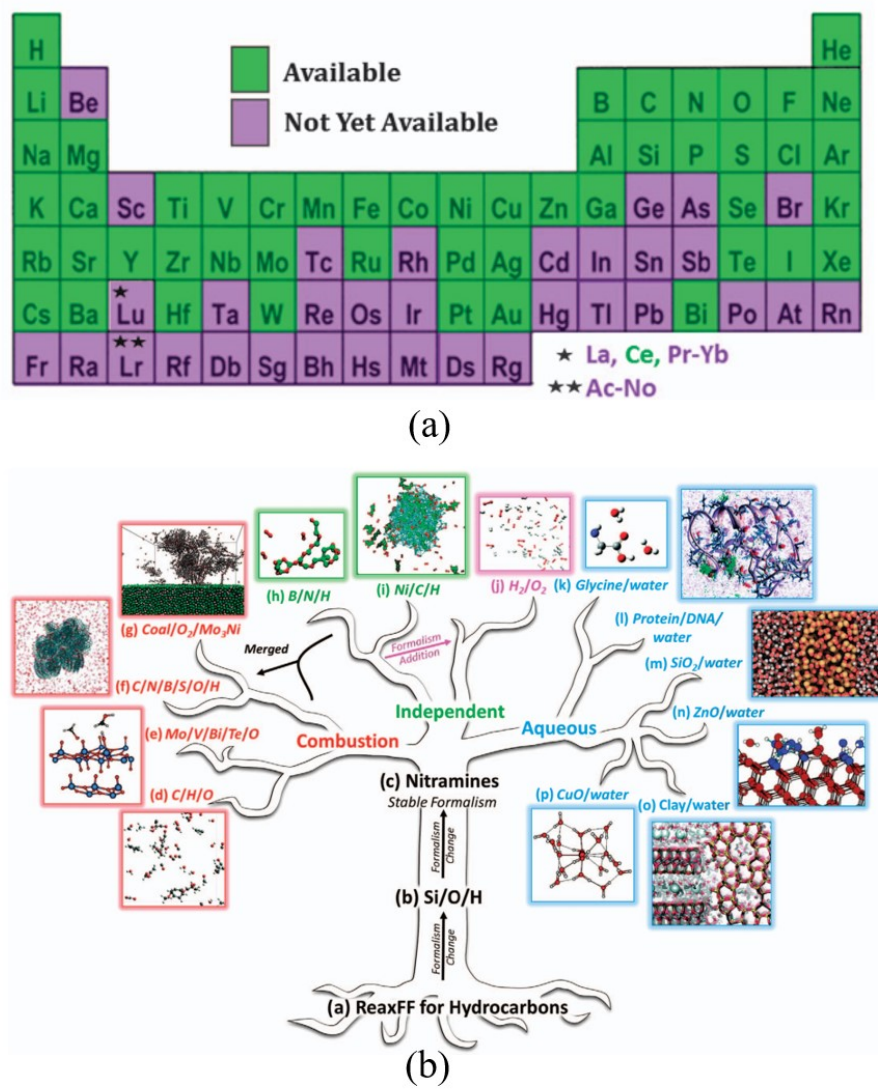

Figure 6. (a) Periodic table showing the elements with ReaxFF parameter sets and (b) ReaxFF tree [109].

The parameter sets within the combustion branch or the aqueous branch are *intra*-transferable but not *inter*-transferable [109]. Thus, while performing MD simulation one should be careful enough not to intermix the parameter sets between the branches which makes the analysis questionable. Our research falls under the independent branch (B/C/H) of the ReaxFF tree.

Energy Minimization

Energy minimization is performed to optimize the structure based on the input atomic coordinates which will bring the system into the configuration having local minimum potential energy. There are several minimization algorithms that are available as part of LAMMPS *min_style* such as conjugate gradient (*cg*) Polak-Ribiere version, Hessian-free truncated Newton algorithm (*hftn*), steepest descent algorithm (*sd*), damped dynamics method (*quickmin* or *fire*) [112]. One should be careful enough to choose the correct time step for any minimization technique since a longer timestep might move the structure far away from the minimum. Also, a very small time step will take longer optimization times. It is advisable to choose the steepest-descent method followed by the conjugate gradient method if the structure is far away from the minimum [113]. For our purpose we have used the conjugate gradient optimization technique since we have started with the *ab-initio* optimized geometry and tried to scan for the SW σ parameter that can stabilize the optimized structure. As the Polak-Ribiere version of conjugate gradient is considered to be one of the most effective minimization algorithms and has been integrated into the LAMMPS, we have made use of this minimization style. Whatever, the style of minimization the fundamental principle is to minimize the total potential energy of the system which can be expressed as [112]

$$E_{Total} = \sum_{i,j} E_{pair}(r_i, r_j) + \sum_{ij} E_{bond}(r_i, r_j) + \sum_{ijk} E_{angle}(r_i, r_j, r_k) +$$

$$\sum_{ijkl} E_{dihedral}(r_i, r_j, r_k, r_l) + \sum_{ijkl} E_{improper}(r_i, r_j, r_k, r_l) + \sum_{i} E_{fix}(r_i)$$

Where $E_{pair}(r_i, r_j)$= Pairwise interaction (Non-bonded and long-range Columbic)

$E_{bond}(r_i, r_j)$= Bonded interactions

$E_{angle}(r_i, r_j, r_k)$= Angular interactions

$E_{dihedral}(r_i, r_j, r_k, r_l)$= Dihedral interactions

$E_{improper}(r_i, r_j, r_k, r_l)$= Improper interactions

$E_{fix}(r_i)$= User-defined constrained

While minimizing the total potential energy of the system the stopping criterion has to be set which can either be energy tolerance, force tolerance, no. of iterations or the no. of total force evaluations. The criterion chosen for our research purpose is detailed in the SW-Potential Optimization section. Details regarding the use of minimization style can be found in the LAMMPS user documentation [112]. Also, a more detailed description regarding the minimization algorithms can be sought in these computational chemistry references [114–116].

Hybrid Reverse Monte Carlo (HRMC) Technique

The HRMC method is used to generate the structures of amorphous materials based on the fitting of experimental diffraction information and the minimization of the system energy using an interatomic potential [117]. It has been used to study the structural properties of amorphous carbon [118–120] and silicon [121] using the interatomic potentials like Environment-Dependent Interatomic potential (EDIP) and SW. HRMC minimizes the error function χ which includes the cost function of each experimental constraint and the energy

penalty term for every random displacement of atoms. Figure 7 shows the inner working of the HRMC simulation. The error function fitting includes the constraints like *g(r)*, *S(q)*, bond angle distribution, coordination, and pore volume constraint which are obtained from the experiments. The starting structure which is subjected to the fitting can be either user-defined initial configuration or the random configuration of the atoms. Then a choice is made either to use HRMC or simply the Reverse Monte Carlo (RMC) based on whether to use the potential energy constraint or not. In our case, we have incorporated the SW potential of the boron carbide which was optimized specifically for the icosahedral geometry found in the crystal structure of boron carbide and elemental boron.

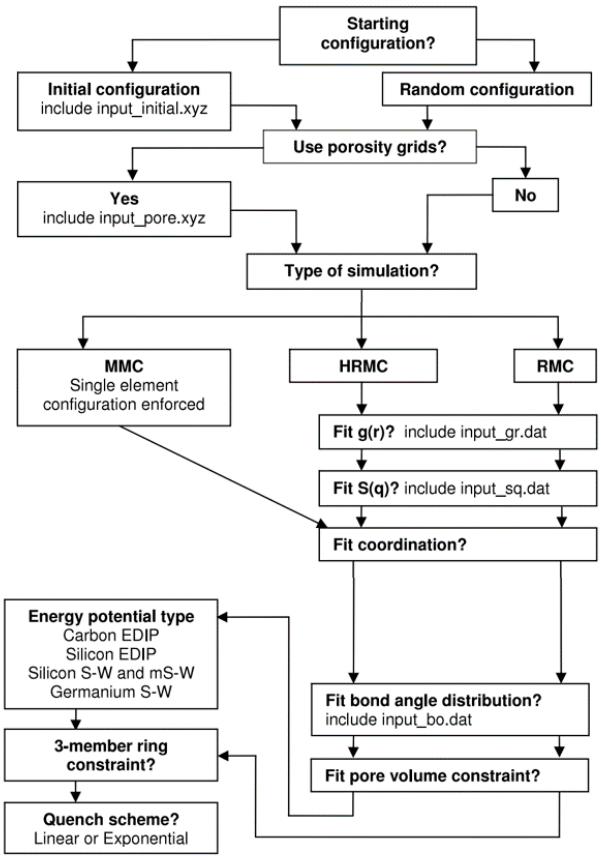

Figure 7. A general working algorithm for HRMC simulation [6].

Now, during the fitting process before any random atomic movement is made, the initial total value of χ [122] is calculated as

$$\chi_{Old,total} = \sum_i \left[\frac{\left(\mathrm{S}(Q_i)_{exp} - \mathrm{S}(Q_i)_{old}\right)^2}{\sigma(Q_i)^2} + \frac{\left(\mathrm{g}(r_i)_{exp} - \mathrm{g}(r_i)_{old}\right)^2}{\sigma(r_i)^2} \right] + \frac{E_{Old}}{k_B T}$$

Here *S(Q)* and *g(r)* are the structure factor and radial distribution function which are obtained from the diffraction experiments. σ represents the uncertainty in i^{th} data point and $k_B T$ is the Boltzmann weighting factor [123]. These weighting factors influence the acceptance probabilities in the HRMC simulation. After the atomic movement, a new total cost function $\chi_{Old,total}$ is calculated and compared with the old one. An atomic movement is accepted if $\chi_{New,total} < \chi_{Old,total}$ and conditionally accepted for $\chi_{New,total} > \chi_{Old,total}$ with the probability$P = exp\left(\chi_{Old,total} - \chi_{New,total}\right)$ [121,122].

COMPUTATIONAL DETAILS

SW-Potential Optimization

Stillinger-Weber (SW) potential parameters for Boron-Boron interactions have been developed by Rasband et al. [124] for B-Si, Dugan et al. [46] for B-C and Moon et al. [98] for B-N. SW potential parameter for boron carbide by Dugan et al. [46] was optimized for stable boron clusters which when applied on icosahedral boron carbide nanoribbon system results in the loss of icosahedral symmetry leading to structural deformation at the temperature of 300 K retaining the structure only at 1 K [125]. Hence, existing B-B interaction σ and $cos\theta_o$ parameters have been optimized for an icosahedral system using potential energy minimization. SW potential σ parameter by Dugan et al. was kept constant at 1.418 for all the B-B and C-C interaction affecting the bond lengths of the interacting system. In this study, the σ parameter for the B-B interaction is tuned with energy minimization performed using classical potential utilizing LAMMPS [102] with an average B-B bond length as the criteria for the choice of parameter. Since icosahedral B_{12} is the building block of bulk boron and boron carbide structure the average bond length is fitted for α-B_{12} structure. The icosahedral B_{12} structure has ~ 39 % of the bond angle in between 58°-61° and ~ 38 % in between 107°-109° with ~ 20 % concentrated at 109°. Thus, the angular cutoff in the SW potential was changed to regular the tetrahedral angle. Then, a supercell of 216 B atoms was constructed from the hexagonal unit cell of α-B_{12} structure [29]. Conjugate gradient style potential energy minimization was performed on the structure with 5.0e-4 time step, 0.0 energy tolerance, 1.0e-8 force tolerance, 10^4 steps of maximum iterations and 10^6 number of force evaluations. This criterion allows terminating the energy minimization process either with the force tolerance/evaluations or with the maximum no. of iterations defined. This process was applied for all the SW potential σ parameter varied from 1.15 to 1.80.

The input script for SW potential optimization can be found in appendix. Figure 8 shows the force norm variation with the no. of iterations for the σ values from 1.15 to 1.80 with the step size of 0.05 where all of the minimization ends below 1000. Although not all the data points are shown in Figure 8 it should be noted however that the iteration in between the data points ended below 1000. All of the minimization iterations terminated before the maximum no. of 10^4 steps was reached with force tolerance criterion with an exception of sigma values 1.38 and 1.39. For these two values of sigma we raised the ceiling to 10^5 steps of maximum iterations and both of them terminated below 10^5 steps by satisfying the force tolerance criterion like rest of the data points. Then the average bond length B-B of the DFT optimized structure is compared with the SW minimized structure to calculate the difference in the average bond length of the resulting structure. The average B-B bond length (d_{avg}) of the DFT optimized α-boron structure is 1.7705 Å which is same as the literature value reported by Decker et al. [31] and Katada et al. [32] in icosahedra.

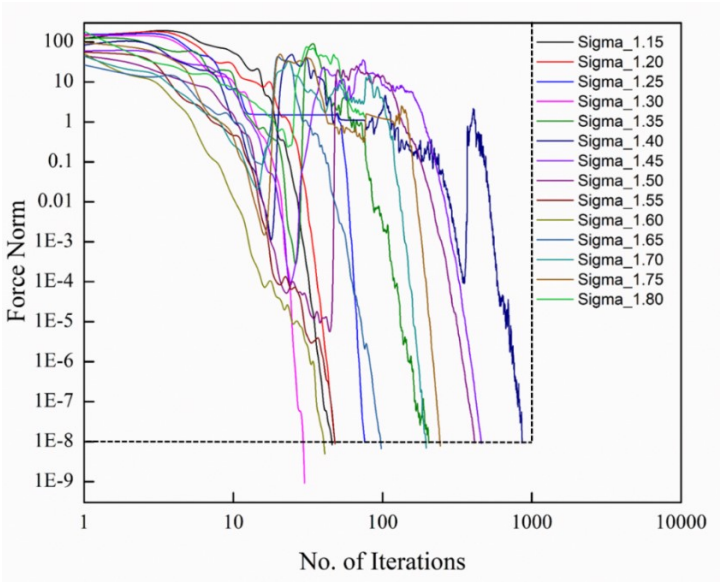

Figure 8. Force norm variation with the no. of iterations. Both the axis are expressed in log scales.

Amorphous Boron Carbide – MD

Amorphous models of B_{12}-(CCC), B_{12}-(CBC) and $B_{11}C_p$-(CBC) were studied using the New SW and ReaxFF potentials in the LAMMPS simulation package as shown in Figure 9. To study the short-range order of icosahedrons in the matrix of boron and carbon atoms as seen in the smaller theoretical models and experimentally studied samples we packed icosahedrons and chain atoms in a box with the random arrangement. In order to make the three a-B_xC samples, 729 units of icosahedrons and chain atoms containing 10935 atoms were packed randomly inside the simulation cell of dimension ~ (45.80 X 45.80 X 45.80) $Å^3$ with the minimum distance between the atoms to be 1.9 Å using PACKMOL [126]. The initial density of all the packed disordered structures was ~ 0.114 atoms/$Å^3$ (~ 2.09 g/cm^3).

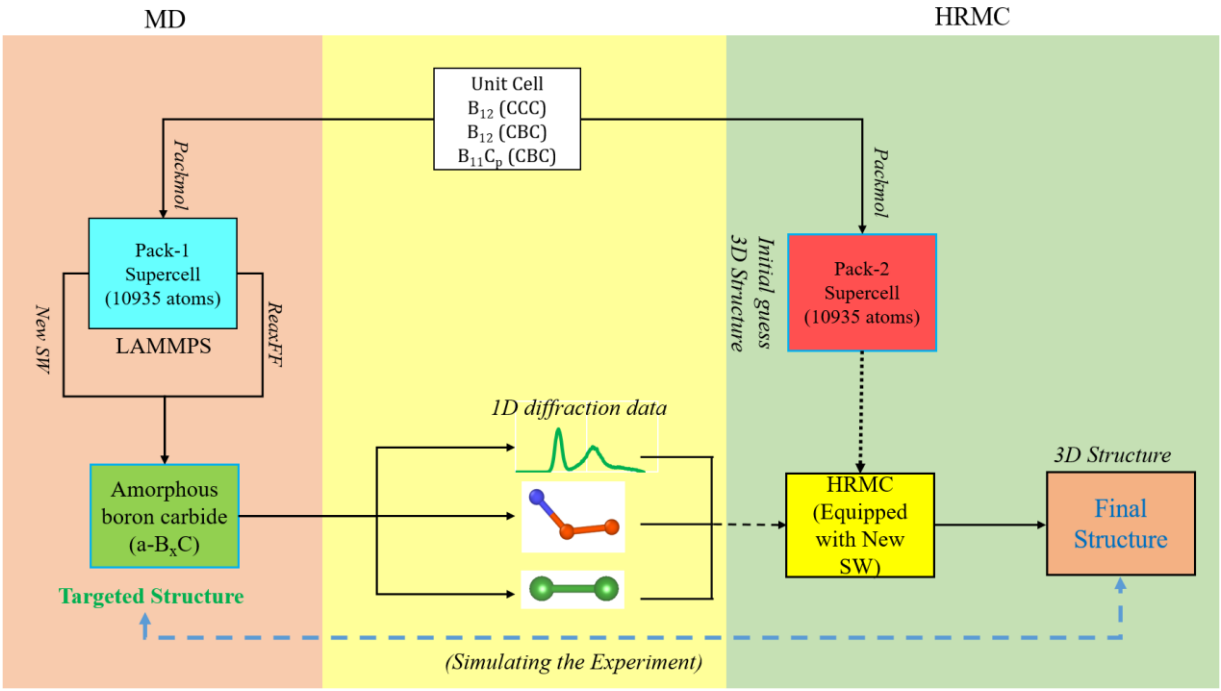

Figure 9. A flow chart for modeling the amorphous boron carbide using MD and HRMC.

Classical MD simulation was performed using New SW and ReaxFF potential on these samples with periodic boundary conditions applied in all three directions as shown in the flow chart of Figure 10. The three initial randomly packed models of boron carbide were subjected to constant pressure and temperature (NPT) simulation using the ReaxFF potential for 42.5 ps from 10 K to 300 K with 0 Gpa and equilibrated at 300 K for 82.5 ps with the time step of 0.25. With the New SW potential, we applied a pressure scheme as shown in Figure 11 where constant volume and temperature (NVT) and NPT simulations with different pressures applied with the goal of matching the density. This scheme was applied to densify the structure using New SW to get reasonably close to the density of the ReaxFF model produced earlier and to compare the short-range order characteristics among the models. Here, firstly NVT simulation was performed for 50 ps at 300 K followed by NPT simulation at 300 K with varying pressure from 0 Gpa to 20 Gpa for 550 ps. It is important to note that the final structure is free from residual stress since it was released with the NPT simulation at zero pressure. The input LAMMPS scripts for generating a-B_xC can be found in the appendix section. A similar approach has been found in the literature and applied to get the desired density of the material for comparison to the experiment [76]. The six different a-B_xC models were prepared using two different interatomic potentials and compared. These models are compared in terms of their final density (ρ), bond angle distribution ($B(\theta)$), radial distribution function ($g(r)$), structure factor ($S(Q)$) and the bonding environment.

Amorphous Boron Carbide – HRMC

HRMC simulation is employed to reconstruct the amorphous models of boron carbide prepared using the MD simulation detailed above. The radial distribution function and static

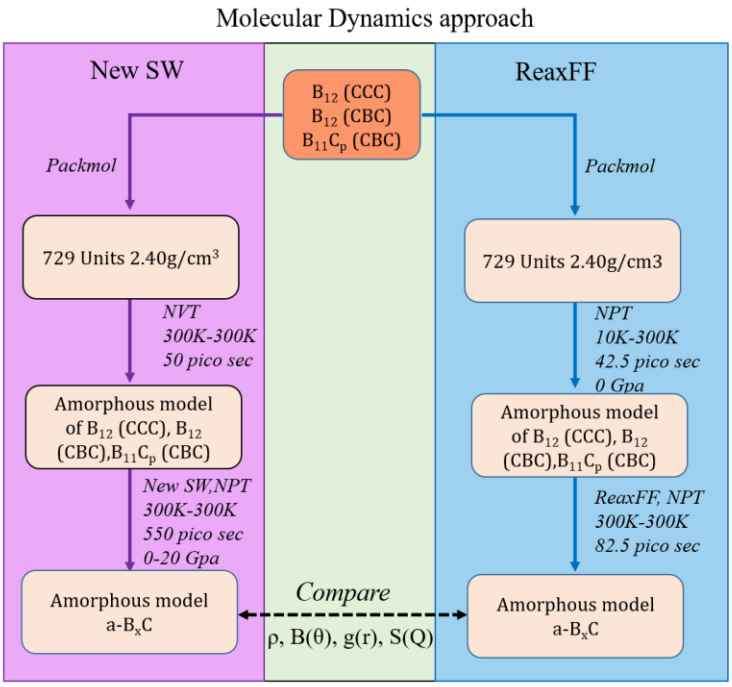

Figure 10. Flow chart showing the MD approach used for generating amorphous boron carbide using New SW and ReaxFF.

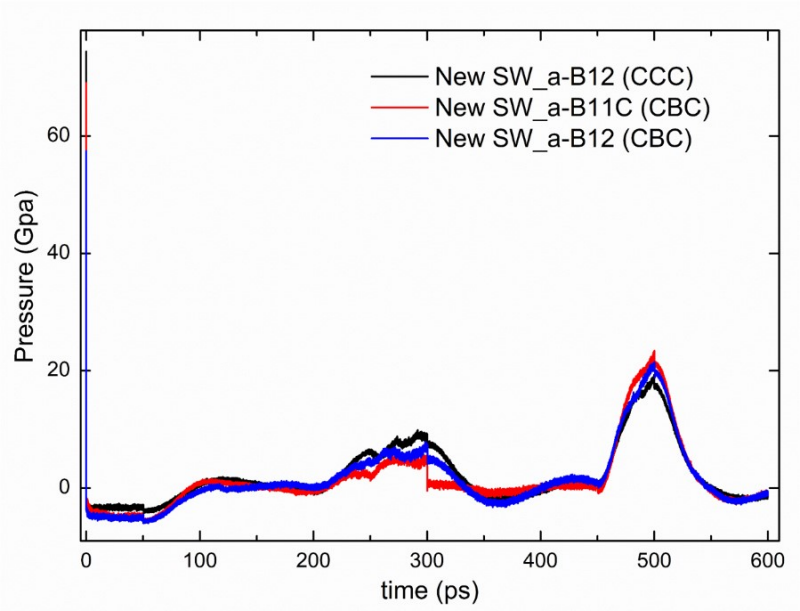

Figure 11. Pressure scheme applied for generating amorphous boron carbide models using New SW potential.

structure factor are calculated from the previous MD models of a-B_xC and used in place of experimental constraints within HRMC. The 3D reconstruction of the amorphous models of materials based only on 1D diffraction data is challenging for HRMC simulations [127]. Even if we apply multiple constraints along with diffraction data fitting in the simulation process to find the 3D atomic structure starting from the completely random configuration of atoms, the solution will be different after every simulation because of a huge family of solution. So, to fit the structure with the diffraction data, the initial starting model cannot be a random collection of atoms. As suggested in the previously discussed literature of amorphous boron carbides where icosahedrons are in the matrix of boron and carbon atoms, we packed another set of icosahedrons and chain atoms randomly in the simulation cell as initial starting configuration for HRMC simulation.

In this HRMC study, we have packed 729 icosahedrons and chain atoms with the minimum tolerance distance of 1.9 Å in a simulation cell of dimension (43.37 X 43.45 X 43.40) $Å^3$ to contain 10935 atoms as shown in the flow chart of Figure 9. This structure was energetically minimized at 300 K for 2 x 10^6 steps using New SW equipped potential in the HRMC code to find the local minimum of the Potential Energy Surface (PES). The output is then fitted with the calculated diffraction data together with the potential constraint. The two-stage HRMC modeling approach has been previously applied in predicting the structure of amorphous materials [127,128]. The output structure of stage-1 is fitted with *S(Q)*, *g(r)* and *B(θ)* along with the average bond length, and coordination histogram constraint since at least four constraints are recommended for multi-element HRMC simulation [129]. A quenching approach is used during the fitting process which starts from 1000 K and is linearly quenched down to 800 K, 500 K, and 300 K in four subsequent stages where every stage takes 25 % of the total simulation steps. All

the HRMC simulations are carried out for 10^7 steps to generate the fitted amorphous models. The HRMC input parameter script has been added as a part of the appendix.

Amorphous Hydrogenated Boron Carbide – MD

Amorphous models of a-B_xC:H_y was produced using the Molecular dynamics simulation using the LAMMPS platform with ReaxFF potential. The starting initial structure is prepared using the repetitive *ortho*-carborane molecule with the CH_2 linkers added randomly in between. The choice of CH_2 as a network former between the dehydrogenated *ortho*-carborane is based on the nuclear magnetic resonance (NMR) study presented by Paquette et al. [67]. A total of 640 *ortho*-carborane are used in the system except for the Model-B6 where 1000 of *ortho*-carborane were used. At first B/C stoichiometry in the initial structure is maintained by adding the CH_2 linkers in between the *ortho*-carborane molecules. Secondly, the H % in the starting structure was matched to that of the experimental thin film samples by randomly removing the H-atoms attached to B-atoms in the *ortho*-carborane molecules following the comments from the earlier experimental investigation [67]. When H-atoms were removed from the *ortho*-carborane it was removed only from the boron site but not the carbon site as no icosahedral carbon bonding was seen during the experimental characterization. The stoichiometry of all the 15 samples made during the process is listed in Table 2 in the order of decreasing H % in the structures. Then, we applied the densification scheme as shown in Figure 12 to simulate the amorphous hydrogenated boron carbide (a-B_xC:H_y) models reproducing the simulated model density as in the experimental samples. At first, NVT simulation is performed at 300 K followed by the NPT simulation at 500 K. During the NPT simulation external pressure is applied to the simulation cell in order to densify the structure. Depending upon the already published experimental density the applied

Table 2. Amorphous hydrogenated boron carbide models and their stoichiometry and density. Where LC = Linker CH_2, AP = Applied pressure, Calc = Calculated, Exp = Experimental.

Model								Density (g/cm^3)	
No.	Structures	LC	Total	H %	B/C	B/H	AP (Gpa)	Calc	Exp
1	Model-D11	220	13600	42	4.27	1.12	20.27	0.97	0.98
2	Model-D22	220	13300	41	4.27	1.19	40.53	1.27	1.27
3	Model-D24	100	12665	39	4.64	1.31	30.40	1.32	1.32
4	Model-D21	0	12528	39	5.00	1.32	70.93	1.43	1.48
5	Model-E2	100	12556	38	4.64	1.34	50.66	1.42	1.44
6	Model-D13	48	12081	36	4.82	1.47	25.33	1.40	1.40
7	Model-D12	168	12086	35	4.42	1.51	20.27	1.40	1.41
8	Model-D2	0	11630	34	5.00	1.62	25.33	1.48	1.50
9	Model-D5	66	11341	32	4.75	1.78	18.24	1.55	1.58
10	Model-D23	45	11147	31	4.83	1.87	20.27	1.61	1.56
11	Model-D8	20	10852	29	4.92	2.03	20.27	1.65	1.64
12	Model-B1	40	10153	24	4.85	2.63	11.15	1.73	1.75
13	Model-D26	78	9698	20	4.71	3.30	8.11	1.80	1.80
14	Model-B6	465	15385	19	4.06	3.00	8.11	1.83	1.83
15	Model-B3	132	9318	16	4.53	4.00	25.33	2.16	2.13

pressure was varied from ~ 8 Gpa to ~ 71 Gpa. The resulting structure is then potential energy minimized with conjugate gradient type minimization for 5000 steps of maximum iteration with zero energy tolerance (*etol*) and 1.0e-8 force tolerance (*ftol*) in order to bring the atoms into their local minimum position. And finally, the minimized structure is subjected to NPT simulation at ambient pressure to release the remnant internal stress present in the structure. This MD simulation script for this modeling scheme can be found in the appendix section. With this approach, we were able to prepare different models corresponding to the experimental sample

having the density within 2 % of the experimental density and the resulting models are free from internal stress.

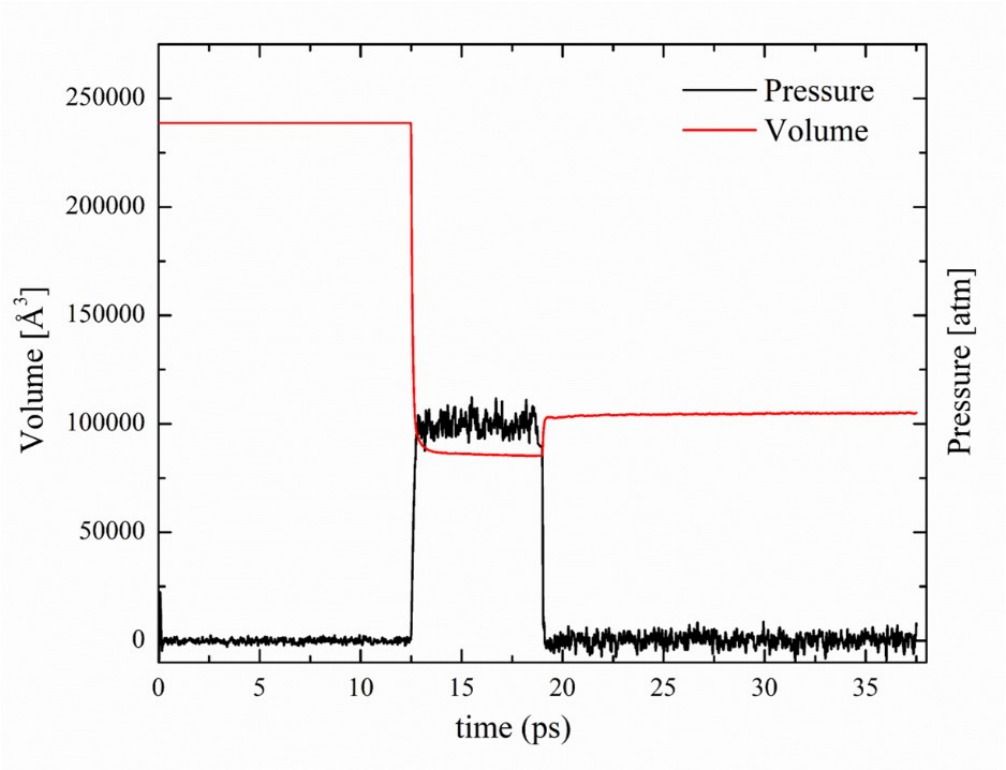

Figure 12. Densification scheme applied for generating amorphous hydrogenated boron carbide models.

RESULTS AND DISCUSSION

SW Parameters

Alpha-Rhombohedral Boron. Figure 13 shows the plot of the variation of the σ parameter with the modulus of difference in the average bond lengths between the unrelaxed and the SW relaxed structures. Below 1.65, the icosahedral structure contracts resulting in the increased error in bond length. And above 1.65, the icosahedral structure expands moving away from the d_{avg} value of α-boron. At the original SW σ value of 1.418, d_{avg} was found to be 1.53144 Å with the difference of 0.23901 Å whereas, with the new optimized σ value of 1.65, d_{avg} was calculated to be 1.77259 Å with the difference of only 0.0021 Å. Hereafter the SW parameter by Dugan et al. will be called the Old SW and the modified form with σ=1.65 and θ_o= 109.47° will be called henceforth the New SW.

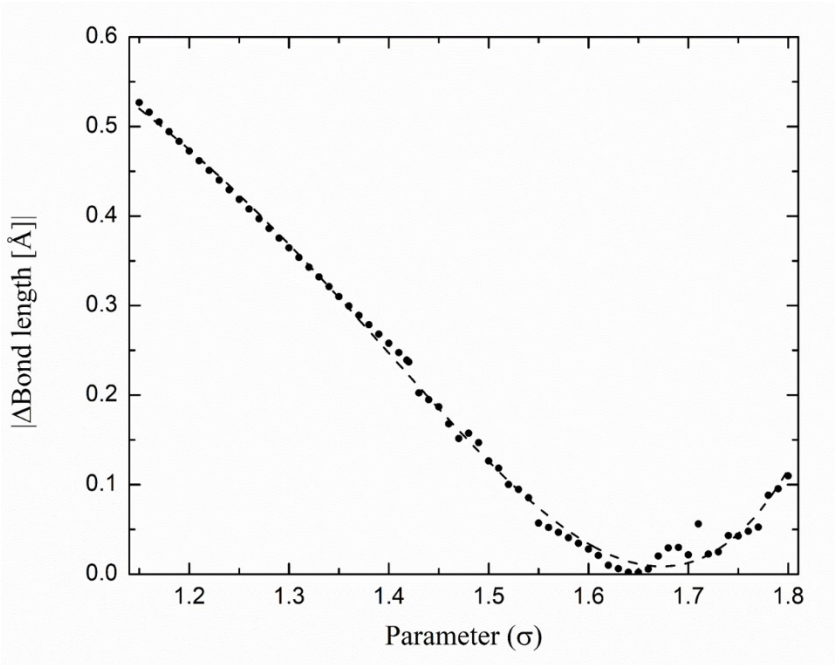

Figure 13. The difference in average bond length of SW minimized α-boron structure with the variation of the SW potential σ parameter.

For both the Old and the New SW, the B-B interaction parameters were used to predict the average bond length of the boron clusters ranging from B_7 to B_{80}. The structural relaxation of stable boron clusters B_7, B_{10}, B_{14}, B_{16}, B_{18} [130], B_{12}, B_{20}, B_{26}, B_{80} [131], B_{44} [132] was performed as described earlier and the average bond lengths computed and compared against the DFT calculated values as listed in Table 3. During minimization, the structural geometry is conserved with only a change in bond lengths between the boron atoms. As seen from Table 3 bond length error due to Old SW in all the cases of boron clusters are found to be greater than 0.22 Å and bond length error in case of the New SW are lower than 0.05 Å. Overall, the d_{avg} results obtained with the New SW B-B interaction parameters are in good agreement with the Ab initio values for boron clusters.

Table 3. Average bond lengths of boron clusters calculated using Old SW, New SW and Ab initio generated structures. Where n = Boron clusters, OSW = Old SW, NSW = New SW.

	Average bond length (Å)			|Δ Bond Length (Å)|	
n	Abinitio ($d_{o,avg}$)	OSW ($d_{old,avg}$)	NSW ($d_{new,avg}$)	$\lvert d_{o,avg} - d_{old,avg} \rvert$	$\lvert d_{o,avg} - d_{new,avg} \rvert$
B_7	1.6937	1.43882	1.64993	0.25488	0.04377
B_{10}	1.68781	1.42711	1.6423	0.2607	0.04551
B_{12}	1.68244	1.42987	1.64885	0.25257	0.03359
B_{14}	1.68492	1.43167	1.65001	0.25325	0.03491
B_{16}	1.68621	1.44034	1.65651	0.24587	0.0297
B_{18}	1.68504	1.43764	1.65573	0.2474	0.02931
B_{20}	1.6671	1.42412	1.63849	0.24298	0.02861
B_{26}	1.69544	1.47123	1.69597	0.22421	0.00053
B_{44}	1.68158	1.44938	1.66898	0.2322	0.0126
B_{80}	1.71349	1.46555	1.69089	0.24794	0.0226

Boron Carbide Crystal. Boron carbide crystal is a complex crystal structure where different bond angles are present for different variants as shown in Figure 3. The three-body angular cut off ($cos\theta_{oijk}$) in the SW potential will be different for the different crystal structures of boron carbide. For the two-element system, there are three two-body pairs namely B-B, C-C, and B-C. There are eight combinations of three-body parameters namely B-B-B, C-C-C, B-C-C, C-B-B, B-B-C, C-B-C, C-C-B and B-C-B where the first atom is the central atom with others on two sides. Here, all the three body angular cutoffs ($cos\theta_{oijk}$) are obtained from the crystal structure of boron carbide and cutoffs for linear chains- such as CCC and CBC chain is used a value of 180^o in all the variants of boron carbide. If the particular angular type is missing in the crystal structure eg. C-B-C in B_{12}-(CBC) then regular tetrahedral angular cutoff is used. σ is kept constant at 1.65 for three-body pairs B-C-C and C-B-B whose second and third elements are the same. All other parameters for B-C-C and C-B-B are the same as that of Dugan et al. [46]. The parameters ε and λ for the three-body interactions with different second and/or third elements e.g. for B-C-B are calculated using the geometric parameter mixing rule i.e., $\varepsilon_{B-c-B} = \sqrt{\varepsilon_{B-B}\varepsilon_{B-C}}$ and $\lambda_{B-c-B} = \sqrt{\lambda_{B-B}\lambda_{B-C}}$. This rule has been widely used to calculate cross parameter terms in LJ potential as Berthelot rule [133]. The other parameters, namely, *A, B, p, q, σ, a, γ* of B-C-B type three-body interaction are assumed to be negligible and set to zero following the LAMMPS documentation [134]. The complete set of parameters we obtained using the above-discussed methodology for B12-(CCC) are listed in Table 4. The tol parameter in the last column is defined in LAMMPS for further optimization for the cutoffs [134]. The SW potential parameters for B12-(CBC) and B11Cp-(CBC) are given in Table 5 and Table 6 respectively. The potential energy plots of the two body SW potential energy comparisons between the Old SW and the New SW for all the interactions present in the boron carbide system

namely B-B, B-C and C-C are shown in Figure 14. The potential well minimum shifts towards a longer separation for the New SW in case of both the B-B and B-C interactions whereas the C-C curve remains unaffected.

Table 4. SW potential parameters for B_{12}-(CCC) used in LAMMPS. The values of three variables *p*, *q*, and *tol* after *B* are all zero except for the first four rows where *p* values are equal to 4.00.

Pairs	ε	σ	a	λ	γ	$cos(\theta_o)$	A	B
B-B-B	1.00	1.650	1.8179	1.00065	0.32408	-0.3333	13.4487	0.08477
C-C-C	1.00	1.418	1.8945	18.70790	1.20000	-1.0000	5.37900	0.50820
B-C-C	1.00	1.650	1.8562	4.32667	0.62362	-1.0000	8.50533	0.20756
C-B-B	1.00	1.650	1.8562	4.32667	0.62362	-0.4226	8.50533	0.20756
B-B-C	1.00	0.000	0.0000	2.08074	0.00000	-0.4695	0.00000	0.00000
C-B-C	1.00	0.000	0.0000	8.99683	0.00000	-0.2250	0.00000	0.00000
C-C-B	1.00	0.000	0.0000	8.99683	0.00000	-0.2250	0.00000	0.00000
B-C-B	1.00	0.000	0.0000	2.08074	0.00000	-0.4695	0.00000	0.00000

Table 5. SW potential parameters for B_{12}-(CBC) used in LAMMPS. Angular cutoff: C-B-B = 117°, B-B-C= 122°, C-B-C absent so 109.47° used a cutoff, C-C-C and B-C-C are chain structures and 180° used although C-C-C was absent in this crystal structure.

Pairs	ε	σ	a	λ	γ	$cos(\theta_o)$	A	B
B-B-B	1.0	1.650	1.8179	1.00065	0.32408	-0.3333	13.4487	0.08477
C-C-C	1.0	1.418	1.8945	18.70790	1.20000	-1.0000	5.37900	0.50820
B-C-C	1.0	1.650	1.8562	4.32667	0.62362	-1.0000	8.50533	0.20756
C-B-B	1.0	1.650	1.8562	4.32667	0.62362	-0.4540	8.50533	0.20756
B-B-C	1.0	0.000	0.0000	2.08074	0.00000	-0.5299	0.00000	0.00000
C-B-C	1.0	0.000	0.0000	8.99683	0.00000	-0.3333	0.00000	0.00000
C-C-B	1.0	0.000	0.0000	8.99683	0.00000	-0.3333	0.00000	0.00000
B-C-B	1.0	0.000	0.0000	2.08074	0.00000	-0.5299	0.00000	0.00000

Table 6. SW potential parameters for $B_{11}C_p$-(CBC) used in LAMMPS. Angular cutoff: C-B-C = Absent, B-C-C chain = 180°, All the three-body interaction C-B-B, B-B-C, C-B-C, C-C-B, and B-C-B distributed around the tetrahedral angle. So, the tetrahedral cutoff is used for all.

Pairs	ε	σ	a	λ	γ	$cos(\theta_o)$	A	B
B-B-B	1.00	1.650	1.8179	1.00065	0.32408	-0.3333	13.4487	0.08477
C-C-C	1.00	1.418	1.8945	18.70790	1.20000	-1.0000	5.37900	0.50820
B-C-C	1.00	1.650	1.8562	4.32667	0.62362	-1.0000	8.50533	0.20756
C-B-B	1.00	1.650	1.8562	4.32667	0.62362	-0.3333	8.50533	0.20756
B-B-C	1.00	0.000	0.0000	2.08074	0.00000	-0.3333	0.00000	0.00000
C-B-C	1.00	0.000	0.0000	8.99683	0.00000	-0.3333	0.00000	0.00000
C-C-B	1.00	0.000	0.0000	8.99683	0.00000	-0.3333	0.00000	0.00000
B-C-B	1.00	0.000	0.0000	2.08074	0.00000	-0.3333	0.00000	0.00000

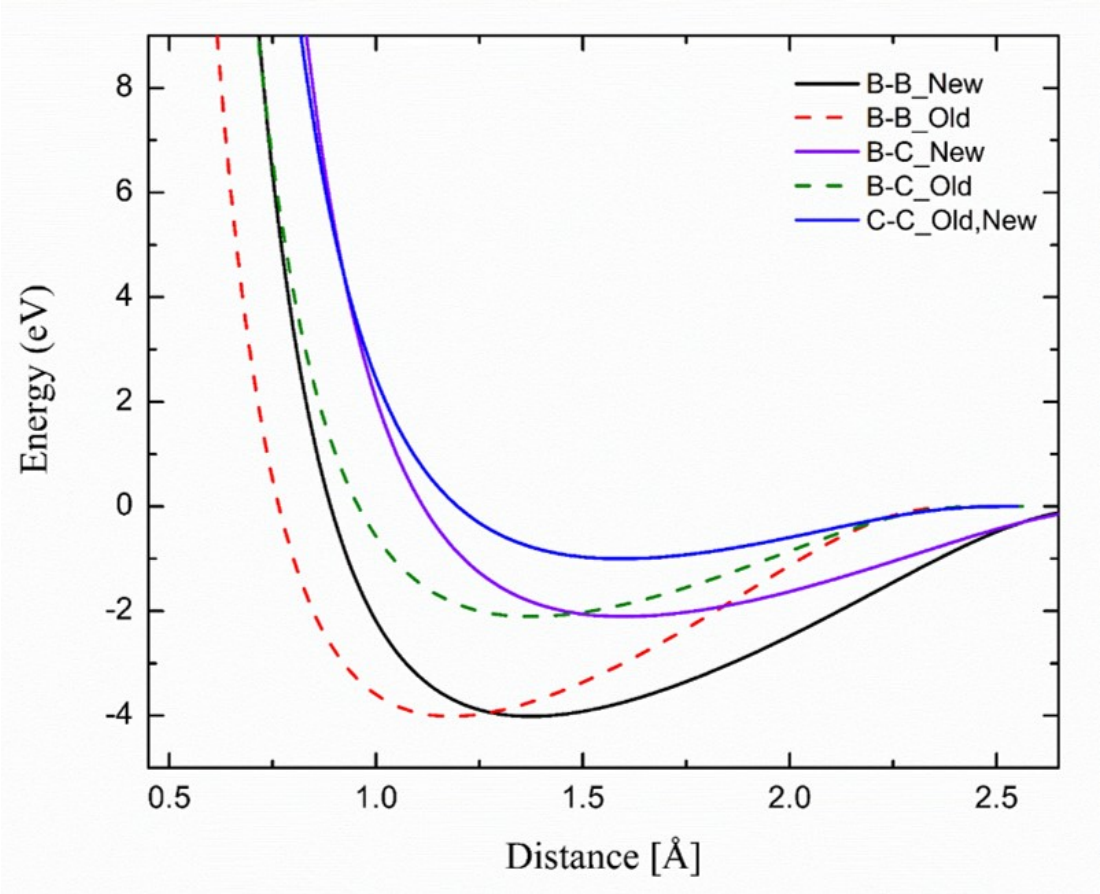

Figure 14. Stillinger-Weber potential two-body energy for B-B, B-C and C-C bonds comparison between Old SW and New SW parameters.

The shift in B-B is ~ 0.21 Å and B-C is ~ 0.12 Å which is due to the change in the length scaling parameter σ parameter from 1.418 to 1.65 which ultimately changes the two-body cutoff $a\sigma$. The shift in the potential is responsible for predicting the correct bond lengths for the boron carbide system with the New SW parameters compared to Old SW. The DFT optimized structures of B_{12} [29], B_{12}-(CCC) [135], B_{12}-(CBC) [136] and $B_{11}C_p$-(CBC) [5] were potential energy minimized as described above using the New SW, Old SW and ReaxFF potential [110]. Table 7 shows the d_{avg} predicted by DFT, ReaxFF, New SW and Old SW potential for all the bonds present in the structures.

Table 7. Average bond length comparison of B_{12}, B_{12}-(CCC), B_{12}-(CBC), B_{12}-(CBC) and B_{11}Cp-(CBC) predicted using DFT, ReaxFF, New and Old SW potential.

Bond Lengths	Process	B_{12}	B_{12}-(CCC)	B_{12}-(CBC)	$B_{11}C_p$-(CBC)
B-B	DFT	1.77	1.773	1.799	1.732
	ReaxFF	1.807	1.756	1.771	1.761
	New SW	1.798	1.731	1.78	1.762
	Old SW	1.531	1.559	1.557	1.551
B-C	DFT	-	1.664	1.562	1.659
	ReaxFF	-	1.711	1.611	1.644
	New SW	-	1.721	1.664	1.633
	Old SW	-	1.708	1.674	1.551
C-C	DFT	-	1.333	-	-
	ReaxFF	-	1.292	-	-
	New SW	-	1.693	-	-
	Old SW	-	1.7	-	1.633

From Table 7 it can be seen that the B-B bond length of the DFT optimized structure is very close to that of ReaxFF and New SW minimized structures with an error of ~ ± 0.02 Å.

Whereas, Old SW predicted a B-B bond length for the structure ~ 0.22 Å smaller than the DFT relaxed structure. This is due to the contraction of the icosahedral structure due to the Old SW B-B potential parameters. The B-C bond length is over-approximated by all the potentials in the case of B_{12}-(CCC) and B_{12}-(CBC) in comparison to DFT optimized geometry. In the case of the $B_{11}C_p$-(CBC) crystal structure, the B-C bond length prediction by ReaxFF and New SW potential are 1.644 Å and 1.633 Å respectively which is very close to that of DFT value 1.659 Å. In comparison, the Old SW generated relaxed structure yields the B-C length of 1.551 Å which is much shorter in comparison to that from the New SW potential. Although $B_{11}C_p$-(CBC) is the stable variant of boron carbide crystal, the Old SW – based minimized structure was not able to stabilize such a geometry. This further confirms our approach to model these which is quite comparable to that achieved by the ReaxFF-based minimization. In the case of Old SW during the minimization process, some of the C atoms which were initially resided in the icosahedra would leave its icosahedral site and form bonds with the CBC chain atom resulting in an increase in the C-B bond count and new C-C bond which was initially absent (see Figure 15(a)). In contrast, the C-atom remains bonded within the icosahedra during the New SW minimization (see Figure 15(b)). We should note however that the C-C bond length prediction for B_{12}-(CCC) for both the New SW and the Old SW has the same level of error as when the interaction parameters were kept unchanged except for the angular cutoff correction. Nevertheless, overall, the New SW potential of boron carbide obtained by modifying the parameters based on the icosahedral-based geometry of the crystal was able to produce results close to that of the sophisticated ReaxFF potential.

The bond angle distribution *B(θ)* is the first nearest neighbor angle histogram that can be used to measure the quality of the structure. Figure 16 shows the *B(θ)* of boron carbide crystal

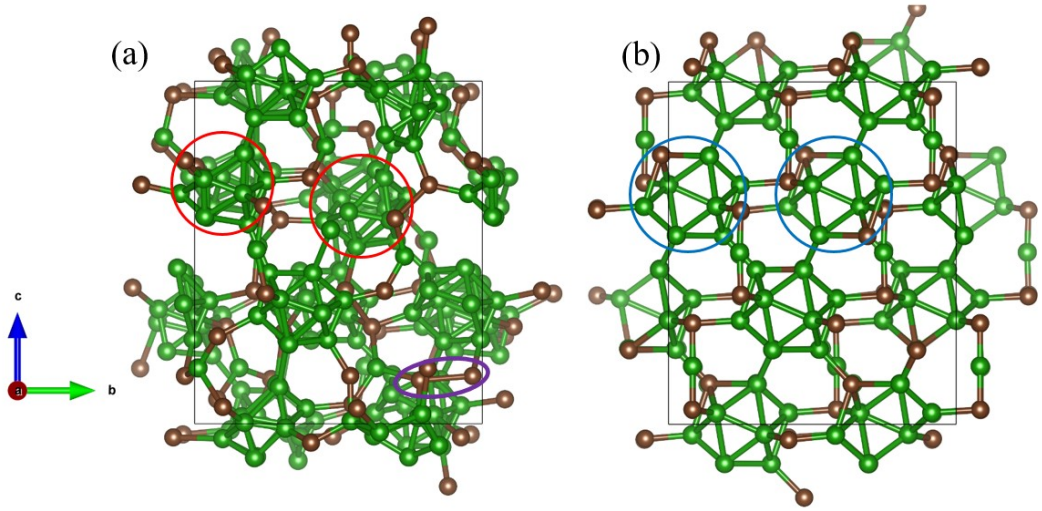

Figure 15. Old SW and New SW potential optimized structure of $B_{11}C_p$-(CBC). The icosahedral structure opened up during the minimization process for Old SW. Open icosahedral cages are circled red, Closed icosahedral cages are circled blue and C-C bond circled purple.

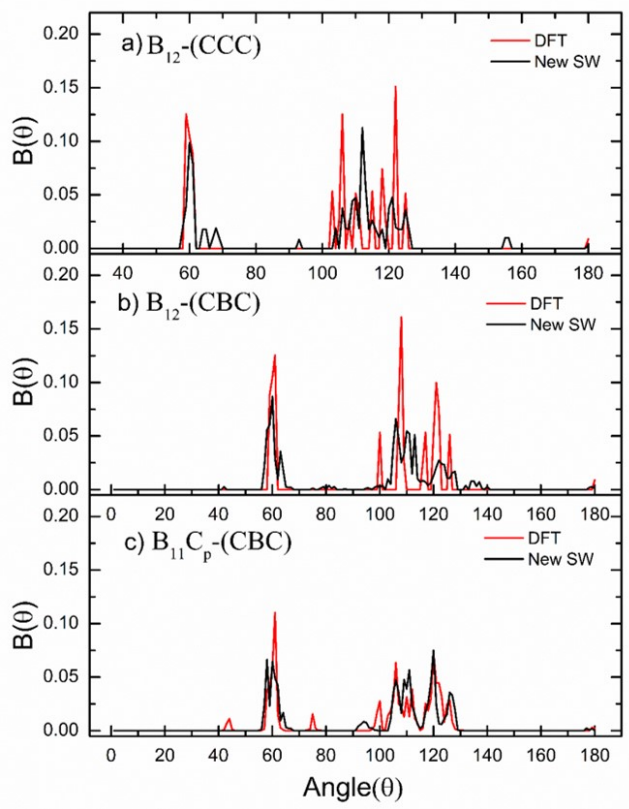

Figure 16. Bond angle distribution of DFT optimized structure compared to New SW minimized boron carbide crystal structure.

optimized using DFT and New SW potential. In all the cases, the angular distribution is centered around two peaks, one at an angle 60° and the other between 100°-130°. *B(θ)* around 60° is in good agreement in all the cases and comes from the three-membered B-atoms rings in the triangles forming icosahedrons. Small peaks at 180° in all the cases come from the atomic chains (CCC and CBC) present in the crystal structure. SW potential function is limited to only one angular cutoff ($cos\theta_{oijk}$) per three-body interaction type. It is due to this inherent limitation of SW potential function all the angular peaks present in DFT optimized structure aren't present in the SW minimized structure.

Structure of Amorphous Boron Carbide – MD

Density. The density of all the final amorphous models of boron carbide from the Molecular Dynamics simulation is listed in Table 8.

Table 8. The density of the amorphous models using ReaxFF and New SW potential.

Amorphous Samples	B-atoms	C-atoms	Density (g/cm^3)	
			ReaxFF	New SW
a-B_{12}-(CCC)	8748	2187	2.48	2.30
a-B_{12}-(CBC)	9477	1458	2.56	2.36
a-B_{11}Cp-(CBC)	8748	2187	2.53	2.37

The literature value of density of α-B_{12} is 2.476 g/cm^3 [29] which is close to the crystalline density 2.473 g/cm^3 [135] for B_{12}-(CCC). The ReaxFF generated a-B_{12}-(CCC) has a density of 2.48 g/cm^3 which is similar to its crystalline counterpart and the amorphous model a-$B_{2.5}$C and the CVD prepared film by Pallier et al. [5]. Similarly, the density of a-$B_{11}C_p$-(CBC) using

ReaxFF is found to be 2.53 g/cm^3 which is also very close to the reported crystalline density of 2.52 g/cm^3 [5,35]. However, the ReaxFF calculated density of a-B_{12}-(CBC) was the highest among all at 2.56 gm/cm^3 which is also significantly higher than the crystalline density 2.44 g/cm^3 found in the literature [136]. The density of the amorphous models predicted by the New SW is 6-7 % lower than that of ReaxFF models because of the slight increase in the interatomic distance between atoms e.g. C-C pair.

Bond Angle Distribution. For the two-element system, there are six different possible combinations of bond angles that can be present in the structure. Table 9 lists all the types of bond angles with their respective amounts present in all the three different variants of amorphous boron carbide models.

Table 9. Percentage of the angular type present in the amorphous models of boron carbide samples prepared using New SW and ReaxFF potential.

Bond	a-B_{12}-(CCC)		a-B_{12}-(CBC)		a-$B_{11}C_p$-(CBC)	
Angles	New SW	ReaxFF	New SW	ReaxFF	New SW	ReaxFF
B-B-B	94.14	84.48	96.27	82.29	93.70	64.26
B-B-C	4.78	9.49	3.09	11.33	5.14	22.03
B-C-C	0.00	0.01	0.00	0.74	0.01	1.59
C-B-B	0.10	1.43	0.09	4.41	0.19	9.98
C-B-C	0.42	2.78	0.26	1.01	0.50	2.00
C-C-C	0.24	1.44	0.00	0.00	0.14	0.00

It can be seen that the prominent angular type present in the amorphous models of boron carbide samples are B-B-B, B-B-C, C-B-B, and C-B-C. The bond angles B-C-C and C-C-C are less than 2 % in all the amorphous samples. Figure 17 shows the comparison between New SW

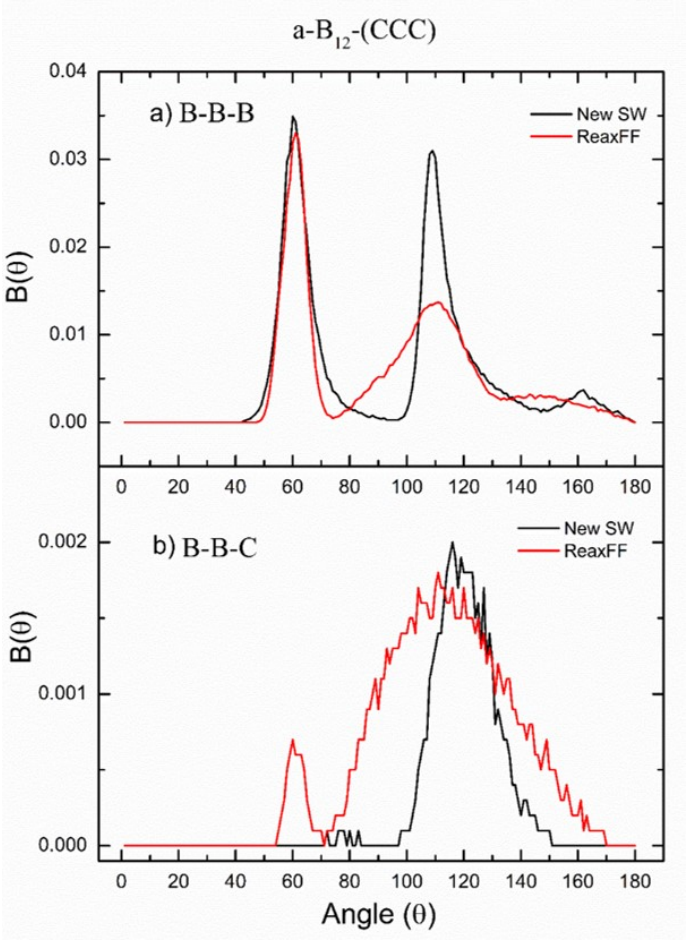

Figure 17. B-B-B and B-B-C type bond angle distribution comparison of a-B_{12}-(CCC) structure between New SW potential and ReaxFF.

and ReaxFF for the two prominent angular type B-B-B and B-B-C in a-B_{12}-(CCC) sample. It can be seen that at around 60° the distribution for B-B-B type is equivalent for both the potential whereas in the higher angular region ReaxFF allows wide distribution of angle around ~ 110° compared to SW.

The bond angle distributions of B-B-B and B-B-C types are presented in Figure 18 for two other models of boron carbide. Here, a similar observation can be made in terms of the B-B-B angle as in a-B_{12}-(CCC). However, B-B-C is more prominent in the ReaxFF generated models than before with the B-B-C angle distribution having a sharp peak at around 60° in the case of a-

$B_{11}C_p$-(CBC) structure compared to other amorphous models. The origin of this peak comes from the fact that one of the C atoms in the structure is a part of icosahedra forming near equilateral angles with B atoms. The absence of this prominent peak in the New SW created model indicates that some of the C atoms in the icosahedra are leaving the site and forming the bonding with the other atoms. In fact, it is seen in Table 9 as a C-C-C angle which is absent in the ReaxFF generated model. This strong peak could potentially be used as a signature to identify whether or not C-atom is within the icosahedral sites in the unknown amorphous boron carbide sample.

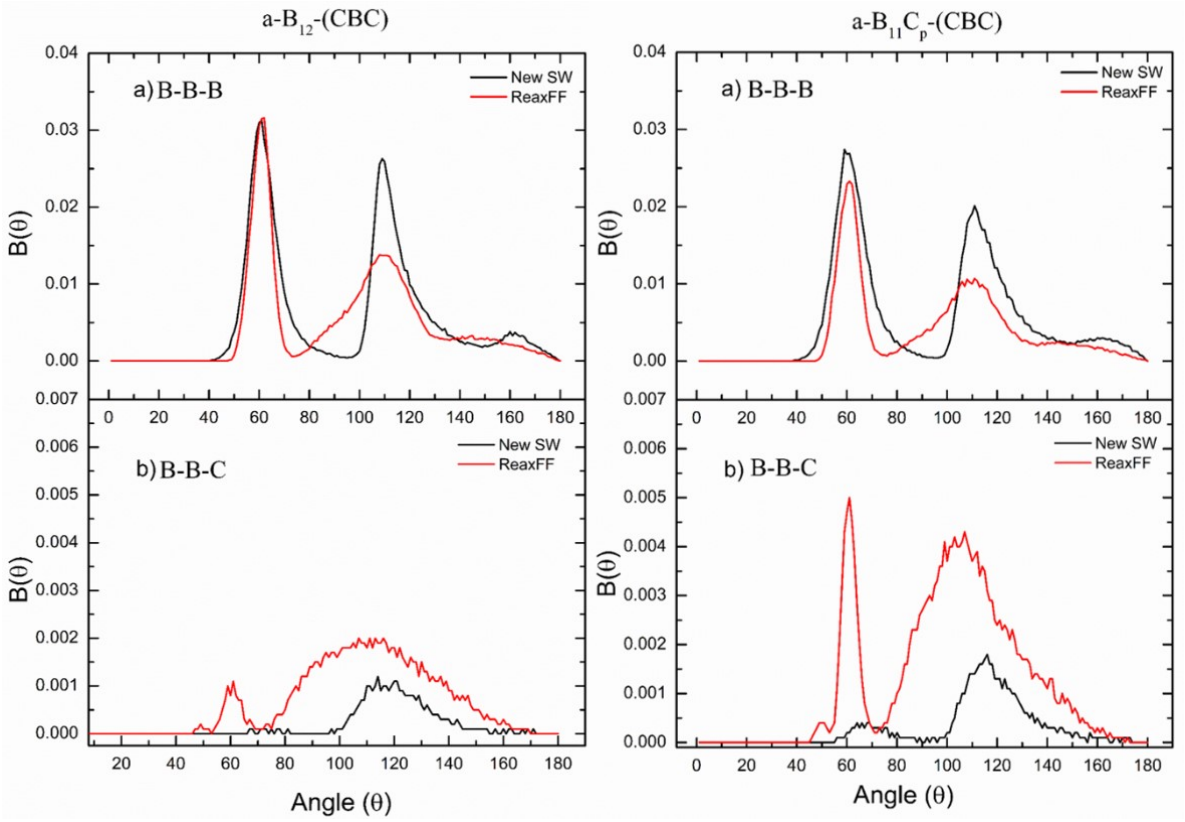

Figure 18. B-B-B and B-B-C angular type comparison between New SW and ReaxFF generated a-B_{12}-(CBC) and a-$B_{11}C_p$-(CBC) amorphous models.

The bond angle distributions which are shown in Figure 17 and Figure 18 produce relatively narrow and distinct peaks for New SW potential at ~ 110^{o} whereas diffused peaks exist for the ReaxFF models which necessarily means more distorted icosahedrons are present in the amorphous sample prepared using ReaxFF. This prominent peak is due to the constraint in SW potential formulation where there is only one choice of the angular cutoff for three-body interaction which we choose to be a regular tetrahedral angle for B-B interaction. The same observation can be made in B-B-C angular type as well in Figure 17 and Figure 18. ReaxFF sample has ~ 9.5 % of the B-B-C angle which is ~ 4.7 % more than the New SW prepared sample. Since the B-B-C angle results from the bonding between the CCC carbon chain and the icosahedra, this could be the reason behind the densified sample coming out of ReaxFF simulated amorphous models. Carbon atom bonding with icosahedral B_{12} is shown in Figure 19 for ReaxFF potential.

The B-B-C angle is much more prominent in the ReaxFF models of a-B_{12}-(CBC) and a-$B_{11}C_p$-(CBC) which can be attributed to more connectivity in the amorphous model helping in densifying the structure as seen from Table 8. The reason both a-B_{12}-(CBC) and a-$B_{11}C_p$-(CBC) are denser than a-B_{12}-(CCC) is that the C-atom in the edge of CBC chain can make three covalent bonds compared to only two in CCC chain. The increased affinity of C-atom in the CBC chain is responsible for an increased percentage of B-B-C angle due to their connectivity resulting in the denser structure. The consistently lower presence of B-B-C and C-B-B three-body angle in all the New SW generated model compared to the ReaxFF model could be the result of two body BC SW parameter. These two-body BC SW parameters were the results of parameter mixing rule and taken directly from Dugan et al. [46] other than the σ parameter which

affects the bond length and as seen from Table 7. The BC bond length due to New SW is very close to DFT and ReaxFF.

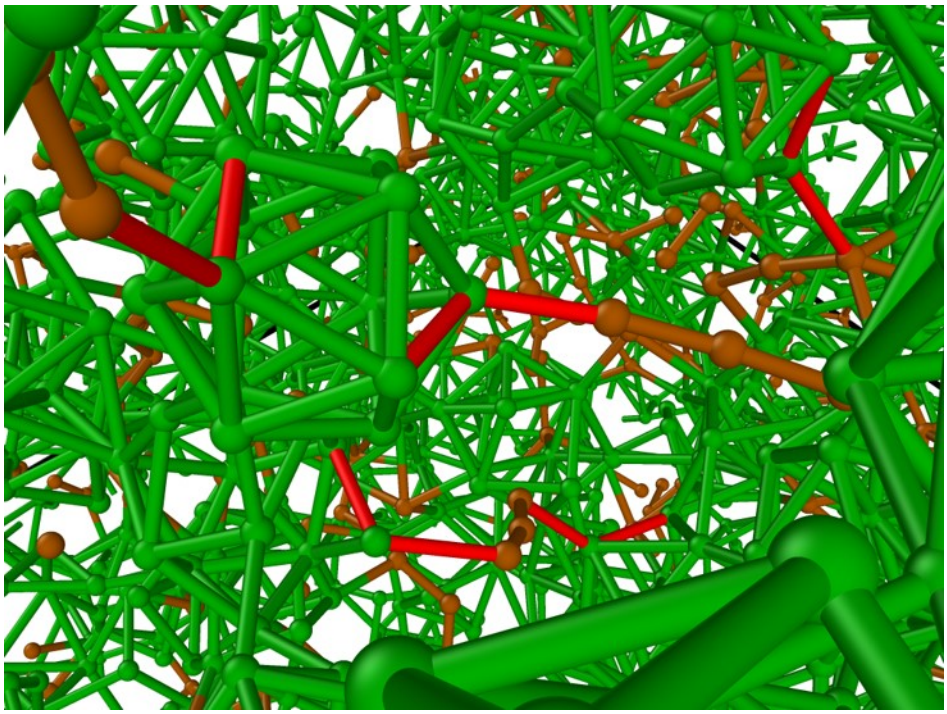

Figure 19. B-B-C angle in the ReaxFF made a-B_{12}-(CCC) model. Green atoms and bonds are the boron and brown atom and bonds are carbon. The red bond shows C atom bonding with B_{12} icosahedron's forming B-B-C angle.

Radial Distribution Function. Radial distribution function *g(r)* provides information on the short-range order of the material structure under study. Figure 20 shows g(r) of a-B_{12}-(CCC) using New SW and ReaxFF potential. The sharp first peaks at ~ 1.8 Å on both the models as seen in Figure 20 (a) and (b) is due to B-B pair with only minor difference noted in Figure 20 (c). This suggests the strong short-range order presence in the structure is predominantly due to B-B pairs. The second nearest neighbor peak, largely due to B-B pairs, is found at ~ 2.9 Å for both potentials. The New SW potential generates a sharp distribution while ReaxFF results in broader distribution. This tells us that the second nearest neighbors have a wide distribution of bond

lengths in the ReaxFF model whereas the New SW model has a much more similar bond length giving rise to the sharp peak. Although it looks erroneous at first sight, this signal can be easily explained using the nearest neighbor distances shown in Figure 21.

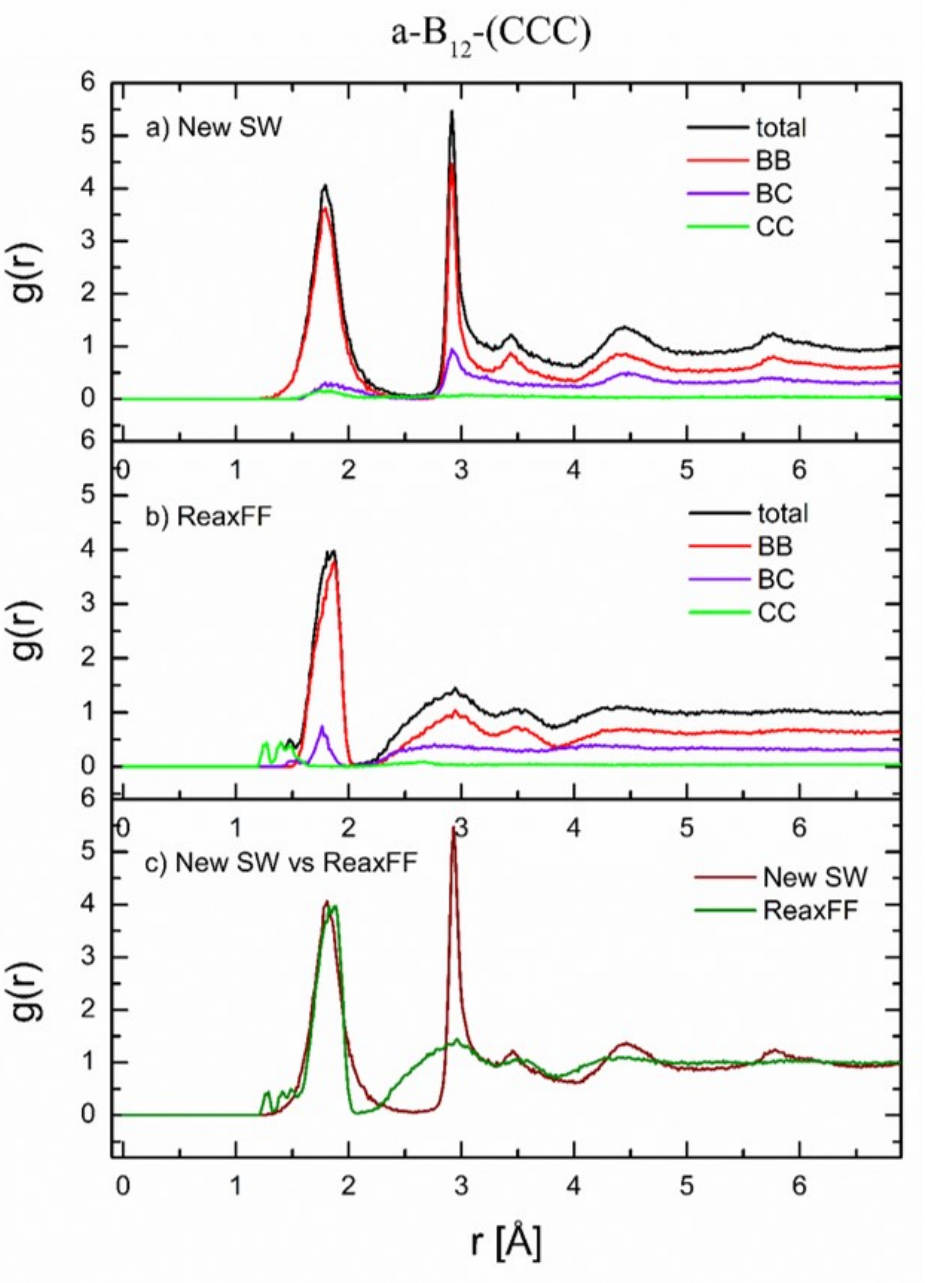

Figure 20. The radial distribution function of a-B_{12}-(CCC) prepared using a) New SW b) ReaxFF and c) comparison between New SW and ReaxFF generated total RDF.

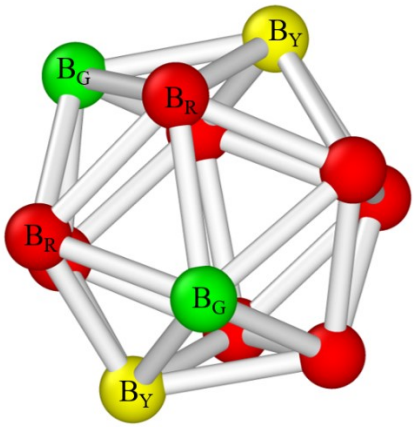

Figure 21. Nearest neighbor distances present in the B_{12} icosahedra. Here red, green and yellow colored boron atoms are used to show the first, second and third nearest neighbor distances respectively present in B_{12} icosahedra. Here, B_R-B_R = 1st neighbor, B_G-B_G = 2st neighbor and B_Y-B_Y = 3rd neighbor.

The first B-B peak icosahedra arise from B_R-B_R type pairs while the second neighbor peak caused by the B_G-B_G pair and the third peak by B_Y-B_Y pairs. The B_G-B_G pair distance is around ~ 2.9 Å within the icosahedra and is responsible for the second peak in the *g(r)* which is present in both models. The root cause for the strong peak for the New SW potential in the *g(r)* seen in Figure 20 (a) and Figure 22 (a) lies in the functional form of SW potential where only one angular cutoff can be applied for one element type. Figure 17 and Figure 18 show the towering peak of the New SW model compared to the ReaxFF model at ~ 110° which comes from the bond angle B_R-B_G-B_G type in Figure 21 resulting in the length of B_G-B_G type to peak at ~ 2.9 Å. As ReaxFF allows a wide variety of B_R-B_G-B_G type angles there is a broad peak for B_G-B_G type neighbors in *g(r)*. The second neighbor peak in New SW generated model is, in fact, an indication of the presence of pentagonal rings coming from icosahedra in the amorphous boron carbide model. Additionally, the B_Y-B_Y lengths are responsible for the tiny shoulder peak at ~3.4 Å which is seen in both Figure 20 (a) and (b). As shown in Figure 20 (a) B-C pairs have first, second and third peaks around B-B position whereas B-C peak in Figure 20 (b) is more

prominent and presents only around ~ 1.75 Å. The prominence of this peak on ReaxFF made a-B_{12}-(CCC) for the B-C pairs is due to the CCC chain atom connecting the icosahedrons which are in agreement with the higher density of ReaxFF model compared to that of New SW model discussed later. The amount of carbon atoms in the amorphous model is 20 % which is reflected as a very low-intensity peak at ~ 1.80 Å in Figure 20 (a) and around ~ 1.4 Å in (b). This mismatch in the C-C position arises because New SW has already been shown to overestimate the C-C bond length in Table 7. C-C pairs form the shoulder peak to the left of the first peak of global *g(r)* in case of ReaxFF model.

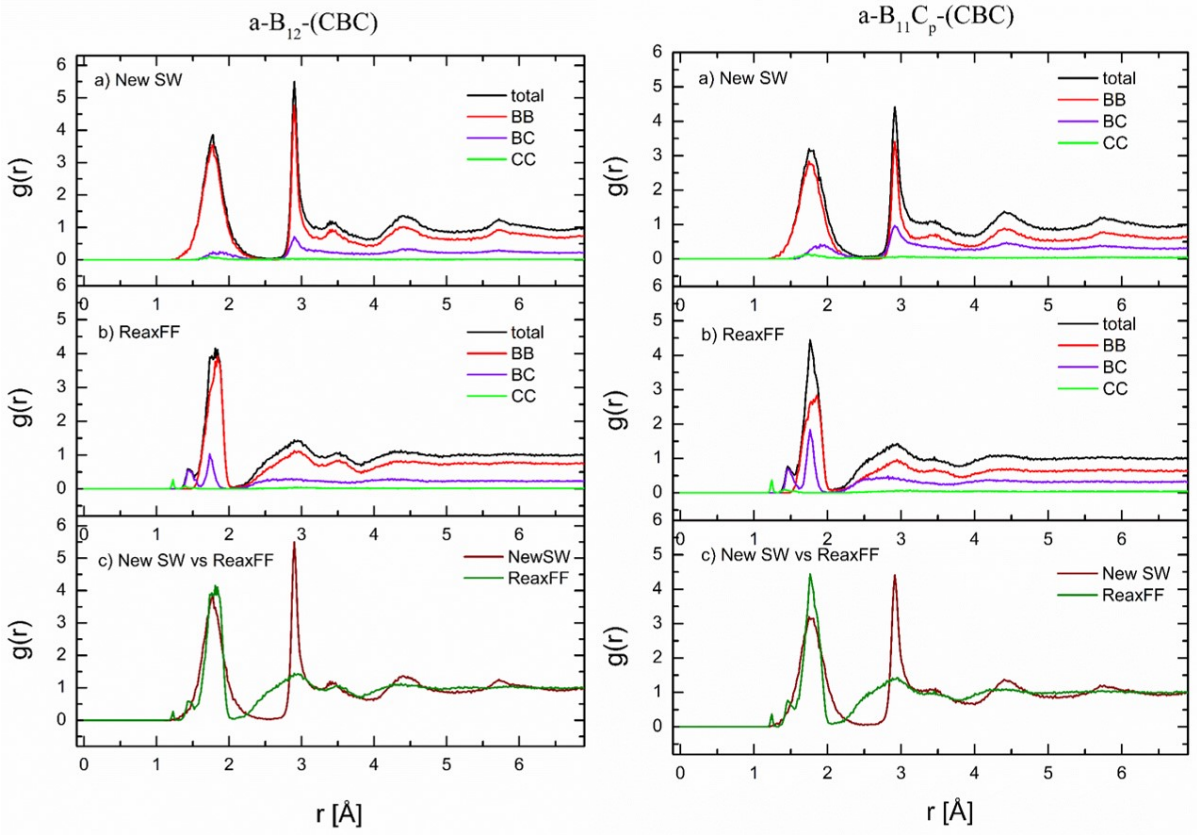

Figure 22. Radial distribution function of a-B_{12}-(CBC) (left) and a-$B_{11}C_p$-(CBC) (right) prepared using a) New SW b) ReaxFF and c) comparison between New SW and ReaxFF generated total RDF.

Figure 22 shows the RDF of two other amorphous model a-B_{12}-(CBC) and a-$B_{11}C_p$-(CBC). All the B-B peaks are located almost around the same position indicating the short-range ordering of icosahedral structure in the amorphous matrix environment. The presence of the B-C pair is more prominent in a-B_{12}-(CBC) and even stronger in a-$B_{11}C_p$-(CBC) model in case of both the potentials. This presence is expected as every chain atom present in the structure has B-C pairs compared to the CCC chain in a-B_{12}-(CCC) where the B-C interaction arises only between icosahedra and chain atoms. However, the B-C peaks are present at ~ 1.45 Å and ~ 1.75 Å compared to only at ~ 1.75 Å in ReaxFF a-B_{12}-(CCC) model. These two peaks arise from different types of B-C bonding environment. The smaller length arises from the B-C bonds in the chain atoms whereas longer bond arises from C in the CBC chain and B in the icosahedra [137] in Figure 22 (b) a-B_{12}-(CBC). But in the case of Figure 22 (b) a-$B_{11}C_p$-(CBC) there is C atom within in icosahedra which adds more types of B-C bonding environment in addition to the present in Figure 22 (b) a-B_{12}-(CBC). The further additions are inter-icosahedral B-C pairs and intra-icosahedral B-C pairs [43] both of which add ~ 1.75 Å type bond length giving rise to the sharp peak even in the global g(r). As seen in Figure 22 (b) both on the left and right C-C pairs peaks at around ~ 1.2 Å due to the bonding between C-atoms from two CBC chains present in the amorphous structure. But C-C pair is in higher amount in Figure 22 (b) a-$B_{11}C_p$-(CBC) compared to Figure 22 (b) a-B_{12}-(CBC) as there is additional bonding between C-atom in $B_{11}C_p$ and CBC chain carbon and intra-icosahedral bonding that connects two $B_{11}C_p$. The simplicity of SW potential formulation couldn't differentiate between the B-C pairs in CBC and B-C pairs between chain carbon and icosahedral boron with a broad and diffused peak at ~ 1.85 Å in Figure 22 (a). Presence of C-C pairs is very minimal in New SW generated model in Figure 22 (a).

Radial distribution function comparison of amorphous boron carbide for all the models shown in Figure 20 and Figure 22 shows the peaks at ~ 1.8 Å, ~ 2.9 Å, and shoulder at ~ 3.4 Å indicating the short-range order interaction strongly representing the icosahedrons. For pristine icosahedra's Larbi et al. [76] mentioned the position of a second and third neighbor at 1.6*d and at 1.9*d respectively with "d" being the edge length in icosahedra. Pallier et al. [5] found a similar result with peaks located at ~ 1.7 Å, ~ 2.9 Å, and ~ 3.4 Å. However, the first global peak is attributed to the B-C pair which is clearly dominated by B-B pair in our results. This arises from the fact that their model has longer chains of B and C atoms outside the icosahedrons whereas our models maintain the B/C stoichiometry with their crystalline counterpart with only short-chained (CCC or CBC) atoms forming the matrix of B and C atoms. The RDF reported by Ivashchenko et al. [40] in their first-principle study of a-120 generated from c-B_4C agrees with our amorphous models. But SRO study of a-B_4C by Bao et al. [137] reported *g(r)* peaks at ~ 1.63 Å and ~ 2.95 Å without the shoulder peak at ~ 3.4 Å. Since the shoulder peak, ~ 3.4 Å is missing which is the indicator of unbroken icosahedra and their first peak shifted to ~ 1.63 Å, more close to B-C bond length 1.57 Å in the amorphous matrix [5], our study suggests the thin films deposited had broken icosahedrons in the BC matrix. The a-B_4C thin film deposited at 600ºC by Zhou et al. reported a series of RDF peaks, namely ~ 1.4 Å originated from C-B-C chain, ~ 1.7 Å from the C-B intra-icosahedral bond length, ~ 2.9 Å from C-C in C-B-C, and a shoulder at ~ 3.5 Å. Our results from Figure 22 agree fairly well with the first two arguments although in our case the peak at 2.9 Å is actually coming from the B-B instead of C-C pair. This is because the carbon concentration is only 20 % which is relatively small to register into a major second nearest neighbor *g(r)* peak. Our study instead suggests that this peak should be attributed to the B-B second nearest neighbor in icosahedron which is also seen in other studies [5,76,137].

Structure Factor. Neutron diffraction static structure factor (*S(Q)*) is a reciprocal space property of materials that are often used to characterize disordered glasses [138–141]. *S(Q)* in reciprocal space is a Fourier transform of *g(r)* in real space which carries short-range, medium-range and nano-order structural information [141]. In Figure 23 we report the total structure factor of a-B_{12}-(CCC) samples and its comparison with the *S(Q)* of Randomly packed B_{12} and DFT structure in the literature within $0.45 \leq Q \leq 21$ Å^{-1}.

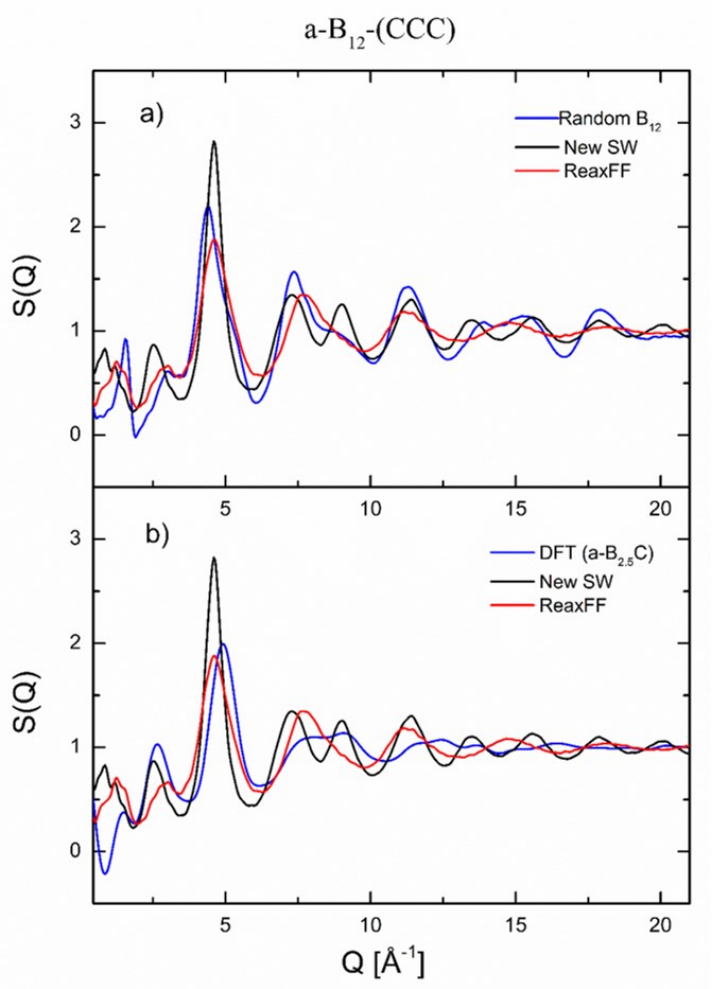

Figure 23. Total structure factor of amorphous boron carbide a-B_{12}-(CCC) prepared using New SW (black line) and ReaxFF (red line) and their comparison with the (a) S(Q) of Random B_{12} (blue line) (b) DFT a-$B_{2.5}$C [142] (blue line).

Icosahedral B_{12} was packed in a simulation box and the structure factor was computed and carries signature peaks containing information of the disordered boron icosahedra. *S(Q)* values below 1 $Å^{-1}$ are not experimentally reliable due to detector resolution and contain unphysical oscillation [123], and are thus excluded from the interpretation. Figure 23 shows the first small intensity peak at ~ 1.5 $Å^{-1}$ in all cases with more intensity for Random B_{12}. The shoulder peak located at ~ 2.6 $Å^{-1}$ is prominent only in New SW and the DFT generated a-$B_{2.5}C$ ($B_{154}C_{62}$) model [5]. The second peak has the highest intensity compared to any other peak in *S(Q)* located at ~ 4.6 $Å^{-1}$ for New SW and ReaxFF models with New SW having a very strong signal. Random B_{12} has a peak shifted to the left at ~ 4.4 $Å^{-1}$ compared to DFT a-$B_{2.5}C$ which has right-shifted peaks at ~ 4.9 $Å^{-1}$. As this second peak is a high-intensity peak present in all the models having random icosahedrons in the amorphous matrix and experimental thin film of boron carbide [5], this can be used as a signature of disordered icosahedrons. The third peak for Random B_{12} is present at ~ 7.2 $Å^{-1}$ with a small shoulder at ~ 9 $Å^{-1}$ but New SW model has two split peaks at both positions while ReaxFF has a peak in between at ~ 7.7 $Å^{-1}$. DFT model a-$B_{2.5}C$ has just a plateau from ~ 6.5 to 10 $Å^{-1}$ but interestingly experimental boron carbide thin film by Pallier et al. [5] has two split peaks in the same position as seen in New SW. Afterward, DFT a-$B_{2.5}C$ peak dampens rapidly followed by the ReaxFF model. Random B_{12} peaks have oscillating peaks that dampen much later than New SW peaks. These oscillating dampening peaks in *S(Q)* are often seen on disordered amorphous glasses [141,143]. Figure 24 includes all the amorphous boron carbon models prepared using New SW and ReaxFF. The features of *S(Q)* of both New SW and ReaxFF model in Figure 24 (b) and (c) are similar and consistent with the explanation of a-B_{12}-(CCC). The *S(Q)* in Figure 24 (b) and (c) suggests the amorphous environment in terms of short-range order are similar to a-B_{12}-(CCC).

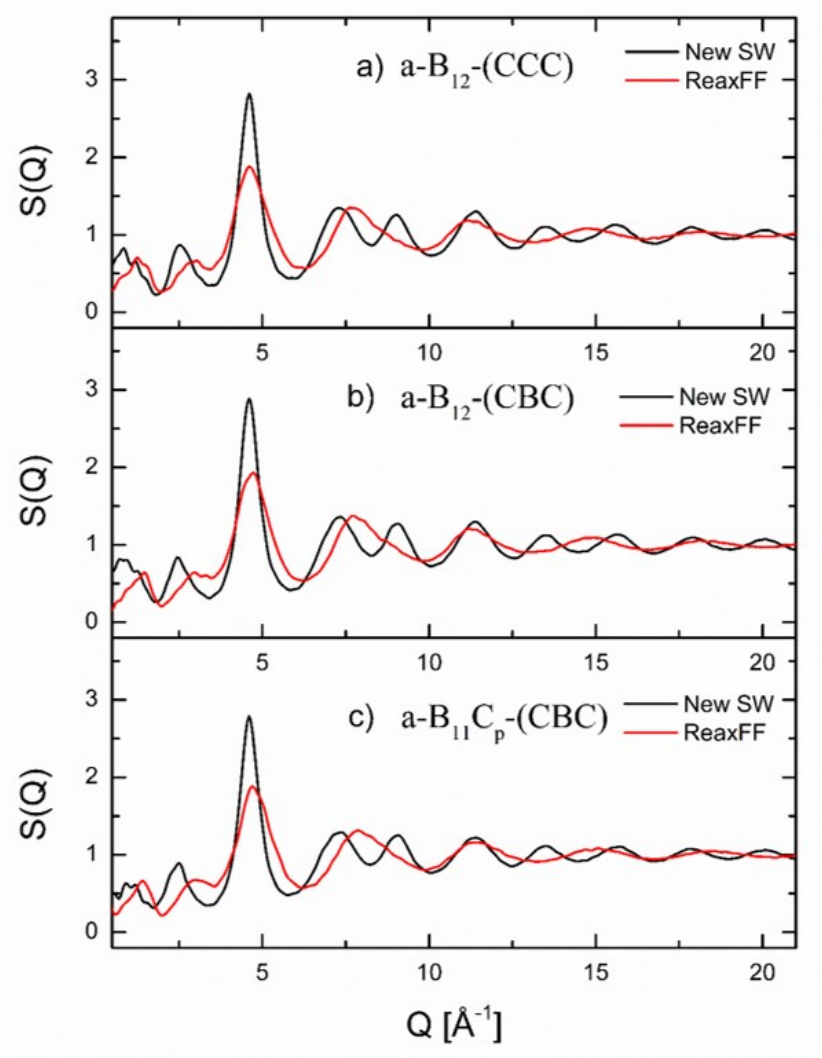

Figure 24. Total structure factor of amorphous boron carbide prepared using New SW (black line) and ReaxFF (red line) (a) a-B_{12}-(CCC) (b) a-B_{12}-(CBC) (c) a-$B_{11}C_p$-(CBC).

Structural Units. The distribution of bonding environments comprised of the first nearest neighbors around a central atom was performed to study the prominence of different types of bonding structural units. As an example, a structural unit is represented as $\underline{B}$-B_5C_2 for the two-element system consists of a central atom B having its first nearest neighbors made up of five B atoms and two C atoms. From Figure 20 and Figure 22 it is clear that the first nearest neighbor for B-atom for ReaxFF and New SW are around the same distance however C-atom has

neighbors at different distances. These structural units are calculated using the cutoffs of 1.88 Å for B-B, 1.72 Å for B-C and 1.45 Å for C-C. The number of structural units fluctuates slightly based on the cutoffs used thus, values below 1 % are ignored. Depending upon the type of crystal structure of boron carbide the presence of B-atom ranges from 80-87 % and C-atom is 17-20 %. The bonding environment of icosahedra can be analyzed mainly by boron centered structural units as shown in Figure 25.

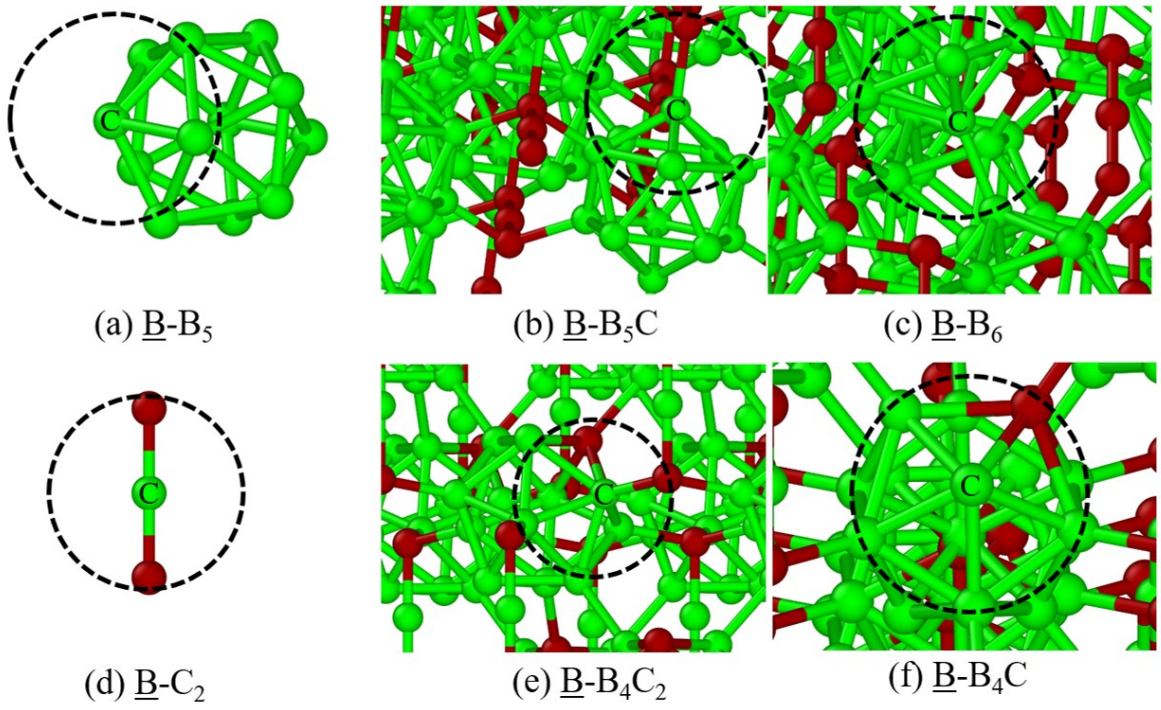

Figure 25. Some of the boron centered local structural environments present in the boron carbide crystal. Here green atoms are boron and brown atoms are carbon. The dotted circle is used to show the first neighbor environment around the boron center marked as C.

In the crystal structure, structural unit B-B_5 is mainly due to the pentagonal cap around the polar boron in icosahedral B_{12}. Similarly, B-B_5C results from the icosahedral boron atom connecting with the carbon atom either via chain or any source and B-B_6 arises from the fact that

icosahedra are connecting each other through boron atoms. B-B_4C and B-B_4C_2 are the environments similar to B-B_5 and B-B_5C respectively except that the C-atom is within the icosahedra. Outside the icosahedra, boron centered environment can be found in the CBC chain in the form of structural unit B-C_2 in the crystal boron carbide.

Figure 26 presents the local structural unit of Boron centered environment in the amorphous boron carbide samples prepared using New SW and ReaxFF potential. The boron centered environments without a carbon connection are slightly more likely in the New SW generated models evident from the B-B_3, B-B_4, B-B_5, B-B_6, B-B_7, and B-B_8 populations. The environment B-B_3 and B-B_4 are the results of distorted or even a few broken icosahedrons. The units B-B_5, B-B_6, B-B_7, and B-B_8 are the results of icosahedral presence and intra-icosahedral bonding through B-atoms. A structural unit containing carbon atoms seen in B-B_3C, B-B_4C and B-B_5C are higher in ReaxFF generated structures. This indicates that the B-C bonding in the ReaxFF models is higher than the New SW which is reflected in their density in Table 8 in the later section. This might be the result of B-C parameters in SW which requires further optimization than the parameter mixing rule.

The results of the Wannier function Center (WFC) calculation of DFT generated a-$B_{2.5}C$ [5] showing the B-B_6 and B-B_5C cluster environments which are also seen in our models in Figure 26. Simeone et al. [144] also attributed these environments in their NMR study of boron carbide. However B-B_4C_2 environment in our model isn't present in the appreciable amount as in a-$B_{2.5}C$. This could be due to the higher presence of C-atoms in their model (B/C= 2.5) compared to ours. Amorphous boron carbide mostly consists of four-fold coordinated boron's (B-B_3C, B-B_4), Penta-coordinated (B-B_4C, B-B_5) and hexacoordinated (B-B_5C, B-B_6) structural units with

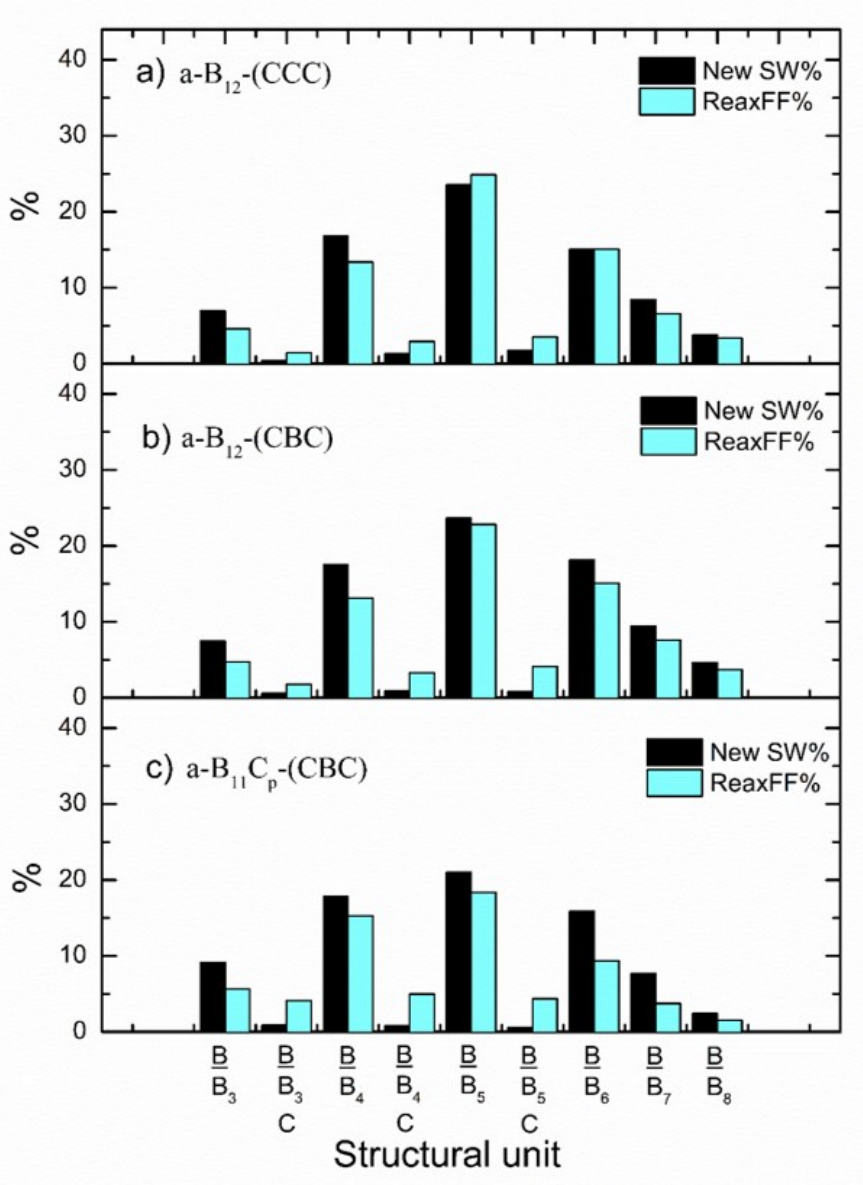

Figure 26. Boron centered prominent local environment present in the amorphous boron carbide models prepared using New SW and ReaxFF potential. (a) a-B_{12}-(CCC) (b) a-B_{12}-(CBC) and (c) a-$B_{11}C_p$-(CBC).

some presence of seven-fold (B-B_7) and eight-fold (B-B_8) coordinated boron centered units seen in Figure 26.The a-$B_{2.5}C$ shows B-environment in the first coordination shell to be highest at six-fold coordination but our models have consistently shown a higher amount of five-fold coordination for both New SW and ReaxFF potentials. The difference in the chemical

environment might be the result of different precursors used to get the amorphous networks as suggested by Ivashchenko [40].

Structure of Amorphous Boron Carbide – HRMC

Bond Angle Distribution. Short-range order present in the structure can be described by studying the nearest neighbor in the first coordination shell, bond length and the angular distribution function as bond angles [145]. The bond angle distribution *B(θ)* comparison between the MD and HRMC models is shown in Figure 27.

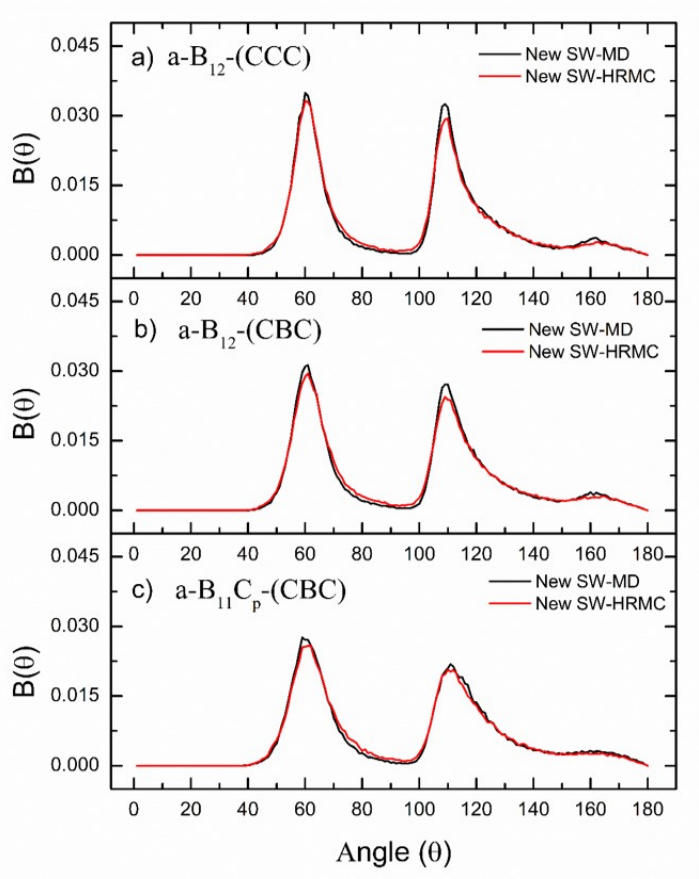

Figure 27. Bond angle distribution comparison between the amorphous models generated by MD and HRMC both using New SW potential. (a) a-B_{12}-(CCC) (b) a-B_{12}-(CBC) (c) a-$B_{11}C_p$-(CBC).

The 3-membered characteristic ring present in the icosahedra is indicated by the bond angle peak at ~ 60° in all the models. The second kind of angle between two boron atoms in the icosahedra is B_R-B_G-B_G type forming between the second nearest neighbor of boron atoms. B_R-B_G-B_G gives rise to the second peak at ~ 110° which is seen in Figure 27. There is a small smooth peak around ~ 160° in the total *B(θ)* seen in all the amorphous models is due to some distorted and fragmented icosahedra. The total bond angle distribution of the HRMC models are very close in agreement with the MD generated amorphous models.

Radial Distribution Function. Figure 28 shows the radial distribution function of the amorphous models from HRMC and their comparison with the parent MD models. HRMC generated models are successful in fitting the *g(r)* peaks for almost all the peak positions. The peak fitting at the positions ~ 1.80 Å, ~ 2.9 Å and ~ 3.4 Å shows icosahedrons are conserved in the HRMC models as in the MD generated models. Signal coming beyond the third nearest neighbor of B-B in the icosahedra is also reproduced and fitted accurately. The peak position at ~ 1.80 Å is mainly attributed to B-B bonding which is less prominent in Figure 28 (c) compared to Figure 28 (a) although the number of boron atoms in both the cases is exactly the same. The reason behind this is the presence of C-atom in the icosahedra forming $B_{11}C$ which keeps the number of B-atom constant but decreases the amount of B-B pair in the structure.

Structure Factor. Static structure factor *S(Q)* fitting between the MD models and HRMC reconstructed structure is shown in Figure 29. Agreement with the MD diffraction data is very good except for the low *Q* region for the MD-*S(Q)*. The unphysical oscillations in the low *Q* region arise from Fast Fourier Transform (FFT) which can be controlled by no. of *Q* values to be fitted in the low *Q* region. The *S(Q)* signal intensity at ~ 4.9 $Å^{-1}$ which is typical of Random B_{12}

is underestimated in HRMC models in all the cases. However, all other secondary oscillating peaks are reproduced well.

Structural Units. The bonding environment is studied using the structural units around the first coordination shell of the central atom. Since boron atoms in our case are mostly present in the forms of the icosahedra boron centered environment, our amorphous models must take these into consideration and such clustering is of central importance. Figure 30 shows the structural unit of boron centered bonding environment comparison between the MD and HRMC generated structures.

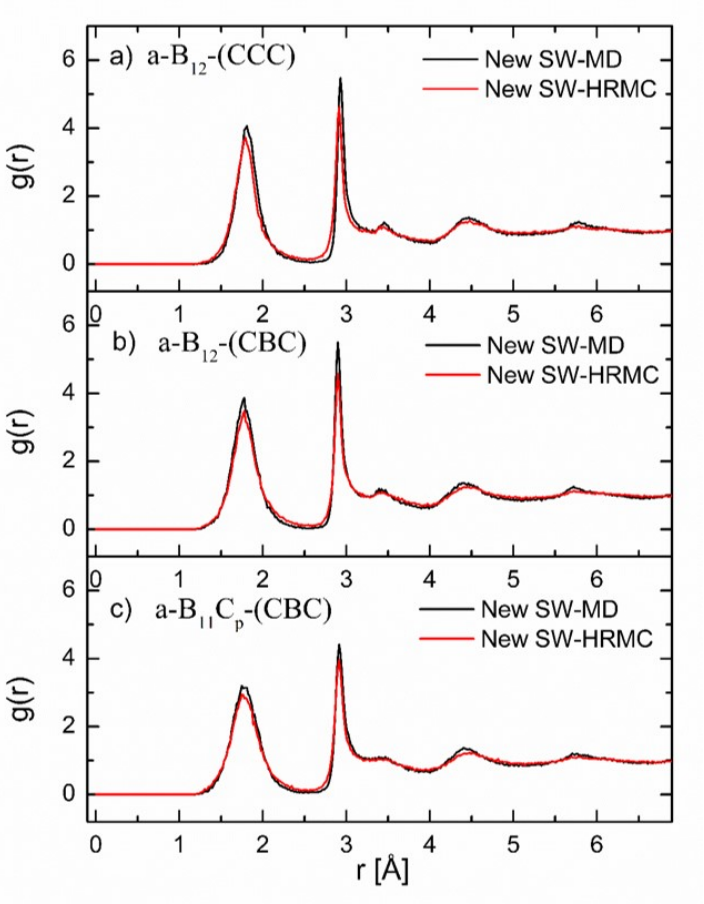

Figure 28. Radial distribution function comparison between the amorphous models generated by MD and HRMC both using New SW potential. (a) a-B_{12}-(CCC) (b) a-B_{12}-(CBC) (c) a-$B_{11}C_p$-(CBC).

The environments B-B_3 and B-B_4 are overestimated by HRMC however the higher coordinated environments like B-B_5, B-B_6, B-B_7, and B-B_8 are slightly underestimated. Carbon present first coordination environments B-B_3C, B-B_4C, and B-B_5C are less than 5 % in the amorphous model which is seen in a similar proportion in the HRMC-generated structures. The coordination histogram is another constraint used to guide the HRMC simulation. Figure 31 shows the coordination distribution of boron atoms in the amorphous boron carbide structures. Boron atoms with four, five and six-fold coordination dominate the structure. HRMC simulation overestimates the three and four-fold coordination whereas higher coordinated boron atoms are underestimated. The five-fold coordination which is a signal of boron in the icosahedra is accurately seen in the HRMC structure compared to MD structures which ensure the stability of icosahedrons.

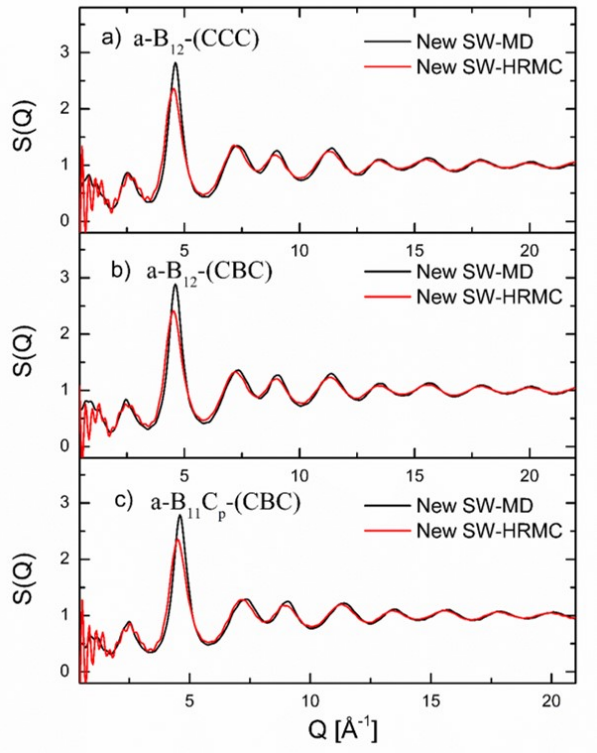

Figure 29. Static structure factor comparison between the amorphous models generated by MD and HRMC both using New SW potential. (a) a-B_{12}-(CCC) (b) a-B_{12}-(CBC) (c) a-$B_{11}C_p$-(CBC).

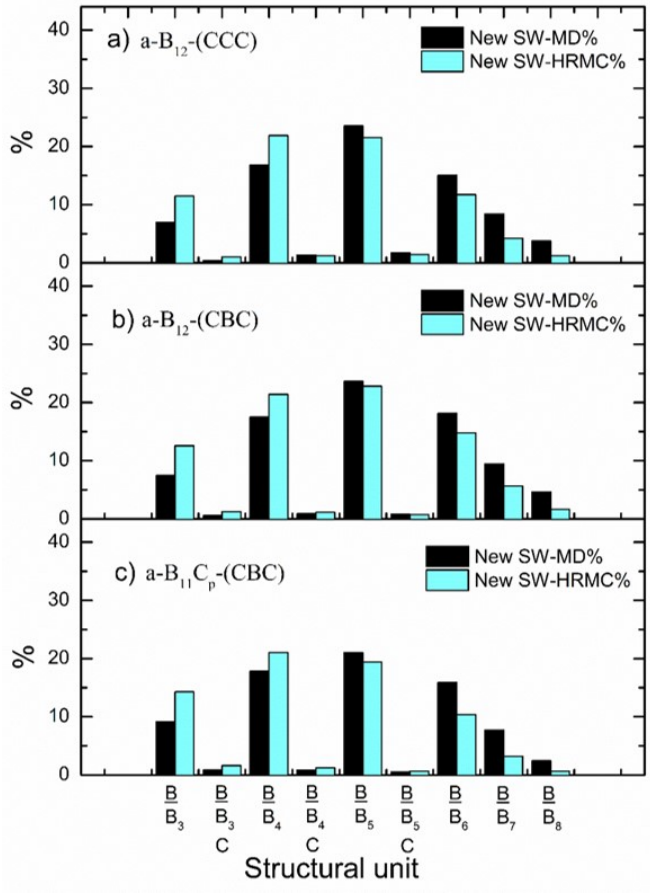

Figure 30. Boron centered prominent local environment present in the amorphous boron carbide models generated using MD and HRMC both using New SW potential (a) a-B_{12}-(CCC) (b) a-B_{12}-(CBC) and (c) a-$B_{11}C_p$-(CBC.

Structure of Amorphous Hydrogenated Boron Carbide-MD

Density. The density of all the a-B_xC:H_y models are presented in Table 2. As can be seen on the Table 2 the density of the models created are as low as 0.97 g/cm^3 corresponding to D11 experimental sample to as high as 2.16 g/cm^3 corresponding to the sample B3 reported by Nordell et al. [18] The models created using the densification scheme detailed in the computational details section are within 2 % of the experimental density and can be seen to match with the experimentally calculated values in Figure 32 (b). It is very important to note that the final structures are free from the residual stress within the models. As in the experimental

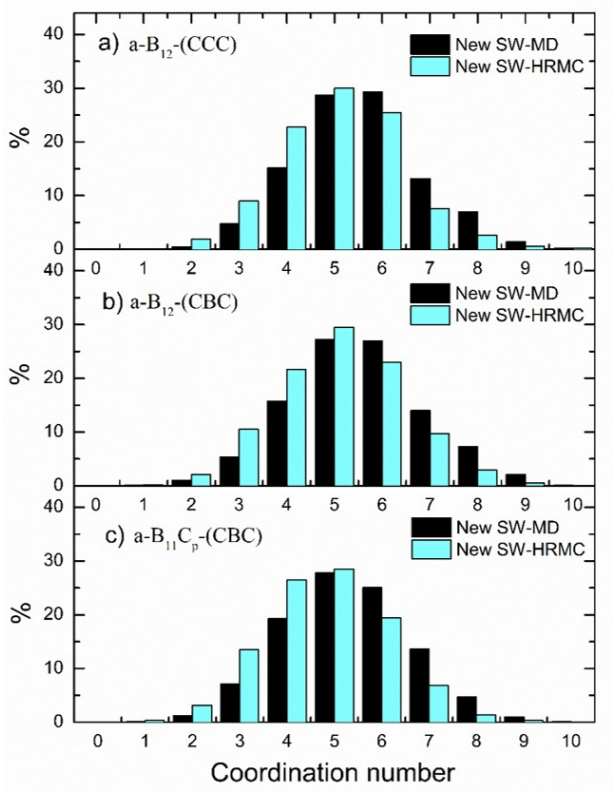

Figure 31. Coordination distributions of Boron atoms in the amorphous models in MD and HRMC. (a) a-B_{12}-(CCC) (b) a-B_{12}-(CBC) (c) a-$B_{11}C_p$-(CBC).

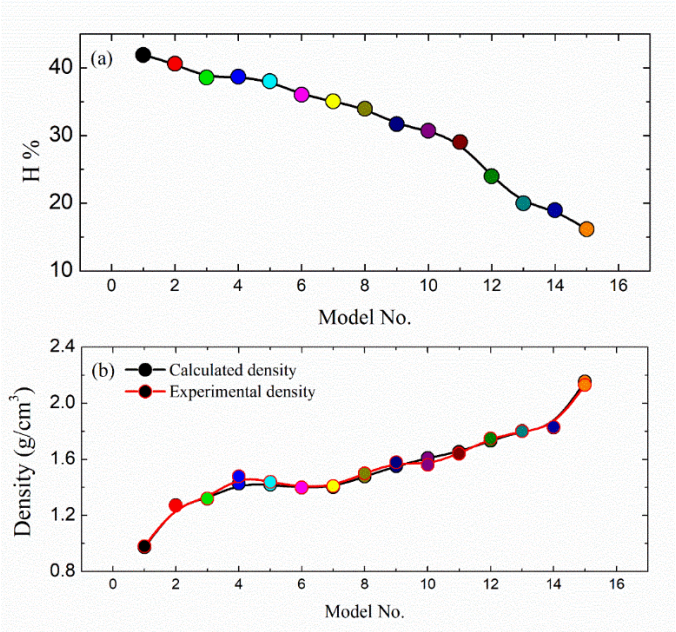

Figure 32. (a) Hydrogen concentration variation on the models of a-B_xC:H_y. (b) Variation of calculated and experimental density.

sample, the density of models has a linear relation with the H % which is shown with the very high linear correlation coefficient of - 0.94 presented in Table 10. With the decreasing H % in the sample the density of the sample goes on increasing as shown in Figure 32 (a) and (b). Model No.'s of the samples are given in Table 2.

The key factor responsible for a given density of any structure is the atomic bonding present within. Figure 33 shows the no. of B-B, B-C, C-C, C-H and H-H bonds that are present in the final a-B_xC:H_y models.

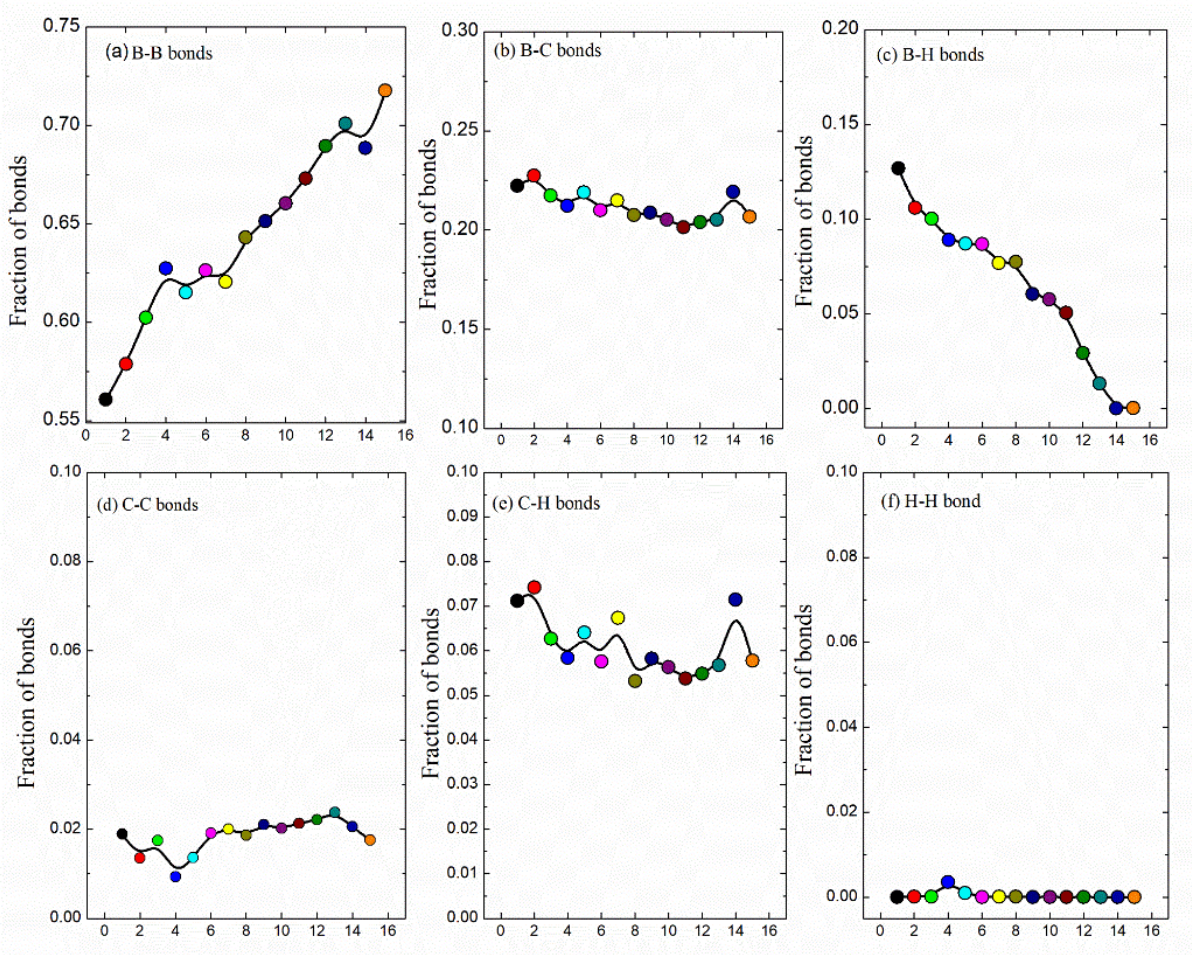

Figure 33. No. of boron, carbon, hydrogen bonds present in the a-B_xC:H_y models.

It is clear from Figure 33 (a) that with the increasing density of the models B-B bond count is increasing linearly whereas B-H bonding goes on decreasing linearly as illustrated in Figure 33 (c). The degree of dependence of B-B and B-H with H% and density can be seen on the correlation coefficients presented in Table 10.

Table 10. The linear correlation coefficient of structural characteristics of a-B_xC:H_y models with their stoichiometry, simulation parameter, and density. All the correlation coefficient higher than 0.8 are highlighted in the table.

Structural	Stoichiometry			Simulation Parameter	Bulk Property
Characteristics	H%	B/C	H/Icosahedra	Applied pressure (Gpa)	Density (g/cm^3)
H%	-	0.00	**1.00**	0.58	**-0.94**
H/Icosahedra	**1.00**	0.00	**-**	0.62	**-0.93**
B-B bond count	**-0.95**	0.00	**-0.94**	-0.46	**0.96**
B-C bond count	0.55	-0.74	0.52	0.00	-0.60
B-H bond count	**0.99**	0.00	**0.99**	0.52	**-0.96**
C-C bond count	-0.56	0.00	-0.58	**-0.96**	0.00
C-H bond count	0.00	**-0.91**	0.00	0.00	-0.45
B-B-B %	**-0.93**	0.00	**-0.92**	-0.39	**0.97**
B-B-C %	-0.64	-0.70	-0.67	-0.37	0.52
B-B-H %	**0.98**	0.00	**0.98**	0.51	**-0.96**
B-C-C %	0.53	-0.71	0.51	0.00	-0.57
B-C-H %	**0.94**	0.00	**0.94**	0.41	**-0.96**
C-B-B %	**0.93**	0.00	**0.93**	0.67	**-0.87**
C-B-C %	0.00	0.00	0.00	**-0.90**	0.00
C-B-H %	**0.82**	-0.47	**0.81**	0.50	**-0.84**
C-C-H %	0.00	0.00	0.00	**-0.88**	0.00
C-H-H %	0.00	**-0.88**	0.00	0.00	-0.48

This clarifies the fact that it is the B-B bonding between deprotonated B-atoms within the icosahedra's are responsible for densification as they are negatively correlated with H/Icosahedra in the structures. We can verify that B-B bonding is, in fact, the *inter*-icosahedral bonding as the initial no. of B-B bonds in all the structure except for Model-B6 has 640 units of icosahedra. Although, C-atom from CH_2 can act as a bridge to form -B-CH_2-B- connection between two dehydrogenated *ortho*-carborane's to aid in the densification process, its overall contribution to the densification of the film is less compared to that of the B-B bonding. The no. of B-C, C-C, and C-H bonds fluctuate very little and are found to be almost constant throughout all the models. The C-C bond count seems to have - 0.96 correlation with the applied pressure. The applied pressure in the structure might have deformed the structure resulting in the increased bond length between them which appears as the decreasing C-C count. The C-H count increases in the structure with the decreasing B/C ratio as addition of CH_2 linkers decreases the B/C ratio. The primary source of B-C, C-C, and C-H bonds are the dehydrogenated *ortho*-carborane. A small no. of C-H and C-C also arises from the *extra*-icosahedral CH_2 hydrocarbon group. There was no H-H bond formation in the models during the densification process as shown in Figure 33 (f).

The H % in the structure correlates very well with the density of the film as mentioned earlier. So, it is important to know the site-specific H-atoms removal that is responsible for aiding for densification. The source of H % in the structure is from CH_2 linkers outside the icosahedra as well as from the H-atoms attached to the icosahedra's. The B-H bonds continue to decrease sharply with decreasing H % in the structure whereas C-H bonds stumble around a constant value. It is clear that the deprotonation of B-atoms from *ortho*-carborane is responsible for densification allowing more B-B bond formation in between the icosahedra's.

Bond Angle Distribution. For the three-element system, there are 18 different possible combinations of the bond angles that can be present in the structure. In our system there were B, C and H atoms so, there were six combinations for each of the atom as a center. They are B-B-B, B-B-C, B-B-H, B-C-C, B-C-H, B-H-H, C-B-B, C-B-C, C-B-H, C-C-C, C-C-H, C-H-H, H-B-B, H-B-C, H-B-H, H-C-C, H-C-H, and H-H-H where the first element is the central atom surrounded by two other atoms forming the angle.

When scanned for all the bond angle distribution we found that the *B(θ)* associated with the H-B-B, H-B-C, H-B-H, H-C-C, H-C-H, and H-H-H were absent in all the samples. This can be explained by the fact that hydrogen atoms can only form single bonding with the other atoms. Also, there was no presence of the B-H-H and C-C-C bond angles present in the structures. The absence of B-H-H is the indicator of no *extra*-icosahedral B-atoms. The B-H-H angle arises if there are fragmented species of *ortho*-carborane forming B_xH_y groups. The icosahedral B-atoms only has one radially outpointing H-atom attached to it. So, the dehydrogenated *ortho*-carborane has maintained the icosahedral geometry during the simulation thus without fragmenting the icosahedral symmetry although deformation of the structure is possible during the densification process. Among the remaining 10 bond angles B-B-B is present in the highest amount ranging from 50-69 % from Model-D11 to Model-B3 and C-H-H is present in the lowest amount of less than 0.5 % which results only due to the CH_2 linkers added into the structure since the icosahedral C-atoms has only one H-atoms bonded to each carbon atoms.

Figure 34 shows the percentage of partial bond angle distribution present in all the models ranging from Model-D11 to Model-B3. These models are arranged in the order of decreasing H % and increasing density. It is clear from Figure 34 (a) that with the increasing density the percentage of B-B-B angle goes on increasing whereas the angles B-B-H, B-C-H, C-

B-B, and C-B-H goes on decreasing linearly. The B-B-B % positive correlation of 0.97 with the density whereas B-B-H, B-C-H, C-B-B, and C-B-H have a negative correlation as mentioned in Table 10. This observation is also consistent with the bond counts of B-B and B-H earlier in Figure 33. This is indicative of the fact that the B-B-B angle is increasing with the increasing density. The other partial bond angle distributions B-B-C and B-C-C don't show clear trend when plotted as the function of decreasing H % as their degree of correlation with H %, B/C, applied pressure and density are only moderate. For carbon-centered C-B-C and C-C-H Table 10 reveals the high degree negative correlation with the applied pressure. As in the case of C-H

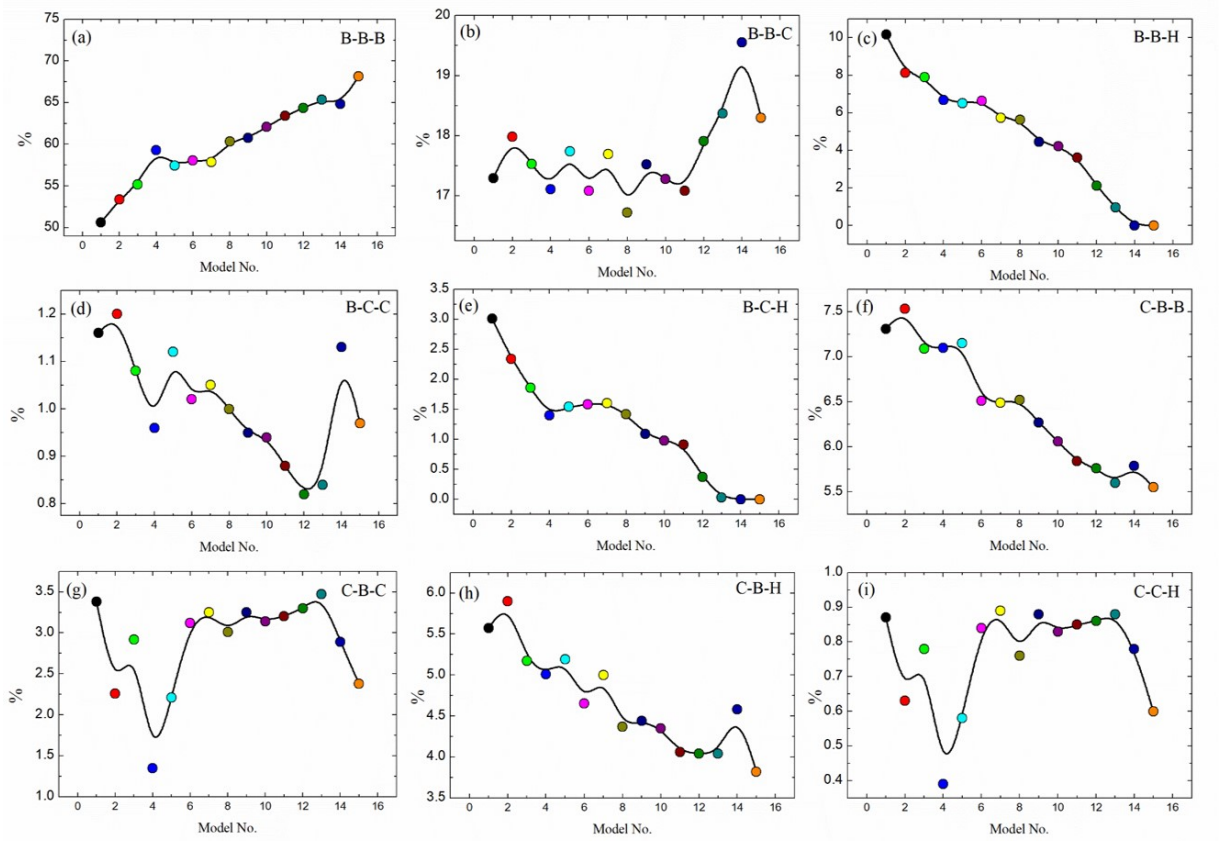

Figure 34. Percentage of the partial bond angle distribution present in the different models of a-B_xC:H_y ranging from Model-D11 to Model-B3.

bond count C-H-H angle is negatively correlated with B/C stoichiometry. The B/C stoichiometry can be used as a measure to predict the amount of CH_2 in the experimental samples.

Figure 35 shows the bond angle distribution of all the models. As can be seen from the figure the total bond angle distribution for all of them is centered on the two characteristics angles at ~ 60^o and ~ 110^o. These two angle are the characteristics of the icosahedral geometry although not only particular of the icosahedral structure. Also, there is a shoulder peak at around ~ 90^o. Table 11 provides the linear correlation coefficient relation of the total and the partial bond angle distribution peaks with the model's stoichiometry, applied pressure and density. From the observation from Table 11 the total bond angle distribution is not seen to have any correlation with stoichiometry or the density of the models. However, with the applied pressure the intensity peaks seem to dampen as they have negative correlations with the intensity peaks. The total bond angle isn't a good indicator to signal the H-content or the density of the structure.

The majority of the total bond angle distribution comes for the B-B-B type angle as seen in Figure 34 (a) and also can be seen in Figure 36. The global peak of ~ 60^o and ~ 110^o comes from the B-B-B type angular distribution in all the models. The peak at ~ 60^o has very small change based upon the intensity however the peak at ~ 110^o is broadening. The intensity peaks in both places vary differently as indicated by their correlation coefficients. Both the peaks are seen to increase with increasing density but the peak at ~ 60^o is independent of the applied pressure. However, the intensity at ~ 110^o is seen to vary strongly with increasing pressure. This could be the result of the more deformation of the icosahedral structure with the applied pressure.

Figure 37 shows the B-B-C bond angle distribution which has a shoulder peak at ~ 50^o and major peaks at ~ 60^o and ~ 110^o. The source of this angular type comes from the carbon atom present in the *ortho*-carborane molecular structure and also from the deprotonated boron

atom bonding with the *extra*-icosahedral carbon atom. The C-atom already on the *ortho*-carborane molecule gives rise to both the peaks however the C-atom outside bonding with the icosahedral bonding can only result in the higher angular type. It is visibly noticeable that around ~ 60° peak position is shifting toward the right from ~ 58° to ~ 61°. The same observation can be seen in the higher angular region at ~ 110°.

Table 11. The linear correlation coefficient of the bond angle distribution intensity peaks of a-B_xC:H_y models with their stoichiometry, simulation parameter, and density. All the correlation coefficient higher than 0.5 are highlighted in the table.

Peak Intensity of B(θ)	Peak position (degrees)	Stoichiometry		Simulation Parameter	Bulk Property
		H%	B/C	Applied pressure (Gpa)	Density (g/cm^3)
Total	40°-70°	0.00	0.00	**-0.73**	0.00
	80°-120°	0.00	0.00	**-0.80**	0.00
B-B-B	40°-70°	**-0.66**	0.46	0.00	**0.66**
	80°-120°	**-0.74**	0.00	**0.84**	0.52
B-B-C	40°-70°	0.00	0.00	0.42	**-0.58**
	80°-120°	0.00	**-0.51**	**0.66**	0.00
B-B-H	100°-160°	**0.92**	0.00	0.00	**-0.97**
B-C-C	40°-70°	0.00	0.00	**0.84**	0.00
	80°-120°	0.00	0.00	0.39	0.37
B-C-H	80°-140°	**0.91**	0.00	0.00	**-0.95**
C-B-B	50°-70°	0.00	-0.45	0.00	**-0.58**
	70°-100°	**0.79**	0.00	**0.88**	**-0.63**
	100°-130°	0.00	0.00	0.50	**-0.56**
C-B-C	50°-70°	0.00	0.00	**0.73**	0.00
	90°-130°	0.00	0.00	**0.86**	0.00
C-B-H	80°-140°	**0.54**	-0.41	0.00	**-0.77**
C-C-H	100°-120°	0.00	0.00	**0.75**	0.00

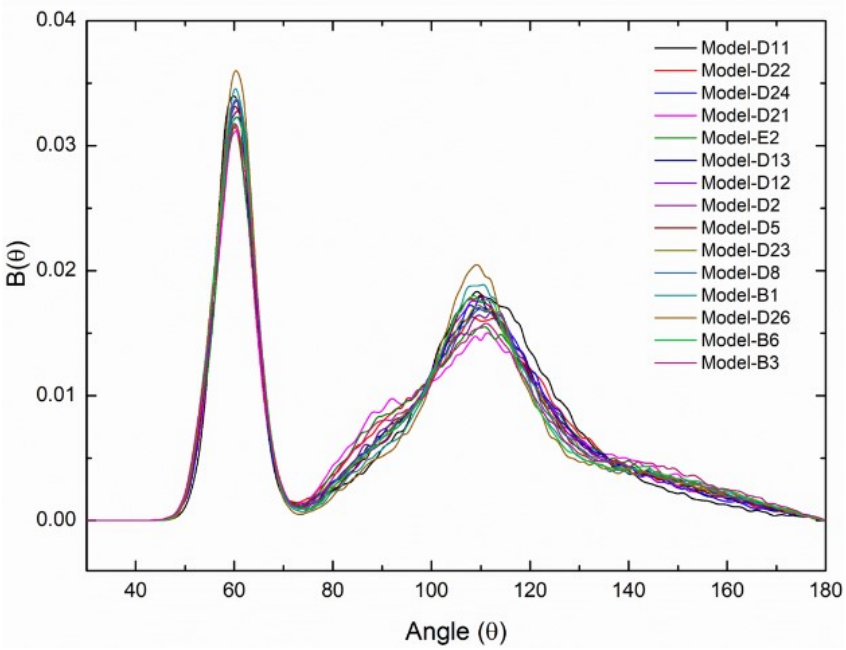

Figure 35. Total bond angle distribution of all the amorphous hydrogenated boron carbide models.

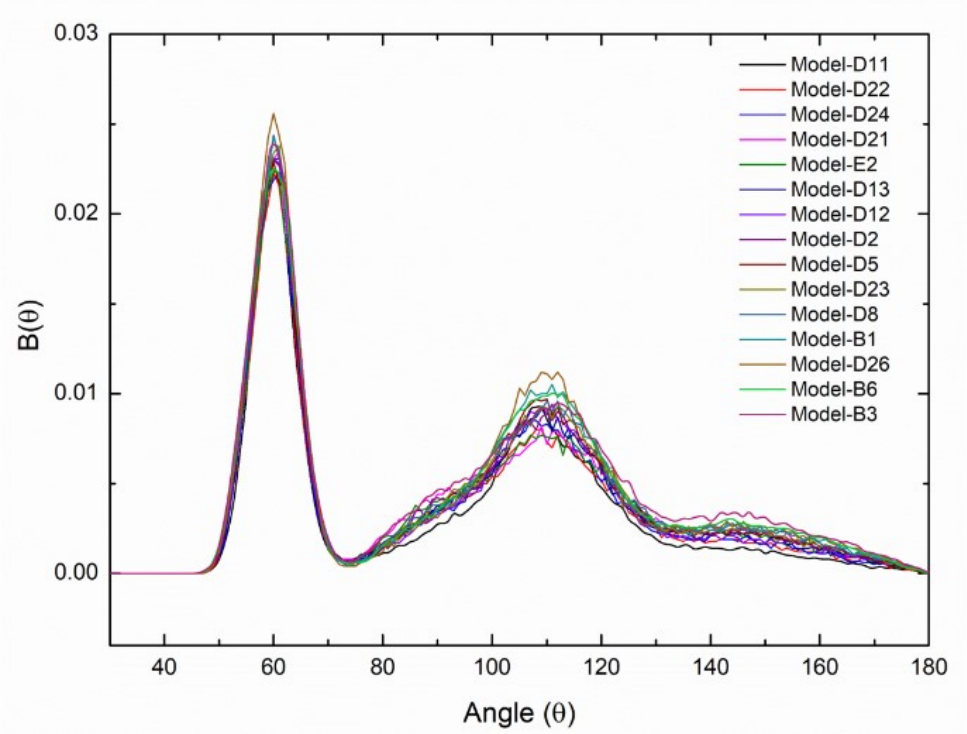

Figure 36. B-B-B bond angle distribution present in the amorphous hydrogenated boron carbide models.

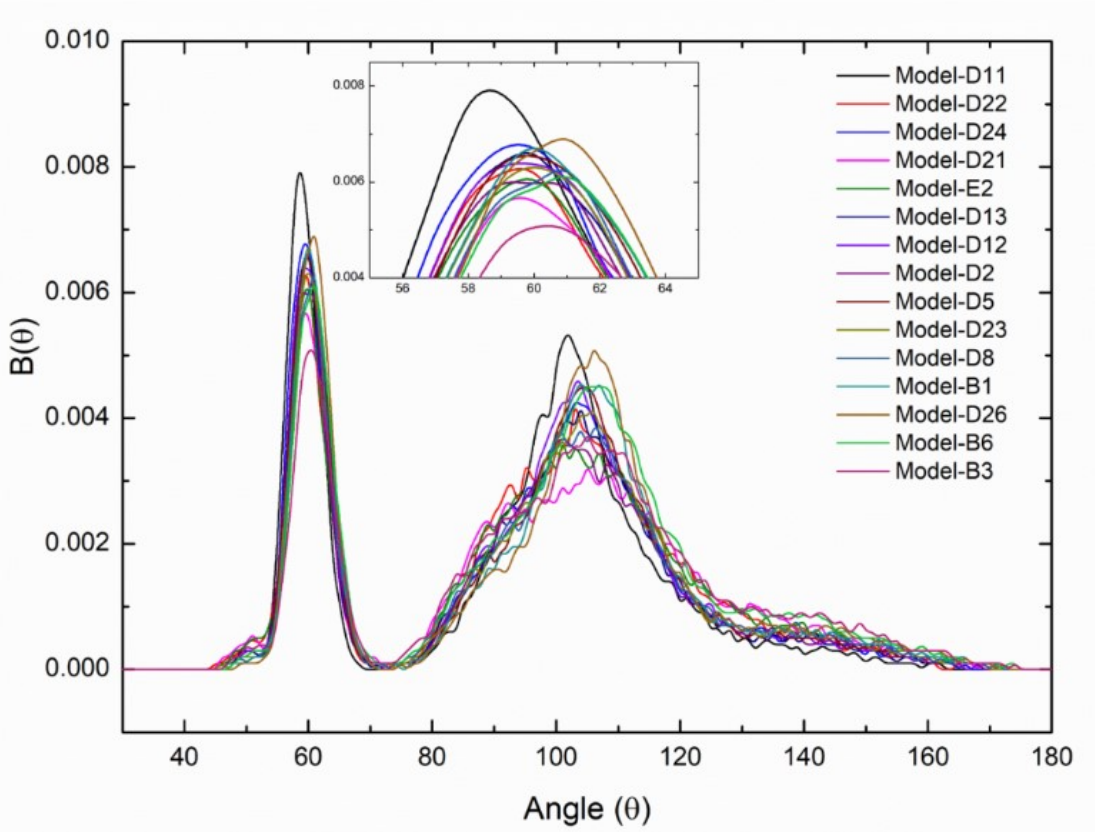

Figure 37. B-B-C bond angle distribution present in the amorphous hydrogenated boron carbide models.

The variation of the peak intensity is moderately correlated only with density at ~ 60°. But the bond angle B-B-C in the higher angular region seen to increase with applied pressure. This is the only angular distribution that is strongly dependent on B/C stoichiometry as seen from Table 11.

B-B-H angular type distribution is shown in Figure 38. In our starting models, there wasn't any *extra*-icosahedral boron's present and the absence of B-H-H type in the final structures would further suggest that boron isn't present outside the icosahedral environment as well. In that case, the only source of B-B-H signal is coming specifically from the icosahedral geometry inherited from the *ortho*-carborane molecule. As seen in Figure 38 the B-B-H angle is distributed around ~ 130°. This is a peculiar signal coming the radially pointing H-atoms in the *ortho*-carborane although in the undistorted *ortho*-carborane it is centered at ~ 120°. The

distortion of this angle could be the result of the densification. Also, there seems to be a peak of very low intensity at around ~ 80^{o} although statistically very lower in amount. The intensity of B-B-H is seen to decrease with the decrease of the H % in the samples. This is the result of the deprotonation of boron atoms of the *ortho*-carborane molecule done randomly in our starting structure which simulates the effect of deprotonation due to the argon bombardment on the *ortho*-carborane molecule. So, as the high energy argon impacts the *ortho*-carborane this distribution can tell us about the deprotonation of the boron atoms within the *ortho*-carborane. The B-B-H is only dependent upon H % as far as the stoichiometry and is seen unaffected by other factors. So, based on the experimentally measurable density or the H% this distribution can be well predicted with the linear relationship. The similar, effect was seen previously with the B-H bond count as well.

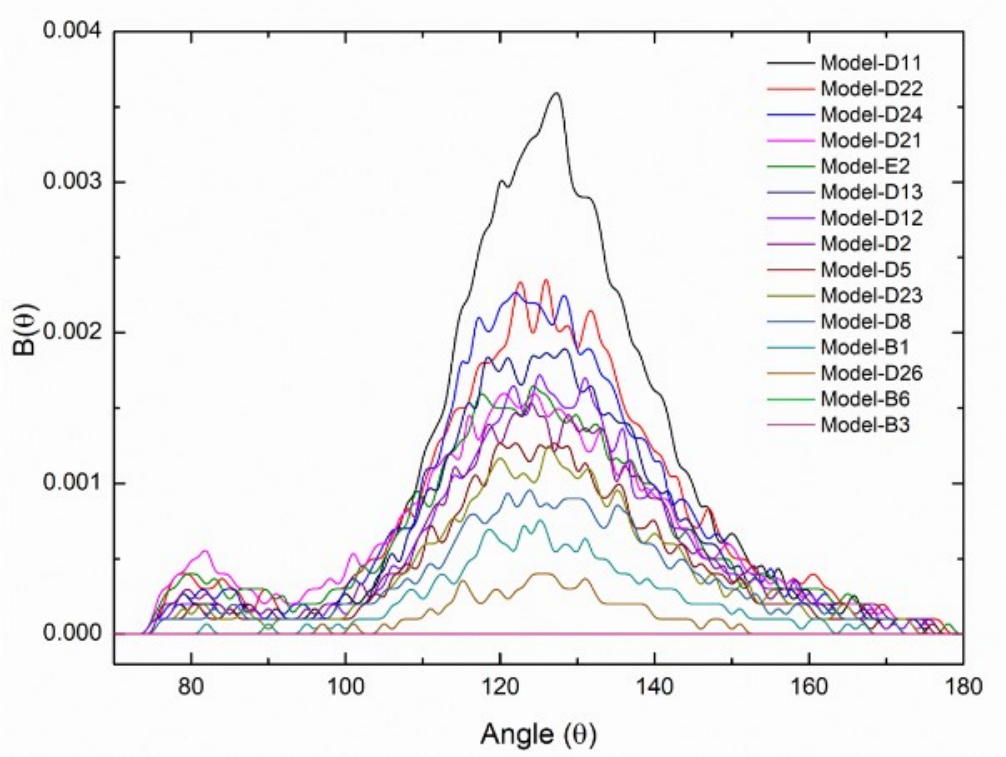

Figure 38. B-B-H bond angle distribution present in the amorphous hydrogenated boron carbide models.

B-C-C bond angular distribution is shown in Figure 39. It has only around 1 % contribution in the total bond angle distribution for all the models as can be seen from Figure 34 (d). The majority of B-C-C bond angle distribution is centered on ~ 58^{o} and very few at ~ 100^{o}. In an *ortho*-carborane molecule, there are two B sites B_3 and B_5 that form this angular type which forms an equilateral type angle with the two carbon atoms positioned at C_1 and C_2 as shown in Figure 5 (a). So, the primary source of this angular distribution is from within the *ortho*-carborane structure which peaks at ~ 60^{o}. B-C-C can be used to differentiate between the amorphous structures generated from other *closo*-carboranes as seen in Figure 4 since *ortho*-carborane is the only one that possesses these characteristics. It is very unlikely that this signal originates from outside the *ortho*-carborane. The deprotonated B-atoms from icosahedra can form the bond with the *extra*-icosahedral carbon linker CH_2 but can form only the single bond. Also, the B-C-C bond angle seems to be immune to the variation of H %, B/C ratio and density. At ~ 60^{o} strong positive correlation is seen with the simulated pressure.

Figure 40 shows the boron centered angular distribution with carbon and hydrogen atoms around it. Two different kinds of observation can be seen in this distribution. First, the peak intensity goes on decreasing from Model-D11 to Model-B3. Second, the peak position around ~ 115^{o} is also seen to have shifted to the lower angular region. The most possible source of this distribution is the icosahedral boron atoms itself. As can be seen in Figure 5 (a) there are six boron atoms namely B_3, B_5, B_7, B_6, B_{11}, and B_4 which can generate this signal. The atoms B_3 and B_6 can form this angle two-fold with both C_1 and C_2. All of these angles within the *ortho*-carborane is centered on ~ 117^{o} in an *ortho*-carborane molecule. The signal intensity is seen to have decreased over time as we go from Model-D11 to Model-B3. This is the result of randomly removing the H-atoms attached to the boron sites. As H % goes on decreasing within the models

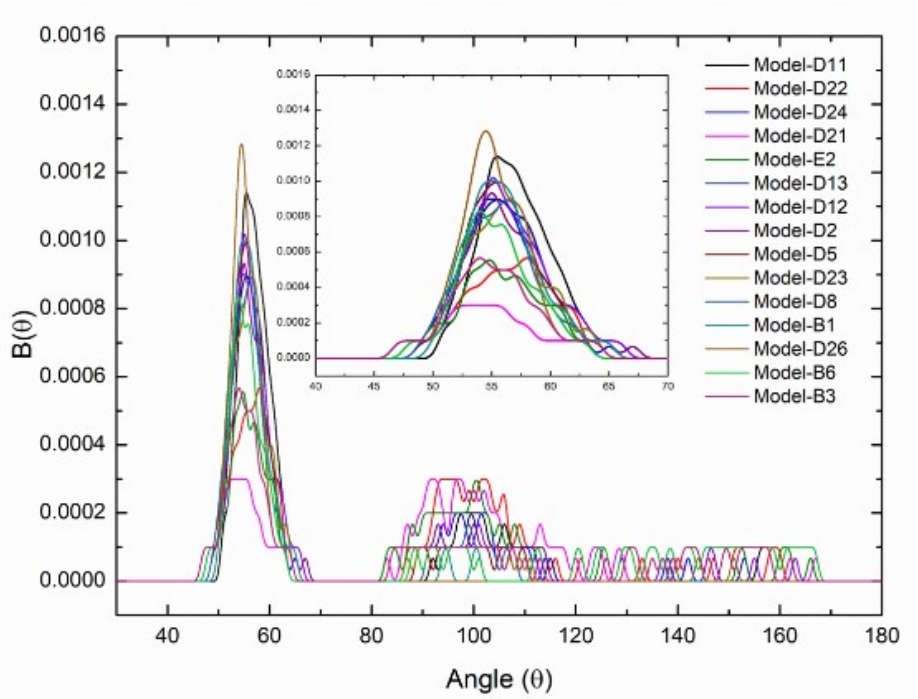

Figure 39. B-C-C bond angle distribution present in the amorphous hydrogenated boron carbide models.

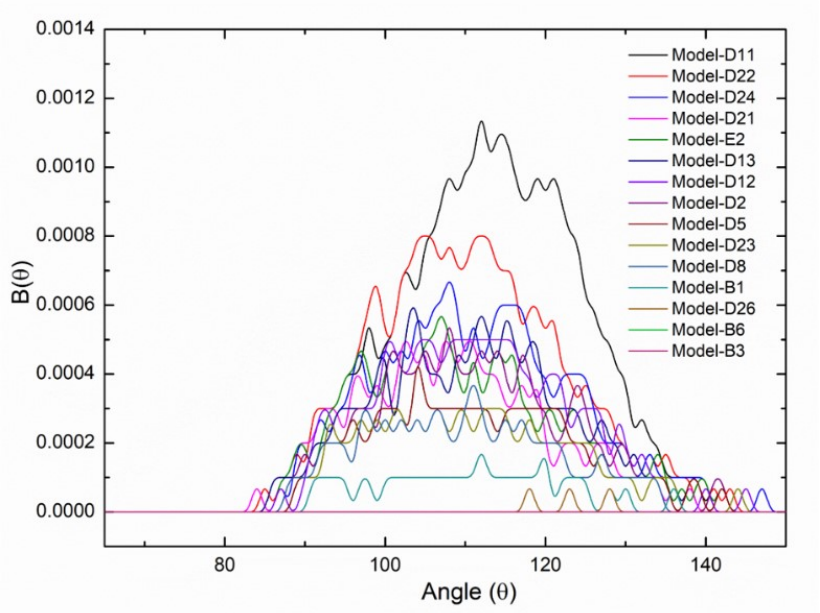

Figure 40. B-C-H bond angle distribution present in the amorphous hydrogenated boron carbide models.

as can be seen from Figure 34 (e) the signal intensity of B-C-H also goes on decreasing. The shift of the peak position could be the result of the densification of the models. The linear regression analysis of the peak intensity provides further verification and insight with the density and H %. B-C-H is strongly correlated with the density and H % as in the case of B-B-H. This angular distribution is the remaining B-atoms bonded with H-atoms within the icosahedra apart from B-B-H. The combination of these two angles gives the dehydrogenation information of icosahedra's however one should be aware of the very low amount of signal coming out of the B-C-H bond angle. The most prominent carbon-centered angular distribution is C-B-B which is present within 5-8 % in the amorphous hydrogenated boron carbide models as can be seen in Figure 34 (f).

The angular distribution for C-B-B is presented in Figure 41. It has three different peaks originating at ~ 60º, ~ 115º, and ~ 85º. Figure 5 (a) shows C_1 and C_2 forming C-B-B bonding with the neighboring boron atoms in an ortho-carborane molecule. There are four cases of C_2-B_6-B_7 type angle giving bond angle peaks at ~ 115º and six cases of C_2-B_6-B_{11} resulting in equilateral type angular distribution. So, for an *ortho*-carborane based structure, the peak intensity of type C-B-B at ~ 60º is higher than ~ 115º. This angular type is independent of H % in the higher and the lower angular region but depends upon the carbon concentration for lower angular region in the structure which is controlled by CH_2 linker and in turn affects the B/C stoichiometric ratio. All the peaks have negative correlation with the density of the sample. The second peak is possible either due to the presence of the CH_2 linker or by the deformation of deprotonated *ortho*-carborane forming the *extra*-icosahedral bonding. The second peak is found to increase in the intensity with the increase of applied pressure in the structure resulting in the

deformation of the icosahedra and also with the increasing H %. The correlation of this second peak with the H % is ambiguous.

The C-B-C bond angle distribution is presented in Figure 42. The origin of this peak is both icosahedral as well as *extra*-icosahedral. Within an *ortho*-carborane structure as in Figure 5, (a) C_2-C_1-B_7 type forms this type of angle at ~ 110^o and C_2-C_1-B_3 forms the angular peak at ~ 60^o. This angular type is also peculiar only to *ortho*-carborane compared to *meta*-carborane and *para*- carborane as there is no CC bonding in their structures. The intensity of peaks at ~ 60^o and ~ 110^o is found to vary based only on the variable pressure applied to densify the structure as seen from Table 11. With higher pressure, the peak intensity decreased and with lower pressure the peak intensity was found to increase. The applied pressure is found to vary based on the H % and B/C stoichiometry controlled by linker's concentration. This angular distribution is statistically small and has no linear correlation with the bulk measurable properties such as H %, B/C stoichiometry and density of the material.

Another prominent carbon-centered bond angle distribution is C-B-H as shown in Figure 43. This bond angle ranges from 4 - 6 % and found to decrease from 5.57 % to 3.82 % from Model-D11 to Model-B3 as shown in Figure 34 (h). The bond angle for C-B-H is found to peak around ~ 115^o. There are three possible sources for this angular environment in the a-B_xC:H_y models. The first source is the icosahedra where C_1 and C_2 carbon within the C_2B_{10} connected to the radially outpointed H-atoms and also the icosahedral boron atoms. The second source would be the CH_2 linker connecting with the deprotonated B-atoms. The third source could be the *inter*-icosahedral bonding resulting due to the distortion and collapse of the deprotonated molecule when variable pressure is applied for the densification. The peak intensity is found to vary with

the H-content and the B/C stoichiometry. The intensity was decreasing with the increasing density in the sample. This correlation can be seen in Table 11.

The bond angle C-C-H is less than 1 % in any of the model of a-B_xC:H_y as shown in Figure 34 (i). The distribution of bond angle for C-C-H centered at ~ 110º as shown in Figure 44. Inside the *ortho*-carborane molecule, C_1-C_2-H and C_2-C_1-H are the only two cases that can create form this angular distribution. It should also be noted that this particular angle is characteristics only of *ortho*-carborane since it results due to CC bonding as in the case of C-C-B bond angle distribution. This particular angle can also result due to bonding between CH_2 linkers outside the icosahedra's. The peak intensity is found to linearly correlate only with the applied pressure on the models with the coefficient value of 0.75.

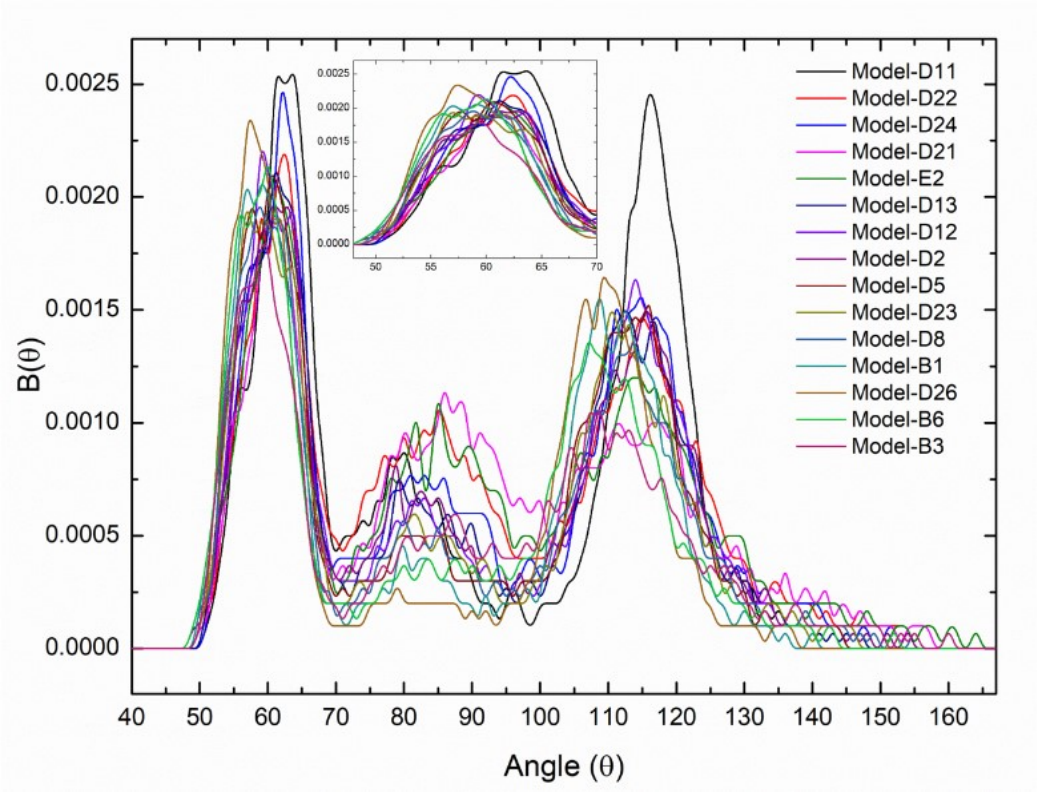

Figure 41. C-B-B bond angle distribution present in the amorphous hydrogenated boron carbide models.

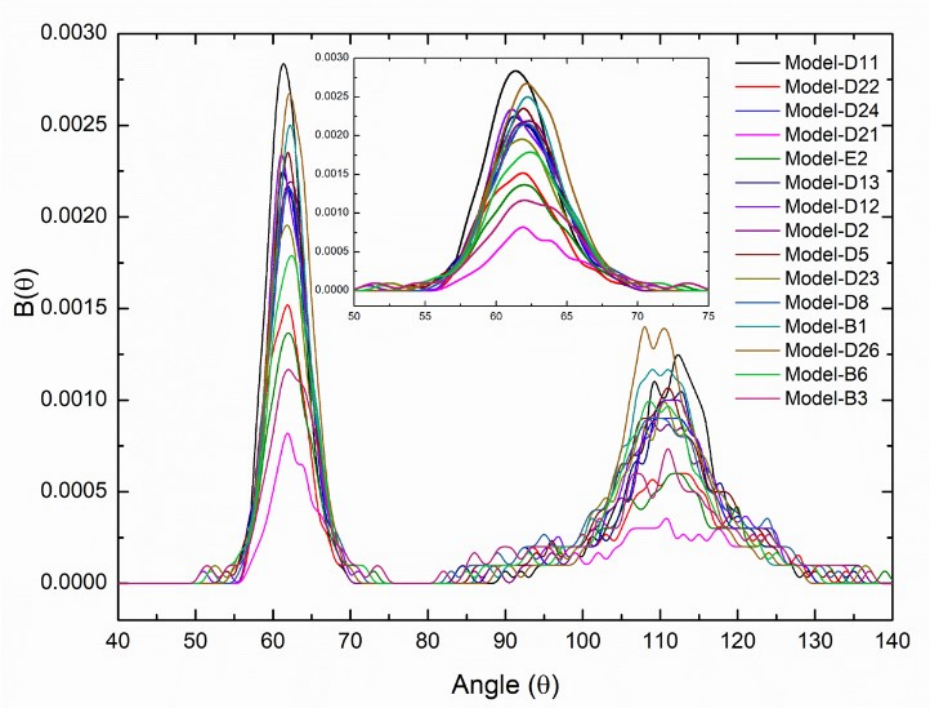

Figure 42. C-B-C bond angle distribution present in the amorphous hydrogenated boron carbide models.

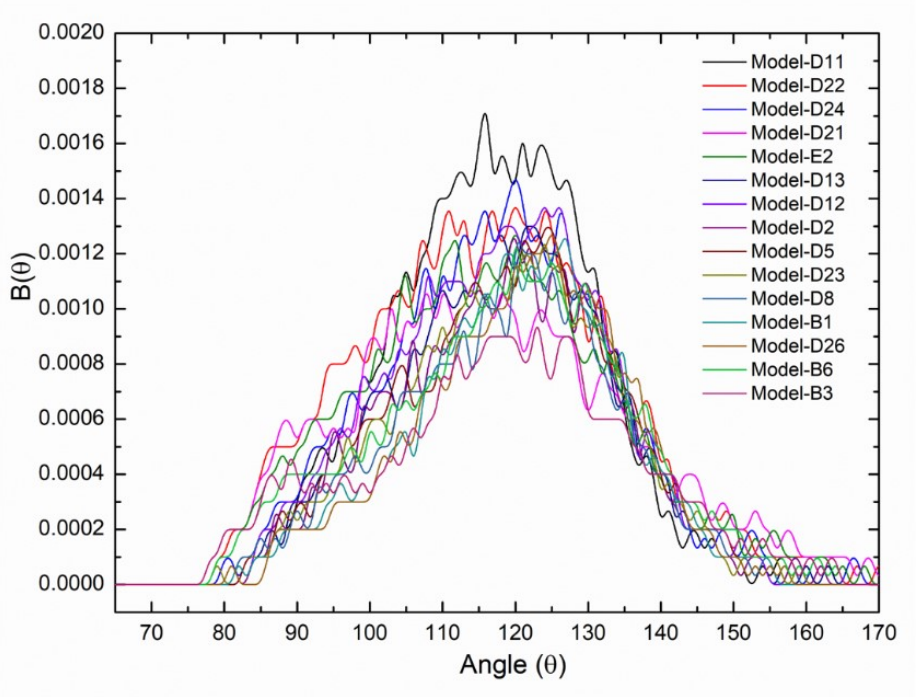

Figure 43. C-B-H bond angle distribution present in the amorphous hydrogenated boron carbide models.

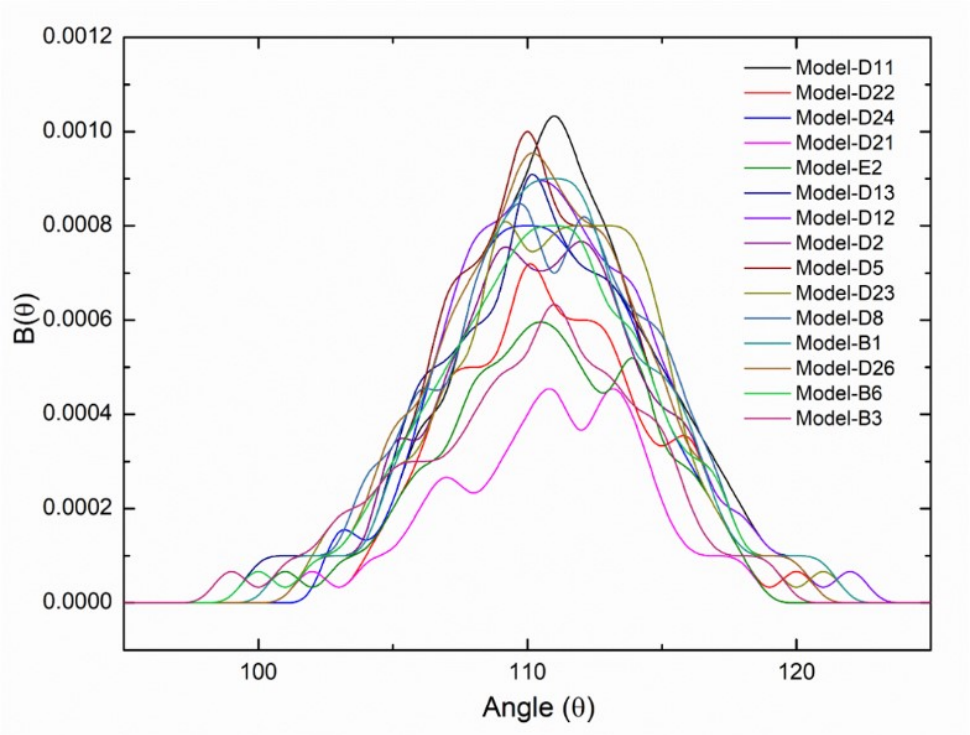

Figure 44. C-C-H bond angle distribution present in the amorphous hydrogenated boron carbide models.

Radial Distribution Function. The *g(r)* information provides the ordering information that is present in the structure. The *g(r)* of all the models were calculated and plotted together as can be seen in Figure 45**.** The distinguishable *g(r)* peaks at ~ 1.1 Å, ~ 1.3 Å, ~ 1.8 Å, ~ 2.9 Å, and ~ 3.5 Å can be seen in Figure 45. The peaks after ~ 3.5 Å are not distinctive indicating the presence of short-range ordering in the a-B_xC: H_y models. The peak intensity at ~ 1.1 Å is the C-H bonding which can be seen to vary in the intensity with the change in H % in the models. The peak centered at ~ 1.3 Å is the B-H bonding in the structure where drastic changes are seen from Model-D11 with maximum hydrogen concentration of 42 % to no peak at all for Model-B3 with the lowest hydrogen concentration of 16 %. The amount of boron in the a-B_xC: H_y models ranges from 47-66 %. The peak intensity at ~ 1.8 Å, ~ 2.9 Å, and ~ 3.5 Å are the first, second and third neighboring distance between the boron atoms in the icosahedral structure. However, the peaks

at ~ 1.8 Å, ~ 2.9 Å is also overlapped with B-C pairs. Model-D26 has the highest peak intensity at ~ 1.8 Å where Model-D11 has high intensity at the ~ 3.5 Å region.

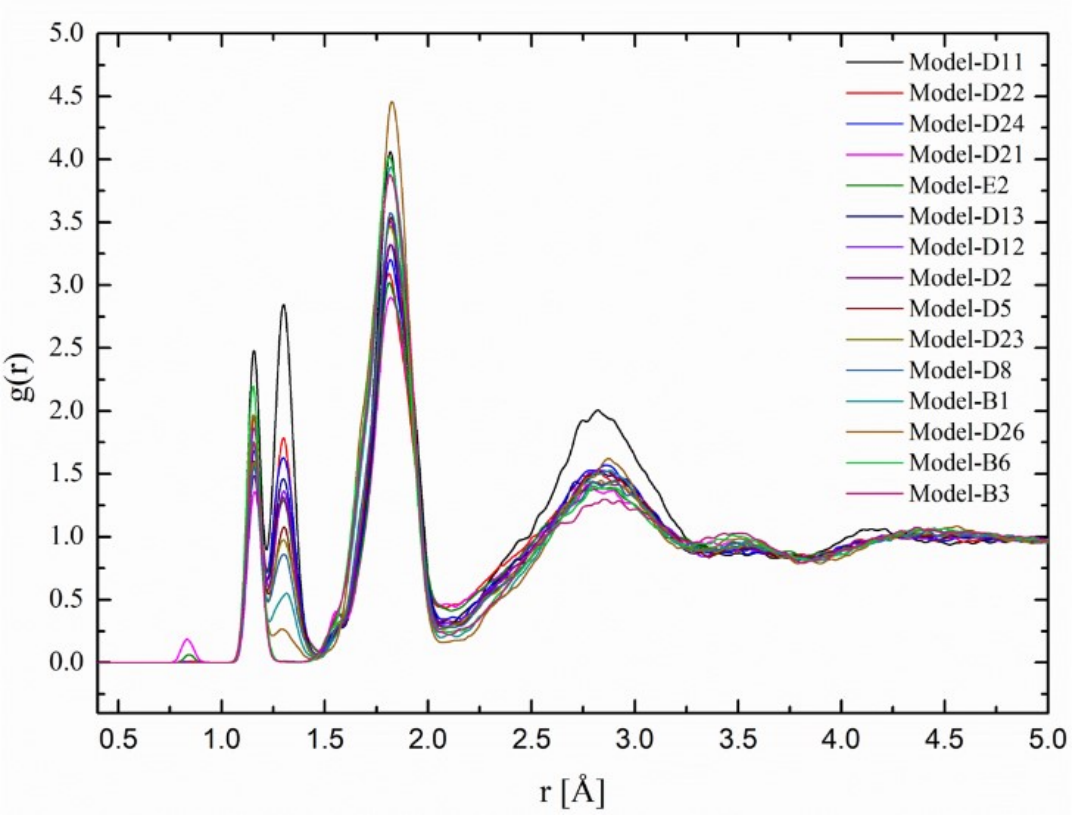

Figure 45. The radial distribution function of all the amorphous a-B_xC: H_y models.

Table 12 provides insight on the variation of the peak intensity of *g(r)* on all the models of a-B_xC:H_y based on their stoichiometry, simulation parameter and density of the models. The C-H peak at ~ 1.1 Å is found to vary based on B/C stoichiometry. This effect is as expected since the addition of CH_2 linkers were solely based on maintaining B/C ratio in the initial starting models. The peak in between 1.25-1.5 Å is the B-H bonding which has the highest degree of correlation as observed earlier in case of B-H bond count and even in the case of B-B-H and B-C-H bond angle distribution. The variation of intensity in this region is independent of

simulation variable which makes it a reliable variable to compare with the experimental *g(r)*. The highest intensity peak is observed in the region of 1.5-2 Å. The peaks in this region are overlapped in between B-C and B-B bonds. The intensity variation in this region found to be dependent on both the H % as well as the applied pressure. With the decreasing H % and pressure the peak intensity is found to increase. The fourth peak has wide distribution ranging from 2-3.25 Å. The intensity of the peak in this region is found to decrease with the increase of density of the sample. To unravel the more detailed picture the partial radial distribution function is discussed.

Figure 46 gives the boron to boron partial radial distribution function for all the models. These models are plotted as a function of decreasing H %. The peak positions are clearly seen at ~ 1.8 Å, ~ 2.9 Å, and ~ 3.5 Å. These are the first, second and third neighbor distances of the boron atoms. The majority of the signal below 3.5 Å comes from the icosahedra. The signal intensity after that is broad indicating the presence of short-range order in the a-B_xC:H_y models. All the intensity peaks have a higher degree of correlation with H-concentration in the structure. With the decreasing H % the intensity is found to increase. The decrease of H % in the sample is essentially the decrease of H/Icosahedra. As the H/Icosahedra decreases the chances of B-B bonding increases. This phenomenon is actually found to be true from the B-B bond counts in the earlier discussion. Although not intuitive from the graph in Figure 46 the correlation coefficients from Table 12 reveal the secret. The second peak is also found to strong negative correlation with the applied pressure indicating the possible distortion of the icosahedra. The third peak is particularly found be almost perfectly correlated with the H % and the density in the samples.

The B-C partial radial distribution function intensity peaks are shown in Figure 47. There are noticeable three peaks in the B-C *g(r)* at ~ 1.55 Å, ~ 1.8 Å, and ~ 2.8 Å. The peaks at ~ 1.8 Å are the regular bond length between the B-C atoms and at ~ 2.8 Å is the second neighbor of carbon within the icosahedral structure. The C_2-B_8 type of pair as shown in Figure 5 (a) gives

Table 12. The linear correlation coefficient of the *g(r)* of a-B_xC:H_y models with their stoichiometry, simulation parameter, and density. All the correlation coefficient higher than 0.8 are highlighted in the table.

Peak Intensity	Peak position	Stoichiometry		Simulation Parameter	Bulk Property
		H%	B/C	Applied pressure (Gpa)	Density (g/cm^3)
g(r)	1-1.25	0.00	**-0.83**	-0.50	0.00
	1.25-1.5	**0.91**	0.00	0.00	**-0.96**
	1.5-2	-0.70	0.00	**-0.81**	0.43
	2-3.25	0.42	0.00	0.00	-0.67
g(r)_B-B	1.5-2	**-0.83**	0.00	-0.69	0.65
	2-3.3	**-0.83**	0.00	**-0.81**	0.62
	3.3-3.8	**-0.99**	0.00	-0.55	**0.94**
g(r)_B-C	1.4-1.6	0.61	0.00	**0.87**	-0.45
	1.6-2	0.00	-0.43	-0.68	0.00
	2-3.8	**-0.79**	0.00	**-0.83**	0.54
g(r)_B-H	1-1.5	**0.92**	0.00	0.00	**-0.96**
	1.5-2.3	0.61	0.00	**0.87**	-0.48
	2.3-3.5	**0.87**	0.00	0.00	**-0.96**
g(r)_C-C	1.3-2	-0.51	0.00	**-0.83**	0.00
g(r)_C-H	1-1.4	0.00	**-0.83**	-0.51	0.00
	2.0-3	0.56	0.00	0.00	-0.77
g(r)_H-H	1.5-4	**0.99**	0.00	0.59	**-0.94**
	4.0-6	**0.97**	0.00	0.54	**-0.96**

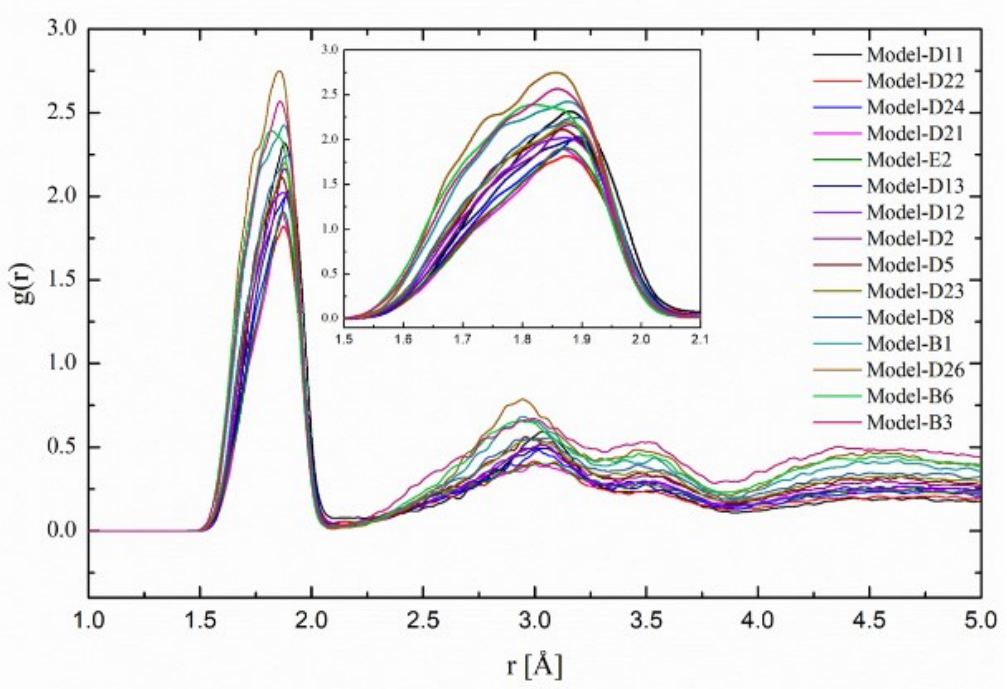

Figure 46. Boron to boron partial radial distribution function for all the a-B_xC:H_y models.

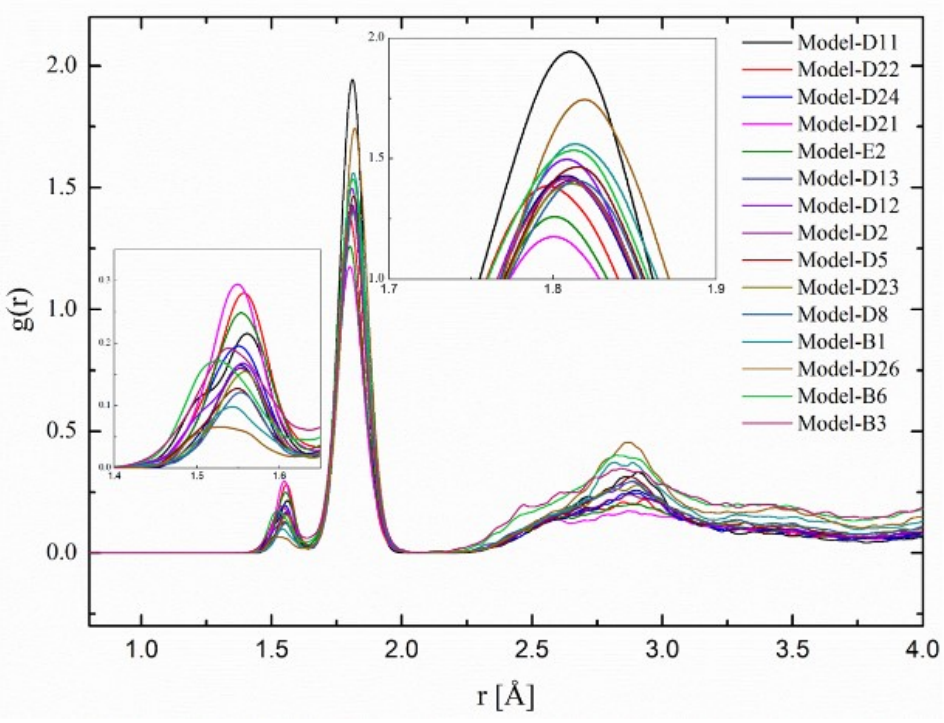

Figure 47. Boron to carbon partial radial distribution function for all the a-B_xC:H_y models.

rise to the second nearest neighbor type interaction. But the peaks at ~ 1.55 Å aren't present in the *ortho*-carborane icosahedral geometry. This peak is the indication of rearrangement or the deformation of the icosahedral structure. Figure 48 shows the B-C bonds present at 0 ps and after 1 ps of the MD simulation in Model-D21. Even at 300 K some of the C_2B_{10} icosahedral structure goes under rearrangement and gives rise to the shorter bond length peaking at ~ 1.55 Å. It should be noted that this rearrangement occurs in a relatively short time and increases with the applied pressure. The initial icosahedral geometry doesn't contain this short bond length. The intensity of B-C *g(r)* in the region of 2 - 3.5 Å is highly correlated with the H % as well as the applied pressure.

Figure 49 shows the B-H first and second nearest neighbor distance within the *ortho*-carborane molecule. Figure 50 is the B-H partial radial distribution function in the a-B_xC:H_y models. The B-H has the intensity peaks at ~ 1.3 Å and at ~ 2.8 Å with a small shoulder peak at ~ 2.1 Å. The ideal *ortho*-carborane has B-H bond length of ~ 1.2 Å and a second nearest neighbor H-atom at ~ 2.6 Å but for the ReaxFF these length extends to ~ 1.3 Å and at ~ 2.8 Å. The peak at ~ 2.1 Å actually arises when the icosahedral structure deforms and then the second neighbor comes closer to certain B-atoms. This analysis is backed up by the statistical linear correlation coefficient calculation which shows the peak at ~ 2.1 Å increasing linearly with the applied pressure in Table 12. Also, the first peak and third peak are a good indicator of the H % and correlate strongly with the density of the a-B_xC:H_y material. These two peaks are also independent of the applied pressure during the simulations.

Statistically the amount of carbon in the structure is very small which spans from 10-16 % in all of the a-B_xC:H_y models. The majority of the carbon atoms reside within the C_2B_{10} icosahedral structure. Figure 51 gives the partial radial distribution function of C-C pairs within

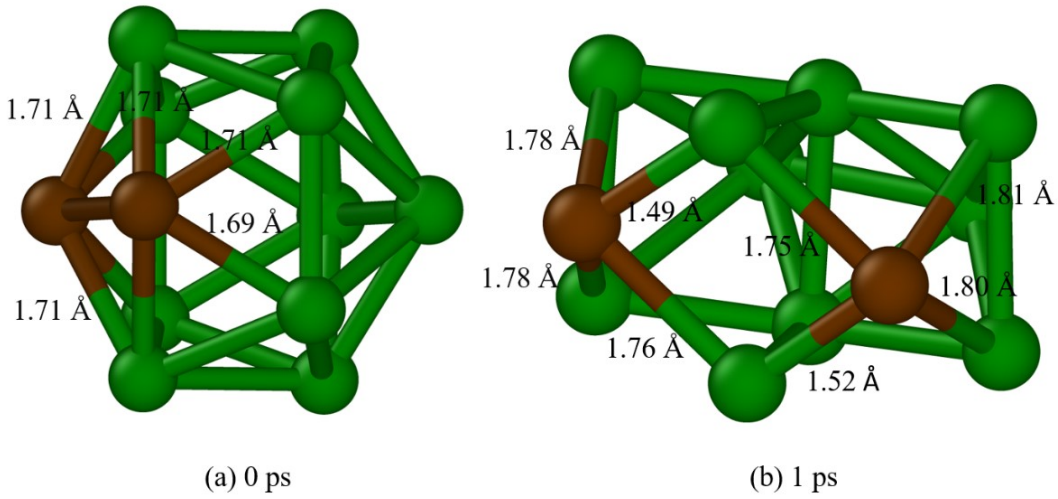

Figure 48. C_2B_{10} icosahedral structure in the a-B_xC:H_y models (a) At 0 ps, (b) After 1 ps. (Green = boron, Brown = carbon, H-atoms are removed for the better visualization)

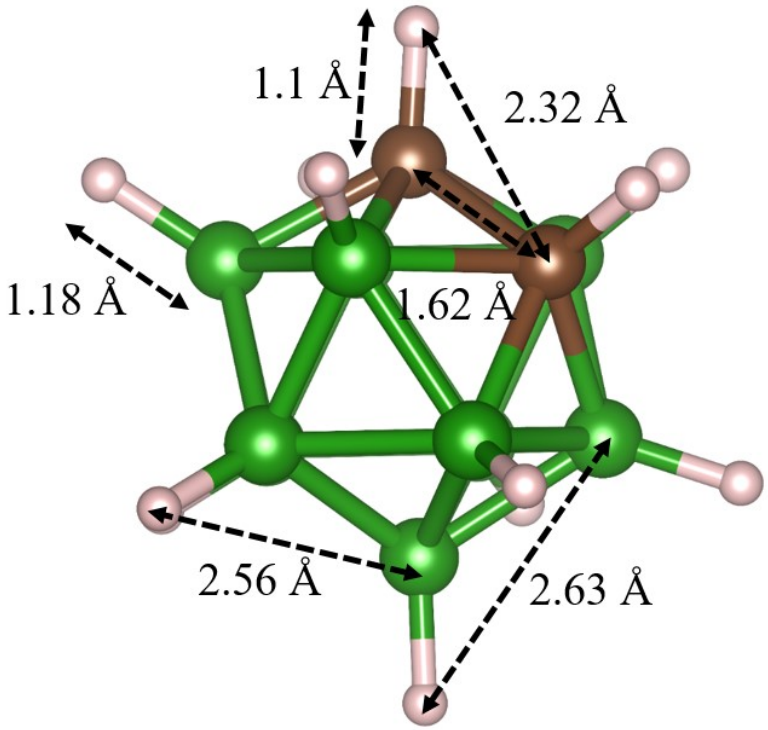

Figure 49. Orthocarborane with the second nearest neighbor distance for B-H and C-H. (Green = boron, Brown = carbon, White = hydrogen atoms.)

the cutoff distance of 5 Å. The first and the major peak position is at ~ 1.7 Å and a small second peak at ~ 2.7 Å. The *ortho*-carborane molecule has a C-C bond length of ~ 1.62 Å but due to the thermal excitation and applied pressure during the ReaxFF-MD simulation the C-C bond length increases to ~ 1.7 Å. The C-C at ~ 1.7 Å is seen to have strong negative correlation with the pressure parameter of the MD-simulation.

The C-H partial radial distribution function is shown in Figure 52. The first sharp peak is observed at ~ 1.16 Å and a very small second nearest neighbor intensity peak is observed at ~ 2.3 Å. The first peak is the C-H bond length in the dehydrogenated *ortho*-carborane structure as well as the CH_2 hydrocarbon linker group and the second peak is the H-atom attached to the nearest C-atom within in the *ortho*-carborane as shown in Figure 49.The intensity of the first C-H peaks varies strongly with the B/C stoichiometry.

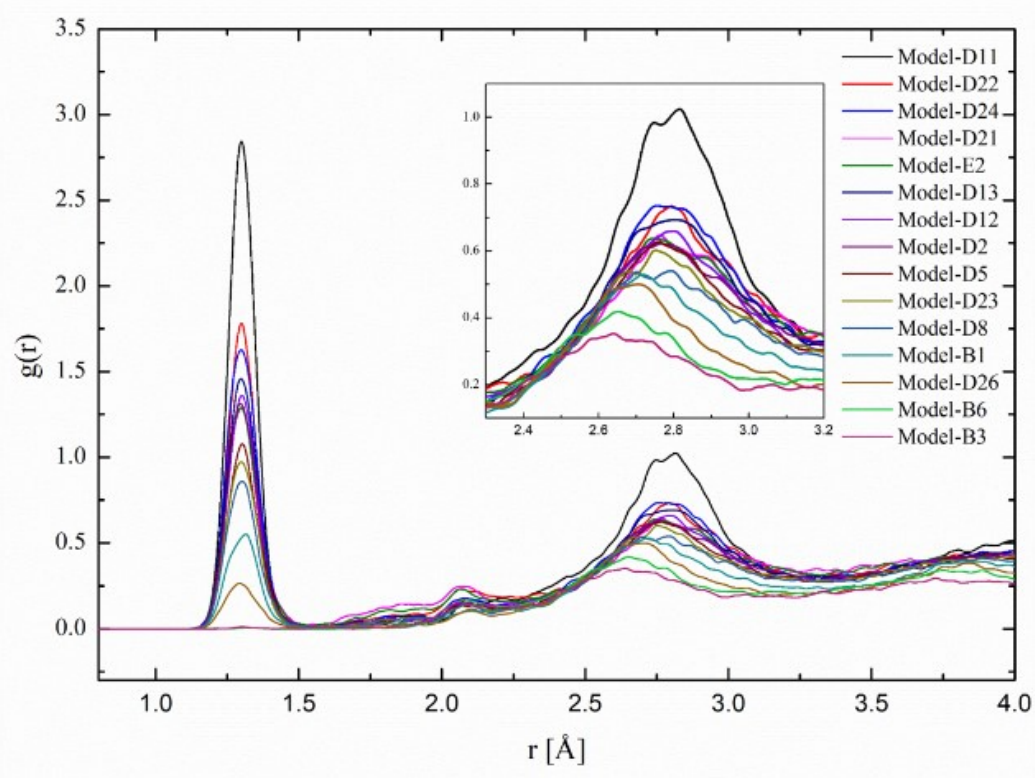

Figure 50. Boron to hydrogen partial radial distribution function for all the a-B_xC:H_y models.

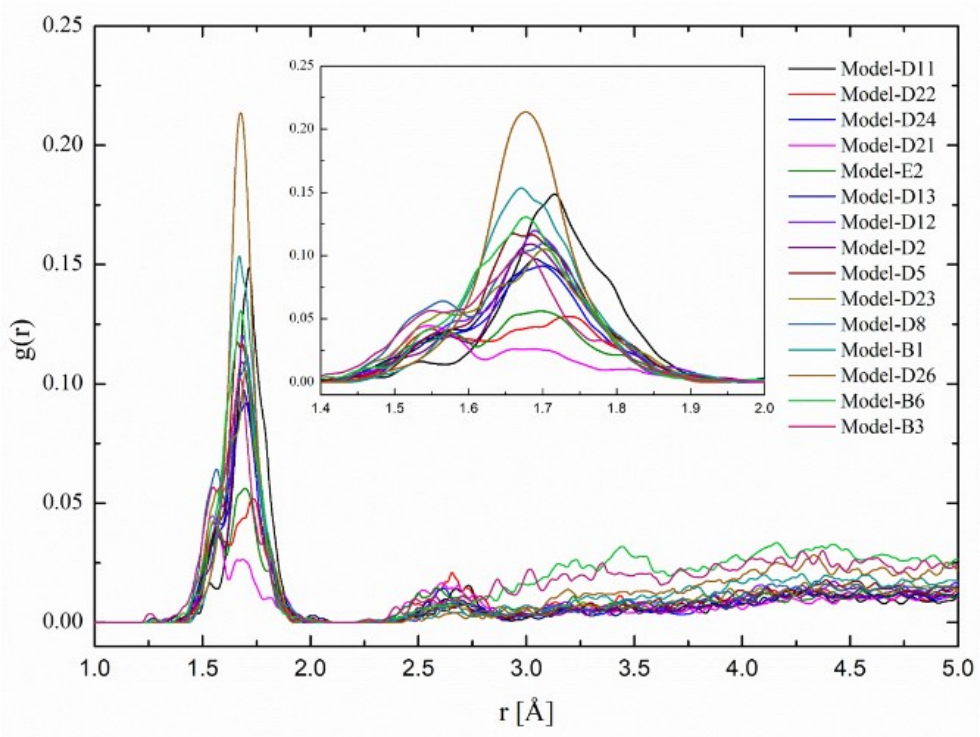

Figure 51. Carbon to carbon partial radial distribution function for all the a-B_xC:H_y models.

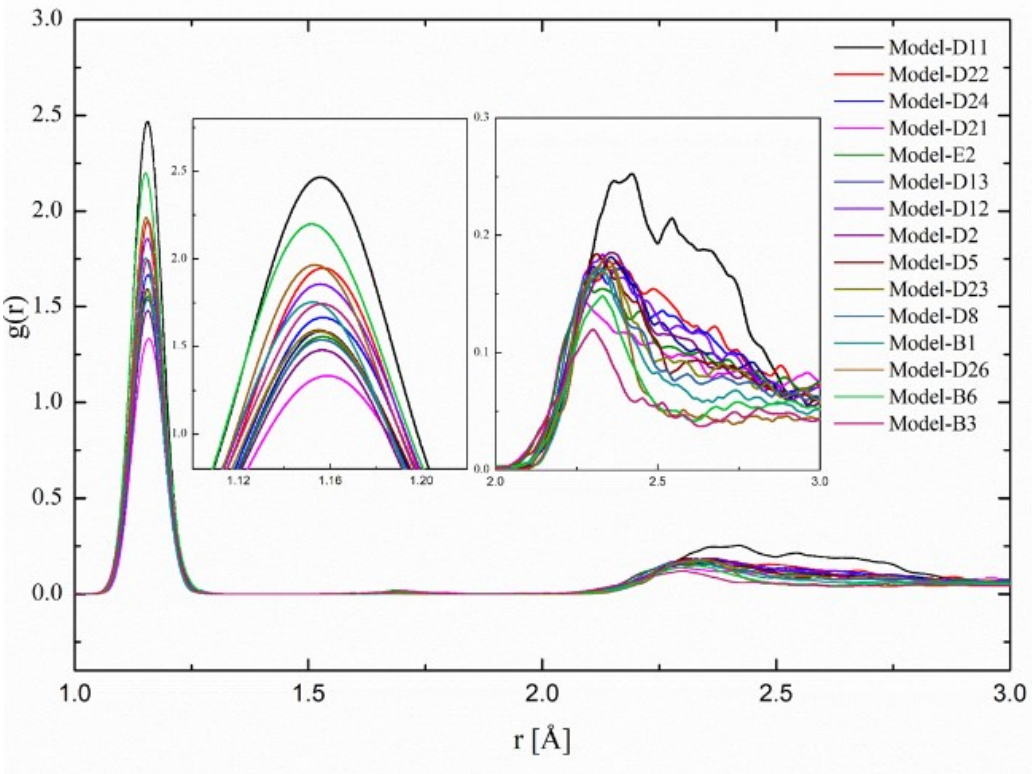

Figure 52. Carbon to hydrogen partial radial distribution function for all the a-B_xC:H_y models.

As the CH_2 group is added in the initial configuration the B/C ratio goes on decreasing that is why the first peak of C-H shown the negative correlation with the B/C stoichiometry in Table 12. The second peak which arises predominantly from the icosahedral C_2B_{10} is found to increase with the increasing H % in the a-B_xC:H_y.

Finally, the H-H pair distribution function is shown in Figure 53. There are some peaks at ~ 1.8 Å, ~ 2.5-2.6 Å, ~ 3.25 Å, and ~ 5.25 Å. Since the H % in the structure is overwhelming it's difficult to decipher the exact location of H-H *g(r)*. However, within the *ortho*-carborane icosahedral geometry, the H-H pair are fixated at a particular location as shown in Figure 54. The first neighbor is around 3.07-3.15 Å, second neighbor of H-atoms attached to B-atoms are 4.94 -

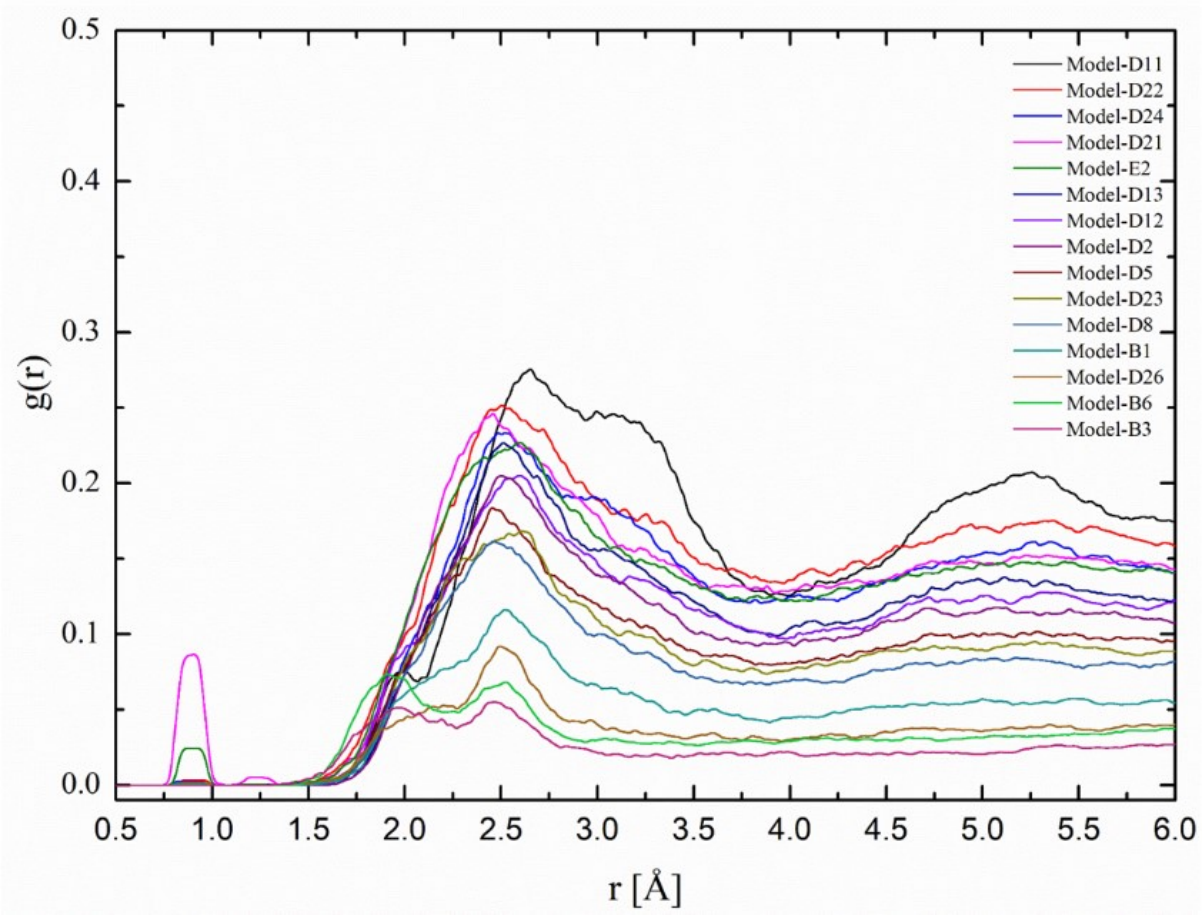

Figure 53. Hydrogen to hydrogen partial radial distribution function for all the a-B_xC:H_y models.

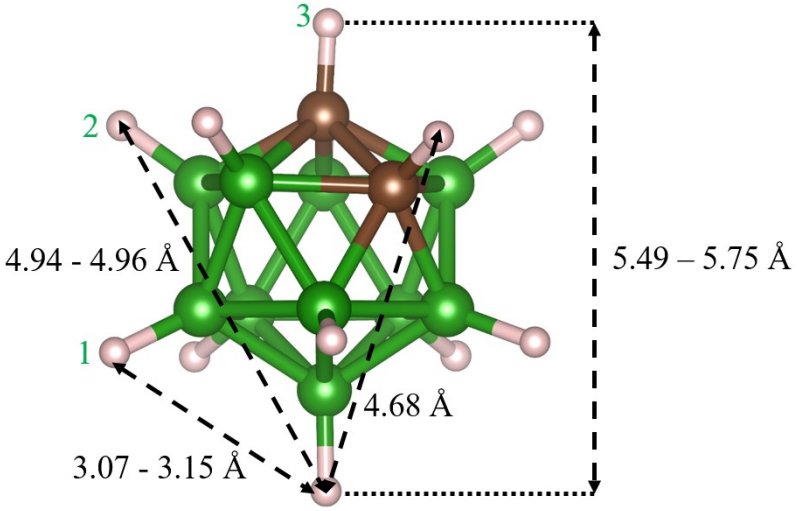

Figure 54. Orthocarborane with the nearest neighbor distance for H-atom. (Green = boron, Brown = carbon, White = hydrogen atoms.)

4.96 Å apart whereas H-atoms attached to C-atoms are closer at 4.68 Å, third neighbor is within the distance of 5.49 - 5.75 Å. The peaks ~ 3.25 Å, and ~ 5.25 Å are most likely the H-H pairs coming from the first and second neighbor from the dehydrogenated *ortho*-carborane. Another source of H-H pair distribution distance is within the CH_2 hydrocarbon linkers which are found to be between 1.77 - 2.15 Å. Most likely, the first and the second peak arises from the H-H pairs in the linkers. The other intermediate-range of pairs comes when the two icosahedra's come close together during the densification process. An important correlation of H-H pairs is with the H % as well the density of the a-B_xC:H_y models.

Next, we opted out to calculate the neutron diffraction static structure factor (*S(Q)*) of a-B_xC:H_y models. This reciprocal space property is plotted in Figure 55. The *S(Q)* peaks are observed in the location ~ 1 $Å^{-1}$, ~ 2.9 $Å^{-1}$, ~ 4.7 $Å^{-1}$, ~ 7.5 $Å^{-1}$, ~ 11.5 $Å^{-1}$ and the oscillating slowly dies out. The *S(Q)* presented in Figure 55 is typical of disordered solids and amorphous materials. These peak positions can be analyzed and explained on the basis of their correlation with the stoichiometric property, simulation parameter, and their density. Table 13 lists out the

linear correlation coefficient of the *S(Q)* peak positions with H %, B/C ratio, applied pressure and density of the material. At first glance it is visible only the peak at ~ 2.9 $Å^{-1}$ is varying based on B/C ration. The intensity peaks at ~ 4.7 $Å^{-1}$ and ~ 7.5 $Å^{-1}$ are increasing with decreasing H % or in other words increasing with increasing density of the a-B_xC:H_y models. Also, these peaks

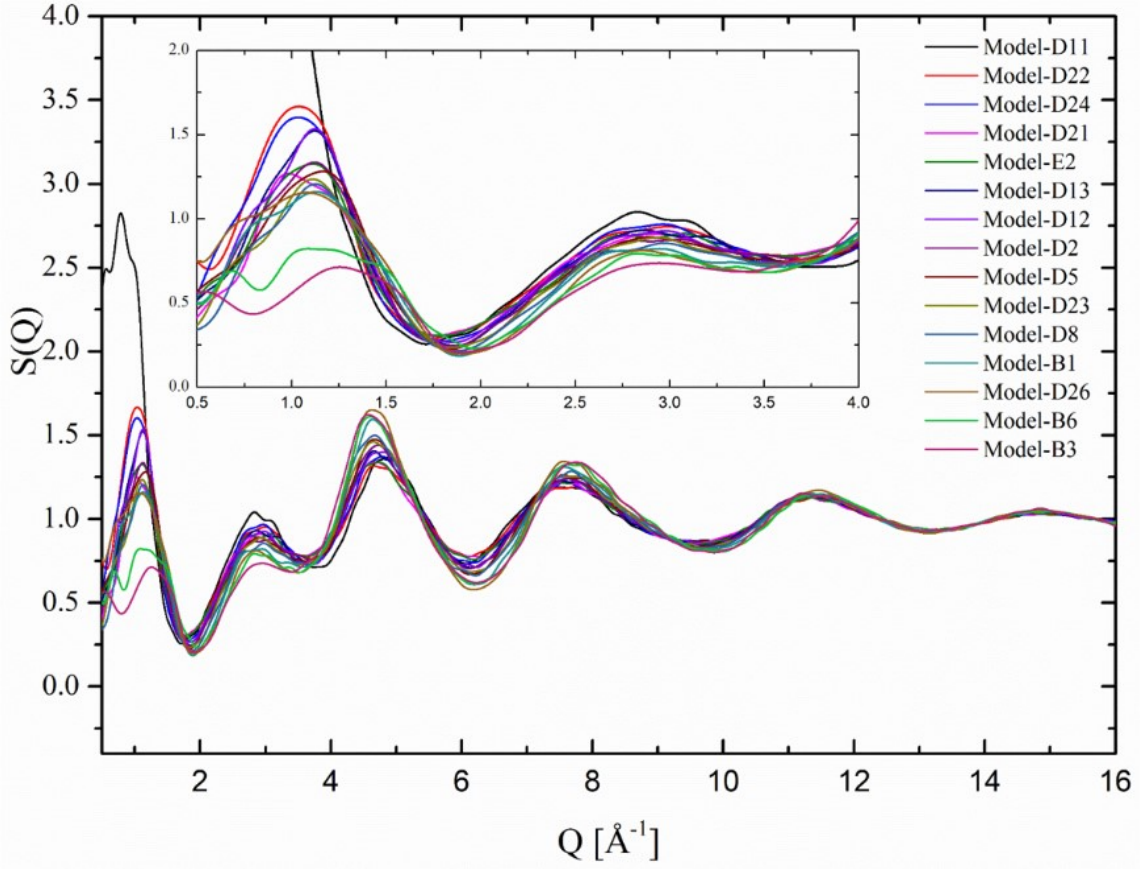

Figure 55. Structure factor *S(Q)* comparison for all the a-B_xC:H_y models.

are moderately correlated with the simulation pressure. The strong signal at ~ 1 $Å^{-1}$, on the other hand, is positively correlated with the H-content and shows no dependence on applied pressure whatsoever. The *S(Q)* signal at ~ 11.5 $Å^{-1}$ has a mixed response and is found to moderate linear correlation with all the parameters other than B/C stoichiometry. This brings us to logically

conclude that first, third and fourth are the indicators of H-concentration whereas the second peak varies based on the B/C ratio.

Table 13. The linear correlation coefficient of *S(Q)* and coordination environments of a-B_xC:H_y models with their stoichiometry, simulation parameter, and density.

Peak Intensity	Peak position	Stoichiometry		Simulation Parameter	Bulk Property
		H%	B/C	Applied pressure (Gpa)	Density (g/cm^3)
	0.5-2	0.74	0.00	0.00	**-0.89**
	2.0-4	0.00	-0.52	0.00	0.00
S(Q)	4.0-6	**-0.97**	0.00	-0.71	**0.85**
	6.0-10	**0.98**	0.00	-0.59	**0.92**
	10.0-13	-0.69	0.00	-0.70	0.55
B-Coordination	-	**-0.98**	0.00	-0.69	**0.88**
C-Coordination	-	0.00	0.00	-0.72	0.00
H-Coordination	-	**-0.80**	-0.56	-0.65	0.63
Total Coordination	-	**-0.99**	0.00	-0.63	**0.91**

Structural Units and Coordination Number. The structural units and coordination number analysis provide a much deeper peek in the structure of amorphous materials. As mentioned earlier the structural units are calculated based on the first nearest neighbor surrounding a central atom. The number of structural units depends upon the geometrical structure and the no. of elements in the system. For our 3 element system of B, C, and H containing icosahedral geometry there were 81 different types of structural bonding environment identified in the a-B_xC:H_y structures. We have ignored the structural bonding environment that is present in less than 1 % as these structural units fluctuate slightly based on the cutoffs used. However, the structural units though less than 1 % but present in all the structures are included here. Based on this classification there are 21 B-centered, 10 C-centered and 2 H-centered

structural units. Figure 56, Figure 57, Figure 58, and Figure 59 presents the B-centered structural bonding environments plotted as a function of decreasing H % in the a-B_xC:H_y models. The B-centered environments <u>B</u>-B_2CH, <u>B</u>-B_2C_2, <u>B</u>-B_2C_2H, <u>B</u>-B_3CH, <u>B</u>-B_3C in Figure 56 and <u>B</u>-B_4, <u>B</u>-B_4H in Figure 57 shows the negative slope with the increasing density of the samples. The units such as <u>B</u>-B_2C_3 and <u>B</u>-B_4C shows no clear correlation with the H-content of the a-B_xC:H_y structures. All other remaining B-centered environments are increasing with the increasing density and decreasing H % in the amorphous models. The higher coordinated boron especially in Figure 58 and Figure 59 are found to have a strong correlation with the density of material. This statistical analysis is consistent with the B-B bond counts discussed earlier.

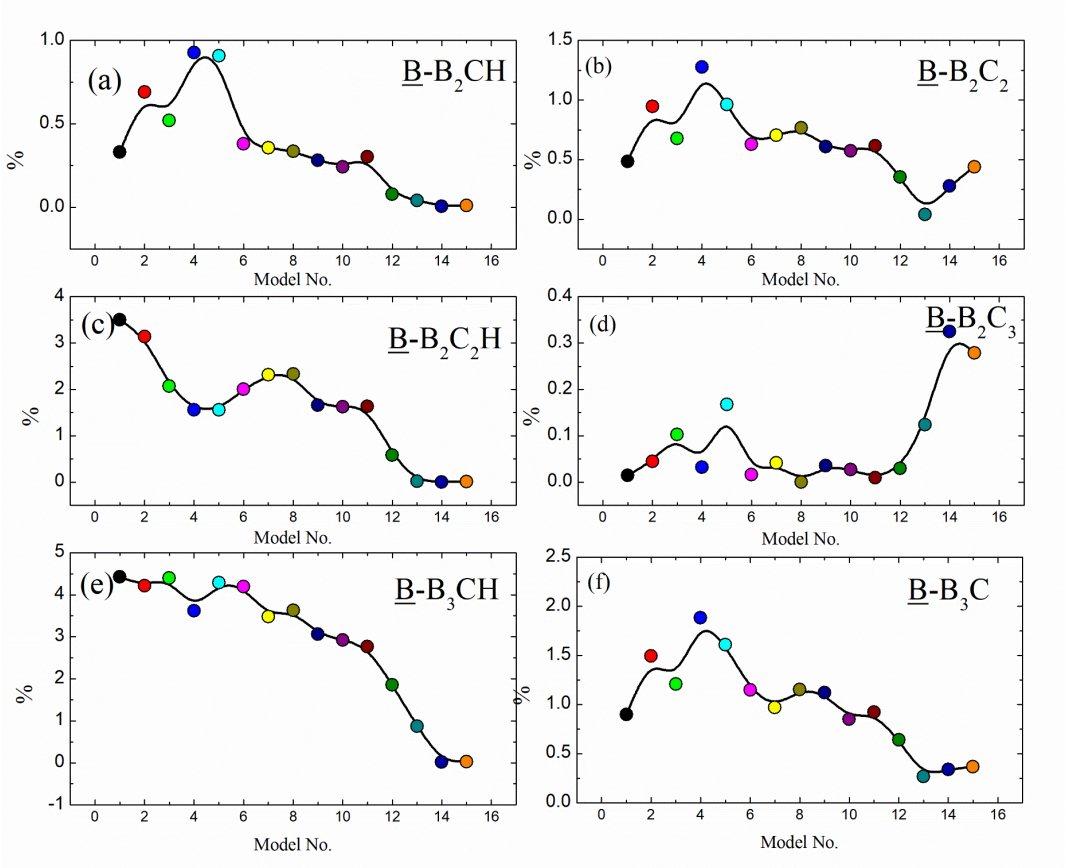

Figure 56. Boron centered structural units present in the a-B_xC:H_y models.

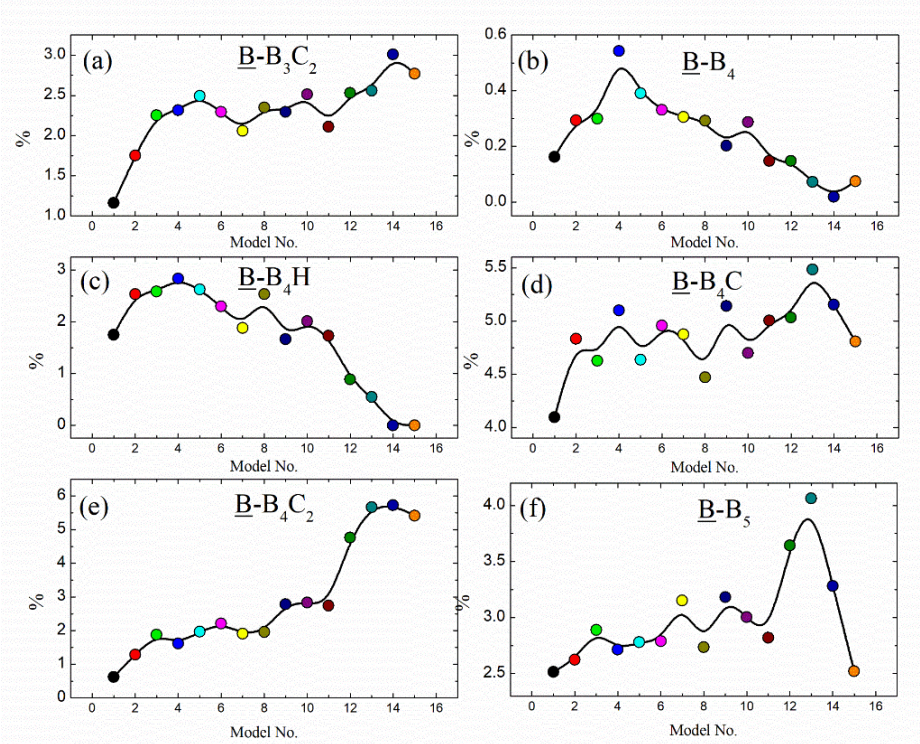

Figure 57. Boron centered structural units present in the a-B_xC:H_y models.

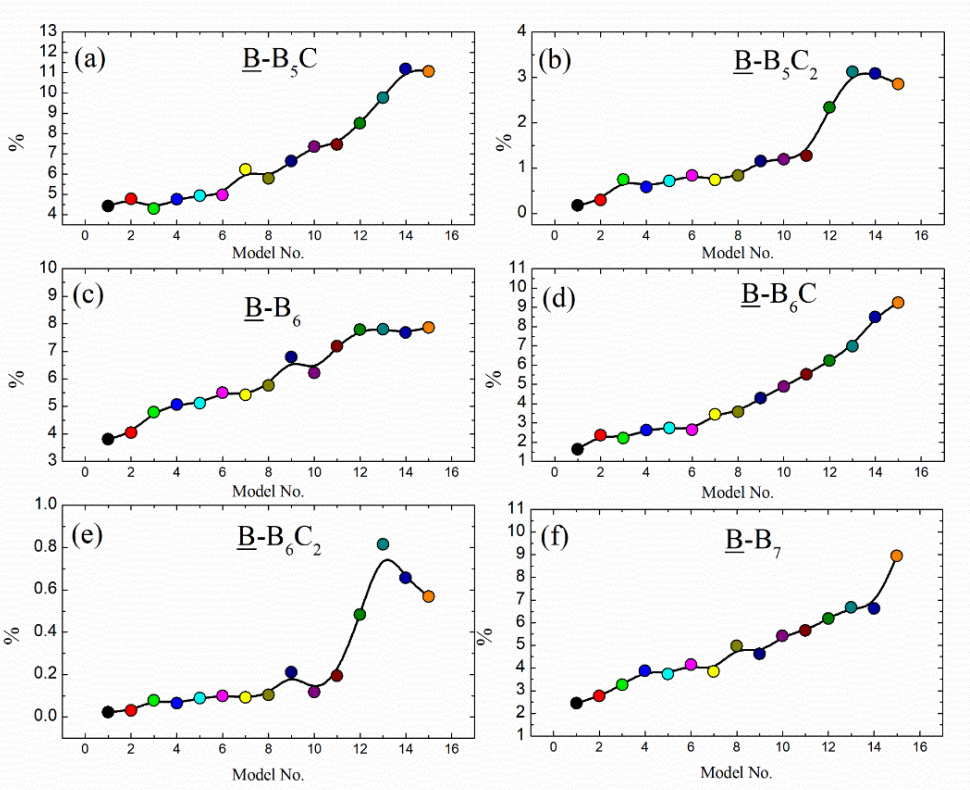

Figure 58. Boron centered structural units present in the a-B_xC:H_y models.

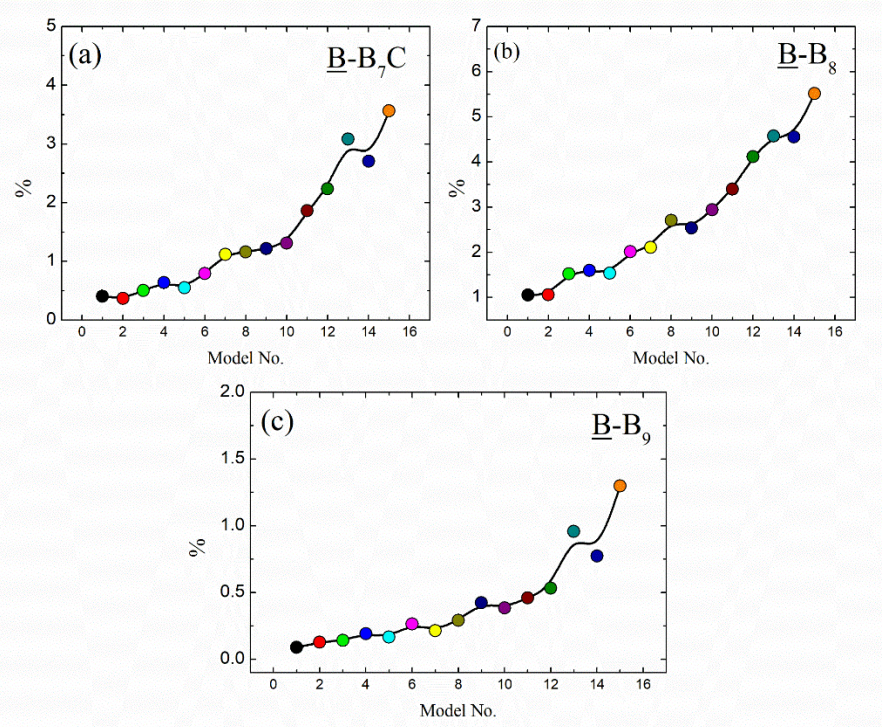

Figure 59. Boron centered structural units present in the a-B_xC:H_y models.

The C-centered environment presented in a statistically significant amount in the models is presented in Figure 60 and Figure 61. Since C-atoms are present in a low amount the structural environments relating to it are also present in lower amount compared to B-centered environments. When plotted as a function of decreasing H-content in the structure the environments such as C-B_2CH, C-B_3CH, C-B_4C, and C-B_4CH shows the increasing tendency whereas C-B_4H, and C-B_5H are found to have decreasing tendency. The remaining C-centered doesn't show clear correlation with the H % or the density. In case of H atom the trends are visibly clear. Figure 62 shows the H-C and H-B bonding environment of H-atom. The H-C bonding environment is almost constant at ~ 13 % for almost all the models with the linear increase from Model-D8 to Model-B6. This is due to the linear decrease of B/C ratio from 4.92 to 4.06. In other words the C % in the structure is increasing in this region from 12-16 %. The H-

B structural unit in Figure 62 (b) is linearly decreasing with the decreasing H % in the material. This is happening as the no. of H-centers is decreasing with the dehydrogenation of B-atoms in the *ortho*-carborane molecules. Finally, the average of carbon and boron centered environment present in all the models are calculated and shown in Figure 63. This quickly reveals that C-B_3CH, C-B_4H, and C-B_4CH stand out and are present more than 2 % in the samples. The likelihood of these environments that can be seen during experimental characterization is higher than other C-center structural units which are on average less than 0.5 %. Much more detailed analysis can be generated out of the structural units but it is out of the scope of this work.

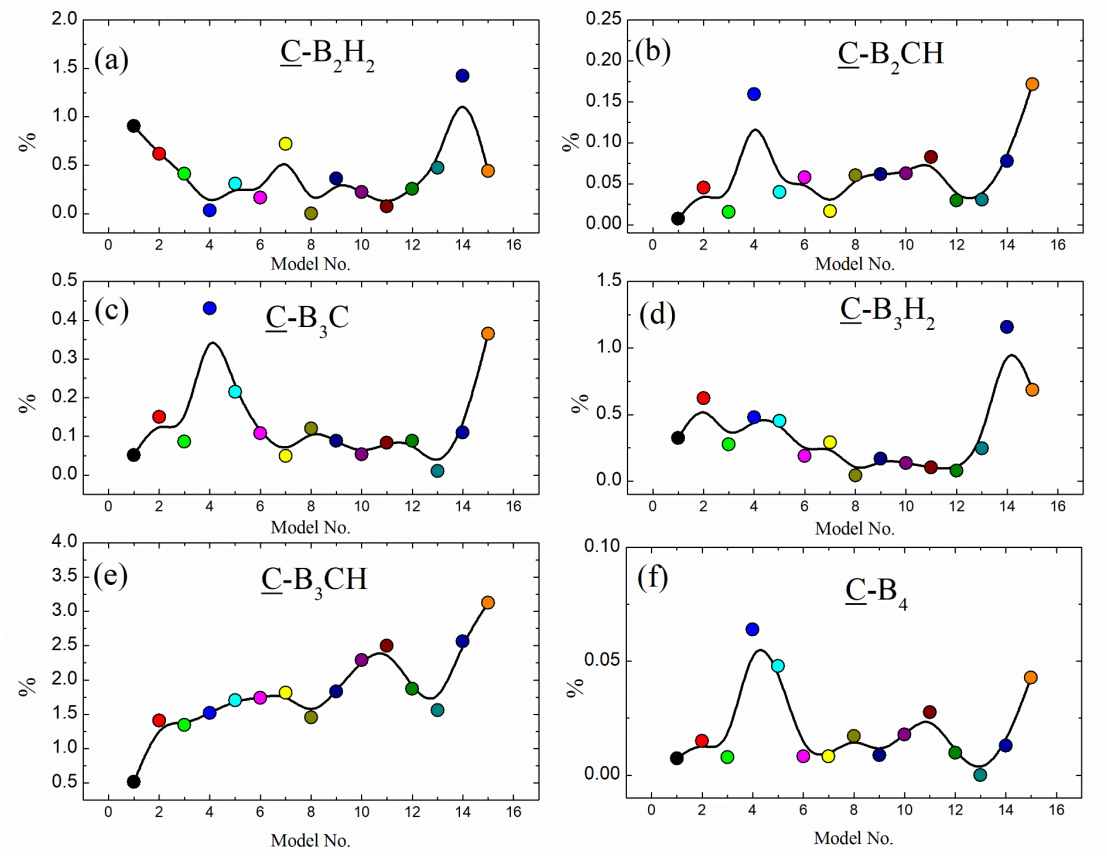

Figure 60. Carbon centered structural units present in the a-B_xC:H_y models.

Last but not the least coordination no. of boron, carbon, hydrogen, and the total is calculated and presented in Figure 64. In general, the boron coordination is increasing with the increasing density of the models and reaches as high as ~ 6.5 with a low of ~ 5.6. Hydrogen coordination shows somewhat decreasing trend from Model-D11 to Model-21 and then increasing nature with density of material. The carbon atom gives a mixed response but within a small window of 5.2 - 5.7. The total coordination number is a mirror image of the boron coordination but linearly increases from ~ 3.6 to ~ 5.5. Boron, hydrogen and total coordination no. is found to have strong linear correlation with H % as can be seen in Table 13 whereas carbon coordination is found be affected by the applied pressure during the simulation. The getaway information from the average coordination no. calculation is that the overall coordination no. increases with the density of models with most of the contribution coming from boron atom.

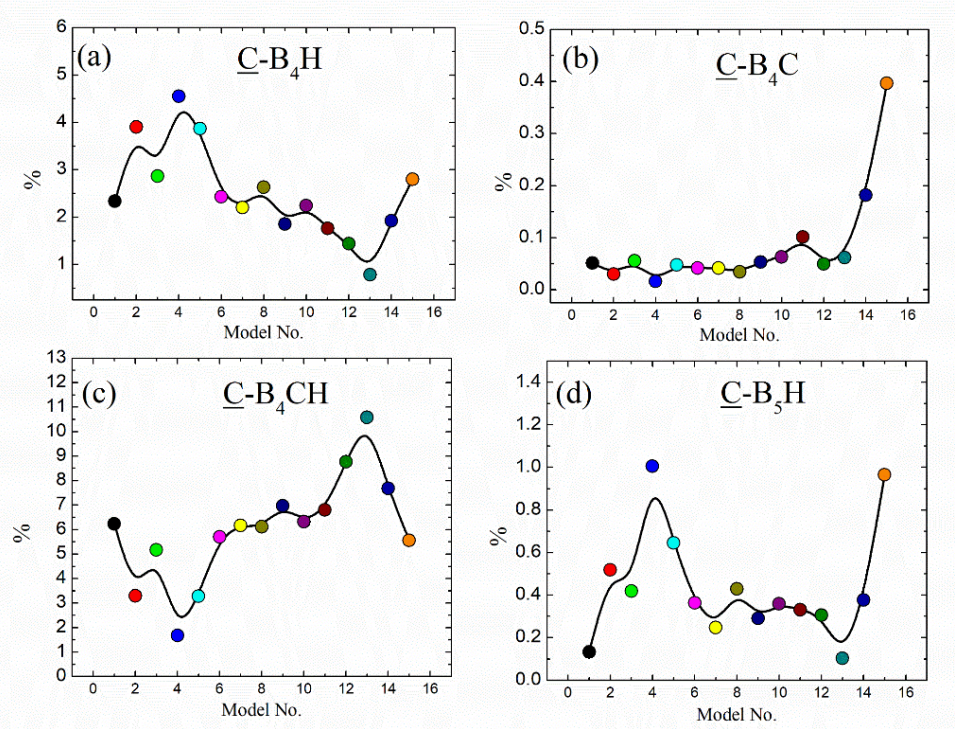

Figure 61. Carbon centered structural units present in the a-B_xC:H_y models.

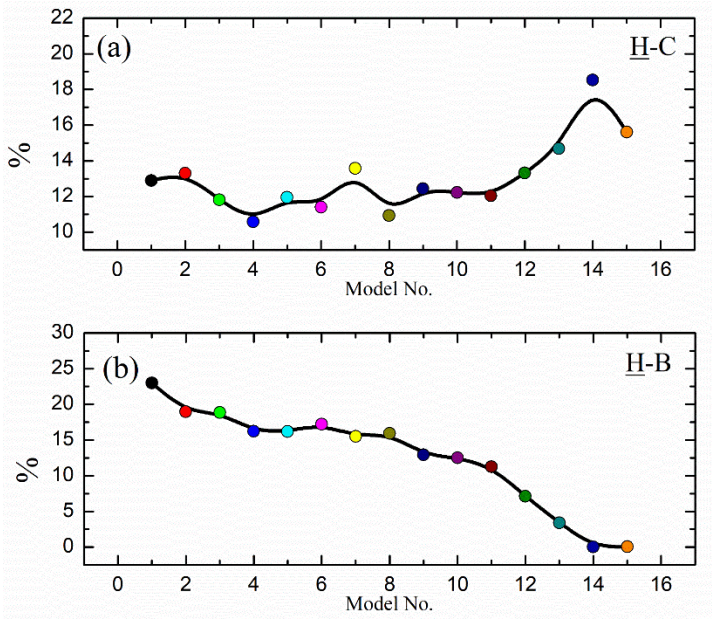

Figure 62. Hydrogen centered structural units present in the a-B_xC:H_y models.

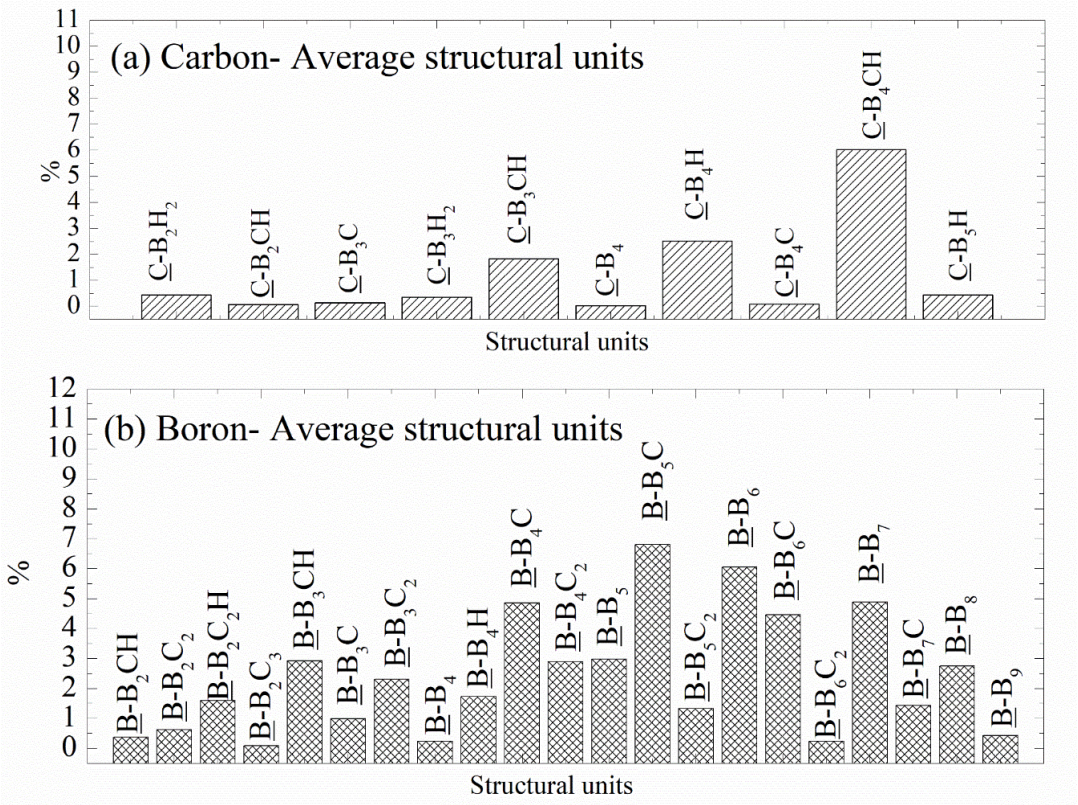

Figure 63. Boron and carbon-centered average structural units present in the a-B_xC:H_y models.

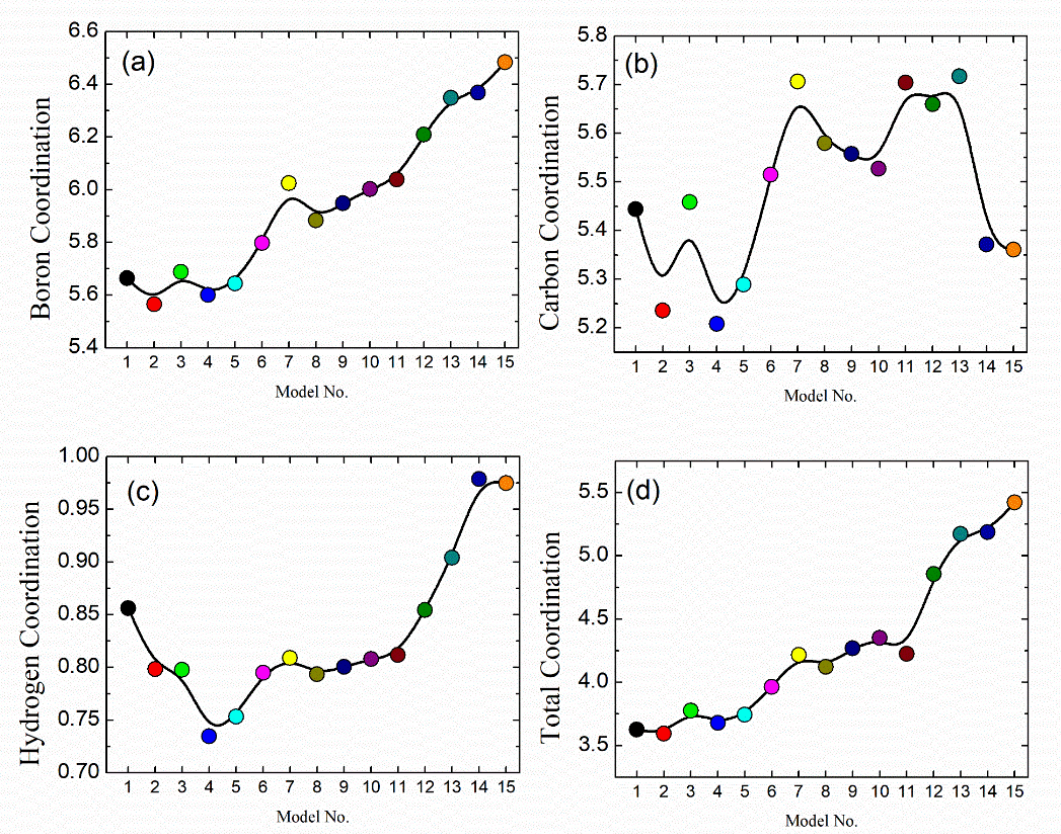

Figure 64. Coordination distribution of boron, carbon, hydrogen present in the a-B_xC:H_y models.

CONCLUSIONS

We have performed MD simulations to study the short-range order present in the different variants of amorphous boron carbide using the SW and ReaxFF potentials. The existing SW potential of the boron cluster was optimized for α-rhombohedral boron and for B_{12}-(CCC), B_{12}-(CBC), and $B_{11}C_p$-(CBC) crystal structure based on their geometry. Amorphous models of boron carbide of three different variants were generated using New SW and ReaxFF and compared. The amorphous boron carbide models are fairly comparable in terms of peak positions and heights with the exception of a fairly sharp second neighbor peak generated by the New SW in *g(r)* and the bond angle at ~ 110° which is attributed to the limitation inherent in the interatomic SW formulation. The sophistication of ReaxFF allows a wide distribution of bonds and angles in the structure whereas the simplicity of SW limits the choices and sharpens the peaks.

In our SRO study of a-B_xC, we were able to show that the presence of icosahedral structures can be recovered in part by utilizing the RDF peaks at ~ 3.4 Å which is traced to the edge to edge Boron atom connections within the clusters. Similarly, a strong characteristic signal was also seen in the *S(Q)* near the vicinity of 4.5 $Å^{-1}$. The pentagonal cap in the icosahedra was discerned through the <u>B</u>-B_5 structural unit environment. In addition, we were able to differentiate between $B_{11}C$ and B_{12} icosahedrons in the amorphous structure via partial bond angle distribution of B-B-C. $B_{11}C$ was found to have a sharp peak at ~ 60° which is nominal in B_{12} present amorphous structures. SRO of a-B_{12}-(CCC), a-B_{12}-(CBC), and a-$B_{11}C_p$-(CBC) were distinguishable based on BC pairs in *g(r)*. a-B_{12}-(CCC) had no short bond peak at ~1.4 Å coming to the chain atom and the intensity of split BC peaks was found to be higher in the case of a-$B_{11}C_p$-(CBC) compared to a-B_{12}-(CBC) in ReaxFF models. However, the New SW potential

couldn't differentiate between the BC pairs in chains and in icosahedral (*inter*- or *intra*-) bonding. Overall, the HRMC simulations utilizing the New SW potential were able to accurately reproduce the bonding environment, angular distribution, real and reciprocal space properties as in the parent MD models.

We have also studied the structural characteristics of amorphous hydrogenated boron carbide material prepared out of the single-source precursor *ortho*-carborane with the PECVD process. We prepared 15 different samples spanning the stoichiometry space of H-concentration in the structure from 16 - 42 %, B/C ration from 4.06 to 5.00 and the density of the material from 0.97 - 2.16 g/cm^3. All of these samples were prepared using MD simulation with the accurate ReaxFF interatomic potential. These models are prepared within 2 % of experimental density and have the exact stoichiometry as in the reported experimental samples. We have applied the densification scheme during the preparation of these structures and it should be noted that models are free from the internal stress. Thus prepared models are characterized for bond counts, bond angle distribution, radial distribution function, static structure factor, and coordination number to provide insight into the structure of a-B_xC:H_y. The variation of structural property with the stoichiometry and density of sample is studied using the linear correlation coefficient calculation.

The linear increase of B-B bond along with the decease of B-H bond count is identified as a key factor responsible for the density of a-B_xC:H_y material. The C-atom in the structure is found to have only played the role of maintaining the resulting stoichiometry of the material. The B-B-H and B-C-H bond angles are identified as a characteristic signal to quantify the H-presence in the icosahedral geometry of dehydrogenated *ortho*-carborane and B-B-B angle is found to have played an important role in the densification process. The intensity of the BC *g(r)* peak at ~

1.5 Å and BH *g(r)* peak at ~ 2.1 Å is a signal indicating the rearrangement or the distortion of the icosahedral geometry.

REFERENCES

[1] N.S. Hosmane, J.A. Maguire, Z. Yinghuai, Polyhedral boron cage compounds: an account, Main Gr. Chem. 5 (2007) 251–265, https://doi.org/10.1080/10241220701607501.

[2] M.M. Balakrishnarajan, P.D. Pancharatna, R. Hoffmann, Structure and bonding in boron carbide: The invincibility of imperfections, New J. Chem. 31 (2007) 473–485, https://doi.org/10.1039/B618493F.

[3] H. Werheit, A. Leithe-Jasper, T. Tanaka, H.W. Rotter, K.A. Schwetz, Some properties of single-crystal boron carbide, J. Solid State Chem. 177 (2004) 575–579, https://doi.org/10.1016/j.jssc.2003.04.005.

[4] M. Beauvy, Stoichiometric limits of carbon-rich boron carbide phases, J. Less Common Met. 90 (1983) 169–175, https://doi.org/10.1016/0022-5088(83)90067-X.

[5] C. Pallier, J.-M. Leyssale, L.A. Truflandier, A.T. Bui, P. Weisbecker, C. Gervais, H.E. Fischer, F. Sirotti, F. Teyssandier, G. Chollon, Structure of an Amorphous Boron Carbide Film: An Experimental and Computational Approach, Chem. Mater. 25 (2013) 2618–2629, https://doi.org/10.1021/cm400847t.

[6] F. Thévenot, Boron carbide—A comprehensive review, J. Eur. Ceram. Soc. 6 (1990) 205–225, https://doi.org/10.1016/0955-2219(90)90048-K.

[7] N. Hong, J. Mullins, K. Foreman, S. Adenwalla, Boron carbide based solid state neutron detectors: the effects of bias and time constant on detection efficiency, J. Phys. D. Appl. Phys. 43 (2010) 275101, https://doi.org/10.1088/0022-3727/43/27/275101.

[8] J.I. Oñate, A. García, V. Bellido, J.L. Viviente, Deposition of hydrogenated B-C thin films and their mechanical and chemical characterization, Surf. Coatings Technol. 49 (1991) 548–553, https://doi.org/10.1016/0257-8972(91)90115-D.

[9] S. Lin, B.J. Feldman, D. Li, Microhardness study of amorphous hydrogenated boron carbide deposited on a cathode substrate by plasma deposition, Appl. Phys. Lett. 69 (1996) 2373–2375, https://doi.org/10.1063/1.117641.

[10] S. Vepřek, S. Rambert, M. Heintze, F. Mattenberger, M. Jurčik-Rajman, W. Portmann, D. Ringer, U. Stiefel, Development of plasma CVD and feasibility study of boron carbide in-situ coatings for tokamaks, J. Nucl. Mater. 162–164 (1989) 724–731, https://doi.org/10.1016/0022-3115(89)90353-X.

[11] S. Vepřek, M.R. Haque, H.R. Oswald, On the chemical erosion of some low-Z materials by hydrogen plasma and on the possibility of regeneration of the first wall by low pressure plasma CVD, J. Nucl. Mater. 63 (1976) 405–409, https://doi.org/10.1016/0022-3115(76)90356-1.

[12] B.J. Nordell, T.D. Nguyen, C.L. Keck, S. Dhungana, A.N. Caruso, W.A. Lanford, J.T. Gaskins, P.E. Hopkins, D.R. Merrill, D.C. Johnson, L.L. Ross, P. Henry, S.W. King, M.M. Paquette, Conquering the Low-k Death Curve: Insulating Boron Carbide Dielectrics with Superior Mechanical Properties, Adv. Electron. Mater. 2 (2016) 1600073, https://doi.org/10.1002/aelm.201600073.

[13] O.K. Farha, A.M. Spokoyny, K.L. Mulfort, M.F. Hawthorne, C.A. Mirkin, J.T. Hupp, Synthesis and Hydrogen Sorption Properties of Carborane Based Metal−Organic Framework Materials, J. Am. Chem. Soc. 129 (2007) 12680–12681, https://doi.org/10.1021/ja076167a.

[14] B.J. Nordell, T.D. Nguyen, A.N. Caruso, S.S. Purohit, N.A. Oyler, W.A. Lanford, D.W. Gidley, J.T. Gaskins, P.E. Hopkins, P. Henry, S.W. King, M.M. Paquette, Carbon-Enriched Amorphous Hydrogenated Boron Carbide Films for Very-Low-k Interlayer Dielectrics, Adv. Electron. Mater. 3 (2017) 1700116, https://doi.org/10.1002/aelm.201700116.

[15] D.N. McIlroy, S.-D. Hwang, K. Yang, N. Remmes, P.A. Dowben, A.A. Ahmad, N.J. Ianno, J.Z. Li, J.Y. Lin, H.X. Jiang, The incorporation of Nickel and Phosphorus dopants into Boron-Carbon alloy thin films, Appl. Phys. A. 67 (1998) 335–342, https://doi.org/10.1007/s003390050780.

[16] R. Bao, D.B. Chrisey, D.J. Cherniak, Kinetics of hydrogen in preparing amorphous B5C:H thin films, J. Mater. Res. 26 (2011) 867–873, https://doi.org/DOI: 10.1557/jmr.2010.93.

[17] B.J. Nordell, C.L. Keck, T.D. Nguyen, A.N. Caruso, S.S. Purohit, W.A. Lanford, D. Dutta, D. Gidley, P. Henry, S.W. King, M.M. Paquette, Tuning the properties of a

complex disordered material: Full factorial investigation of PECVD-grown amorphous hydrogenated boron carbide, Mater. Chem. Phys. 173 (2016) 268–284, https://doi.org/10.1016/j.matchemphys.2016.02.013.

[18] B.J. Nordell, S. Karki, T.D. Nguyen, P. Rulis, A.N. Caruso, S.S. Purohit, H. Li, S.W. King, D. Dutta, D. Gidley, W.A. Lanford, M.M. Paquette, The influence of hydrogen on the chemical, mechanical, optical/electronic, and electrical transport properties of amorphous hydrogenated boron carbide, J. Appl. Phys. 118 (2015) 35703, https://doi.org/10.1063/1.4927037.

[19] S. Hwang, D. Byun, N.J. Ianno, P.A. Dowben, H.R. Kim, Fabrication of boron-carbide/boron heterojunction devices, Appl. Phys. Lett. 68 (1996) 1495–1497, https://doi.org/10.1063/1.116266.

[20] S. Lee, J. Mazurowski, G. Ramseyer, P.A. Dowben, Characterization of boron carbide thin films fabricated by plasma enhanced chemical vapor deposition from boranes, J. Appl. Phys. 72 (1992) 4925–4933, https://doi.org/10.1063/1.352060.

[21] G.G. Peterson, Y. Wang, N.J. Ianno, M. Nastasi, Modeling Changes in Measured Conductance of Thin Boron Carbide Semiconducting Films Under Irradiation, IEEE Trans. Nucl. Sci. 63 (2016) 2815–2822, https://doi.org/10.1109/TNS.2016.2626268.

[22] A.N. Caruso, R.B. Billa, S. Balaz, J.I. Brand, P.A. Dowben, The heteroisomeric diode, J. Phys. Condens. Matter. 16 (2004) L139–L146, https://doi.org/10.1088/0953-8984/16/10/l04.

[23] P. Chaudhari, N. Meshram, A. Singh, A. Topkar, R. Dusane, Hot wire chemical vapour deposition (HWCVD) of boron carbide thin films from ortho-carborane for neutron detection application, Thin Solid Films. 519 (2011) 4561–4564, https://doi.org/10.1016/j.tsf.2011.01.295.

[24] Q. An, K.M. Reddy, K.Y. Xie, K.J. Hemker, W.A. Goddard, New Ground-State Crystal Structure of Elemental Boron, Phys. Rev. Lett. 117 (2016) 85501, https://doi.org/10.1103/PhysRevLett.117.085501.

[25] L. V McCarty, J.S. Kasper, F.H. Horn, B.F. Decker, A.E. Newkirk, A NEW CRYSTALLINE MODIFICATION OF BORON, J. Am. Chem. Soc. 80 (1958) 2592,

https://doi.org/10.1021/ja01543a066.

[26] R.E. Hughes, C.H.L. Kennard, D.B. Sullenger, H.A. Weakliem, D.E. Sands, J.L. Hoard, The Structure of -Rhombohedral Boron, J. Am. Chem. Soc. 85 (1963) 361–362, https://doi.org/10.1021/ja00886a036.

[27] A.R. Oganov, J. Chen, C. Gatti, Y. Ma, Y. Ma, C.W. Glass, Z. Liu, T. Yu, O.O. Kurakevych, V.L. Solozhenko, Ionic high-pressure form of elemental boron, Nature. 457 (2009) 863–867, https://doi.org/10.1038/nature07736.

[28] E.D. Jemmis, M.M. Balakrishnarajan, Polyhedral Boranes and Elemental Boron: Direct Structural Relations and Diverse Electronic Requirements, J. Am. Chem. Soc. 123 (2001) 4324–4330, https://doi.org/10.1021/ja0026962.

[29] K. Persson, Materials Data on B (SG:166) by Materials Project, (2014), https://doi.org/10.17188/1191505.

[30] A.R. Oganov, V.L. Solozhenko, Boron: a hunt for superhard polymorphs, J. Superhard Mater. 31 (2009) 285, https://doi.org/10.3103/S1063457609050013.

[31] B.F. Decker, J.S. Kasper, The crystal structure of a simple rhombohedral form of boron, Acta Crystallogr. 12 (1959) 503–506. https://10.1107/S0365110X59001529.

[32] K. Katada, An Electron Diffraction Study Evaporated Boron Films, Jpn. J. Appl. Phys. 5 (1966) 582–587, https://doi.org/10.1143/jjap.5.582.

[33] M. Van Schilfgaarde, W.A. Harrison, Electronic structure of boron, J. Phys. Chem. Solids. 46 (1985) 1093–1100, https://doi.org/10.1016/0022-3697(85)90025-3.

[34] Domnich Vladislav, Reynaud Sara, Haber Richard A., M. Chhowalla, Boron Carbide: Structure, Properties, and Stability under Stress, J. Am. Ceram. Soc. 94 (2011) 3605–3628, https://doi.org/10.1111/j.1551-2916.2011.04865.x.

[35] H.K. Clark, J.L. Hoard, The Crystal Structure of Boron Carbide, J. Am. Chem. Soc. 65 (1943) 2115–2119, https://doi.org/10.1021/ja01251a026.

[36] D.M. Bylander, L. Kleinman, S. Lee, Self-consistent calculations of the energy bands and bonding properties of $B_{12}C_3$, Phys. Rev. B. 42 (1990) 1394–1403, https://doi.org/10.1103/PhysRevB.42.1394.

[37] S. Lee, D.M. Bylander, S.W. Kim, L. Kleinman, Computational search for the real tetragonal B50, Phys. Rev. B. 45 (1992) 3248–3251, https://doi.org/10.1103/PhysRevB.45.3248.

[38] D.R. Armstrong, J. Bolland, P.G. Perkins, G. Will, A. Kirfel, The nature of the chemical bonding in boron carbide. IV. Electronic band structure of boron carbide, B13C2, and three models of the structure $B_{12}C_3$, Acta Crystallogr. Sect. B. 39 (1983) 324–329. https://10.1107/S0108768183002487.

[39] S. Aydin, M. Simsek, Hypothetically superhard boron carbide structures with a $B_{11}C$ icosahedron and three-atom chain, Phys. Status Solidi. 246 (2009) 62–70, https://doi.org/10.1002/pssb.200844328.

[40] V.I. Ivashchenko, V.I. Shevchenko, P.E.A. Turchi, First-principles study of the atomic and electronic structures of crystalline and amorphous B_4C, Phys. Rev. B. 80 (2009) 235208.

[41] R. Bao, D.B. Chrisey, Short range order structure of amorphous B_4C boron carbide thin films, J. Mater. Sci. 46 (2011) 3952–3959, https://doi.org/10.1007/s10853-011-5320-3.

[42] I. Caretti, R. Gago, J.M. Albella, I. Jiménez, Boron carbides formed by coevaporation of B and C atoms: Vapor reactivity, B_xC_{1-x} composition, and bonding structure, Phys. Rev. B. 77 (2008) 174109.

[43] K. Shirai, S. Emura, S. Gonda, Y. Kumashiro, Infrared study of amorphous $B_{1-x}C_x$ films, J. Appl. Phys. 78 (1995) 3392.

[44] X.Q. Yan, W.J. Li, T. Goto, M.W. Chen, Raman spectroscopy of pressure-induced amorphous boron carbide, Appl. Phys. Lett. 88 (2006) 131905, https://doi.org/10.1063/1.2189826.

[45] D. Ghosh, G. Subhash, C.H. Lee, Y.K. Yap, Strain-induced formation of carbon and

boron clusters in boron carbide during dynamic indentation, Appl. Phys. Lett. 91 (2007) 61910, https://doi.org/10.1063/1.2768316.

[46] N. Dugan, Ş. Erkoç, Structural properties of boron carbide nanoparticles: Application of a new set of Stillinger–Weber parameters, Comput. Mater. Sci. 50 (2011) 2950–2954, https://doi.org/10.1016/J.COMMATSCI.2011.05.012.

[47] Z. Gamba, B.M. Powell, The condensed phases of carboranes, J. Chem. Phys. 105 (1996) 2436–2440, https://doi.org/10.1063/1.472111.

[48] J.J. Ott, B.M. Gimarc, Optimized Structures and Relative Stabilities of the Carboranes from Ab Initio Calculations, J. Comput. Chem. 7 (1986) 673–692, https://doi.org/10.1002/jcc.540070510.

[49] R.H. Baughman, NMR, Calorimetric, and Diffraction Study of Molecular Motion in Crystalline Carboranes, J. Chem. Phys. 53 (1970) 3781.

[50] R.N. Grimes, Chapter 9 - Icosahedral Carboranes: 1,2-C2B10H12, in: R.N.B.T.-C. (Third E. Grimes (Ed.), Academic Press, Boston, 2016: pp. 283–502, https://doi.org/10.1016/B978-0-12-801894-1.00009-3.

[51] K. Hermansson, M. Wójcik, S. Sjöberg, o-, m-, and p-Carboranes and Their Anions: Ab Initio Calculations of Structures, Electron Affinities, and Acidities, Inorg. Chem. 38 (1999) 6039–6048, https://doi.org/10.1021/ic9903811.

[52] D. Grafstein, J. Dvorak, Neocarboranes, a New Family of Stable Organoboranes Isomeric with the Carboranes, Inorg. Chem. 2 (1963) 1128–1133, https://doi.org/10.1021/ic50010a011.

[53] C.A. Brown, M.L. McKee, Rearrangements in icosahedral boranes and carboranes revisited, J. Mol. Model. 12 (2006) 653–664, https://doi.org/10.1007/s00894-006-0111-5.

[54] B. Dong, A. Oyelade, J.A. Kelber, Carborane-based polymers: a novel class of semiconductors with tunable properties, Phys. Chem. Chem. Phys. 19 (2017) 10986–10997, https://doi.org/10.1039/C7CP00835J.

[55] O.I. Buzhinsky, E.A. Azizov, A.M. Belov, S.A. Grashin, A. V Krasilnikov, I.A. Kovan, C. V Mirnov, A.A. Petrov, V.G. Petrov, D. V Portnov, T.S. Pulinets, A.N. Romannikov, A.A. Skvortsova, S.M. Sotnikov, S.N. Tugarinov, S.I. Fedorenko, A.P. Chernobaj, A.I. Kanaev, V.M. Sharapov, S.Y. Rybakov, A.E. Gorodetsky, A.P. Zakharov, A.A. Vasilyev, S.N. Luzganov, V.P. Fokin, A.N. Chulkov, A simple boronization technique for T-3M and T-11M tokamak chambers, J. Nucl. Mater. 191–194 (1992) 1413–1416, https://doi.org/10.1016/0022-3115(92)90708-S.

[56] S. Papetti, T.L. Heying, p-Carborane [1,12-Dicarbaclovododecaborane(12)], J. Am. Chem. Soc. 86 (1964) 2295, https://doi.org/10.1021/ja01065a045.

[57] V.K. Alimov, D.B. Bogomolov, M.N. Churaeva, A.E. Gorodetsky, S.L. Kanashenko, A.I. Kanaev, S.Y. Rybakov, V.M. Sharapov, A.P. Zakharov, R.K. Zalavutdinov, O.I. Buzhinsky, A.P. Chernobay, S.A. Grashin, S. V Mirnov, V.I. Bregadze, A.Y. Usyatinsky, Characterization of a-B/C: H films deposited from different boron containing precursors, J. Nucl. Mater. 196–198 (1992) 670–675, https://doi.org/10.1016/S0022-3115(06)80120-0.

[58] J. Winter, H.G. Esser, L. Könen, V. Philipps, H. Reimer, J. v. Seggern, J. Schlüter, E. Vietzke, F. Waelbroeck, P. Wienhold, T. Banno, D. Ringer, S. Vepřek, Boronization in textor, J. Nucl. Mater. 162–164 (1989) 713–723, https://doi.org/10.1016/0022-3115(89)90352-8.

[59] B. Sylvester, S.-H. Lin, B.J. Feldman, Doping vs alloying in amorphous hydrogenated boron carbide, Solid State Commun. 93 (1995) 969–971, https://doi.org/10.1016/0038-1098(94)00914-7.

[60] A. Annen, M. Saß, R. Beckmann, A. von Keudell, W. Jacob, Structure of plasma-deposited amorphous hydrogenated boron-carbon thin films, Thin Solid Films. 312 (1998) 147–155, https://doi.org/10.1016/S0040-6090(97)00735-9.

[61] J. Braddock-Wilking, S.-H. Lin, B.J. Feldman, 13C NMR Spectroscopy of Amorphous Hydrogenated Carbon and Amorphous Hydrogenated Boron Carbide, MRS Proc. 555 (1998) 401, https://doi.org/DOI: 10.1557/PROC-555-401.

[62] D. Byun, B.R. Spady, N.J. Ianno, P.A. Dowben, Comparison of different chemical vapor deposition methodologies for the fabrication of heterojunction boron-carbide diodes, Nanostructured Mater. 5 (1995) 465–471, https://doi.org/10.1016/0965-9773(95)00256-E.

[63] A.S. Anan'ev, O.I. Kon'kov, V.M. Lebedev, A.N. Novokhatski, E.I. Terukov, I.N. Trapeznikova, Fabrication and properties of amorphous hydrogenated boron carbide films, Semiconductors. 36 (2002) 941–943, https://doi.org/10.1134/1.1500477.

[64] D.L. Schulz, A. Lutfurakhmanov, B. Mayo, J. Sandstrom, D. Bunzow, S.B. Qadri, R. Bao, D.B. Chrisey, A.N. Caruso, Characterization of a-B5C:H prepared by PECVD of orthocarborane: Results of preliminary FTIR and nuclear reaction analysis studies, J. Non. Cryst. Solids. 354 (2008) 2369–2371, https://doi.org/10.1016/j.jnoncrysol.2007.10.077.

[65] R.B. Billa, T. Hofmann, M. Schubert, B.W. Robertson, Annealing effects on the optical properties of semiconducting boron carbide, J. Appl. Phys. 106 (2009) 33515, https://doi.org/10.1063/1.3190679.

[66] A.A. Ahmad, N.J. Ianno, P.G. Snyder, D. Welipitiya, D. Byun, P.A. Dowben, Optical properties of boron carbide (B5C) thin films fabricated by plasma-enhanced chemical-vapor deposition, J. Appl. Phys. 79 (1996) 8643–8647, https://doi.org/10.1063/1.362487.

[67] M.M. Paquette, W. Li, M. Sky Driver, S. Karki, A.N. Caruso, N.A. Oyler, The local physical structure of amorphous hydrogenated boron carbide: insights from magic angle spinning solid-state NMR spectroscopy, J. Phys. Condens. Matter. 23 (2011) 435002, https://doi.org/10.1088/0953-8984/23/43/435002.

[68] R. James, F.L. Pasquale, J.A. Kelber, Plasma-enhanced chemical vapor deposition ofortho-carborane: structural insights and interaction with Cu overlayers, J. Phys. Condens. Matter. 25 (2013) 355004, https://doi.org/10.1088/0953-8984/25/35/355004.

[69] S. Dhungana, T.D. Nguyen, B.J. Nordell, A.N. Caruso, M.M. Paquette, G. Chollon, W.A. Lanford, K. Scharfenberger, D. Jacob, S.W. King, Boron and high-k dielectrics: Possible fourth etch stop colors for multipattern optical lithography processing, J. Vac. Sci. Technol. A. 35 (2017) 21510, https://doi.org/10.1116/1.4974920.

[70] A. KANAEV I., S. RYBAKOV Yu., M. CHURAEVA N., EPMA and ellipsometric characterization of PECVD boron-carbon films, J. Phys. IV Fr. 03 (1993) C3-183-C3-188. https://10.1051/jp4:1993323.

[71] V.M. Sharapov, A.I. Kanaev, S.Y. Rybakov, L.E. Gavrilov, Erosion of a-B/C : H films under deuterium plasma irradiation, J. Nucl. Mater. 220–222 (1995) 930–933,

https://doi.org/10.1016/0022-3115(94)00614-8.

[72] E. Echeverria, B. Dong, G. Peterson, J.P. Silva, E.R. Wilson, M.S. Driver, Y.-S. Jun, G.D. Stucky, S. Knight, T. Hofmann, Z.-K. Han, N. Shao, Y. Gao, W.-N. Mei, M. Nastasi, P.A. Dowben, J.A. Kelber, Semiconducting boron carbides with better charge extraction through the addition of pyridine moieties, J. Phys. D. Appl. Phys. 49 (2016) 355302, https://doi.org/10.1088/0022-3727/49/35/355302.

[73] M. Imam, C. Höglund, S. Schmidt, R. Hall-Wilton, J. Birch, H. Pedersen, Plasma CVD of hydrogenated boron-carbon thin films from triethylboron, J. Chem. Phys. 148 (2018) 34701, https://doi.org/10.1063/1.5006886.

[74] B. Dong, A. Oyelade, N. Nandagopal, J.A. Kelber, Aromatic-doped boron carbide films formed by PECVD of metacarborane and aniline or pyridine: Chemical and electronic structure, Surf. Coatings Technol. 314 (2017) 45–50, https://doi.org/10.1016/j.surfcoat.2016.08.031.

[75] E. Rühl, N.F. Riehs, S. Behera, J. Wilks, J. Liu, H.-W. Jochims, A.N. Caruso, N.M. Boag, J.A. Kelber, P.A. Dowben, Photofragmentation of the closo-Carboranes Part II: VUV Assisted Dehydrogenation in the closo-Carboranes and Semiconducting B10C2Hx Films, J. Phys. Chem. A. 114 (2010) 7284–7291, https://doi.org/10.1021/jp103805r.

[76] M. Belhadj-Larbi, R.C. Horn, P. Rulis, Model creation and electronic structure calculation of amorphous hydrogenated boron carbide: a classical/ab initio hybrid approach, RSC Adv. 7 (2017) 46788–46795, https://doi.org/10.1039/C7RA06988J.

[77] B.J. Alder, T.E. Wainwright, Phase Transition for a Hard Sphere System, J. Chem. Phys. 27 (1957) 1208–1209, https://doi.org/10.1063/1.1743957.

[78] J.E. Jones, S. Chapman, On the determination of molecular fields. —II. From the equation of state of a gas, Proc. R. Soc. London. Ser. A, Contain. Pap. a Math. Phys. Character. 106 (1924) 463–477, https://doi.org/10.1098/rspa.1924.0082.

[79] A. Rahman, Correlations in the Motion of Atoms in Liquid Argon, Phys. Rev. 136 (1964) A405–A411, https://doi.org/10.1103/PhysRev.136.A405.

[80] A.R. Leach, Molecular Modelling PRINCIPLES AND APPLICATIONS, Pearson Education Limited, 2001.

[81] L. Verlet, Computer "Experiments" on Classical Fluids. I. Thermodynamical Properties of Lennard-Jones Molecules, Phys. Rev. 159 (1967) 98–103, https://doi.org/10.1103/PhysRev.159.98.

[82] R.W. Hockney, POTENTIAL CALCULATION AND SOME APPLICATIONS., Methods Comput. Phys. 9 135-211(1970). (1970). https://www.osti.gov/servlets/purl/4079632.

[83] W.C. Swope, H.C. Andersen, P.H. Berens, K.R. Wilson, A computer simulation method for the calculation of equilibrium constants for the formation of physical clusters of molecules: Application to small water clusters, J. Chem. Phys. 76 (1982) 637–649, https://doi.org/10.1063/1.442716.

[84] D. Beeman, Some multistep methods for use in molecular dynamics calculations, J. Comput. Phys. 20 (1976) 130–139, https://doi.org/10.1016/0021-9991(76)90059-0.

[85] J.M. Haile, Molecular Dynamics Simulation: Elementary Methods, 1st ed., John Wiley \& Sons, Inc., New York, NY, USA, 1992.

[86] D.C. Rapaport, The Art of Molecular Dynamics Simulation, 2nd ed., Cambridge University Press, Cambridge, 2004, https://doi.org/DOI: 10.1017/CBO9780511816581.

[87] R. Lesar, Introduction to Computational Materials Science Fundamentals to Applications, 1st ed., Cambridge University Press, 2013.

[88] S. Plimpton, P. Crozier, A. Thompson, LAMMPS-large-scale atomic/molecular massively parallel simulator, Sandia Natl. Lab. 18 (2007) 43.

[89] H.J.C. Berendsen, D. van der Spoel, R. van Drunen, GROMACS: A message-passing parallel molecular dynamics implementation, Comput. Phys. Commun. 91 (1995) 43–56, https://doi.org/10.1016/0010-4655(95)00042-E.

[90] J.D. Gale, GULP: A computer program for the symmetry-adapted simulation of solids, J. Chem. Soc. Faraday Trans. 93 (1997) 629–637, https://doi.org/10.1039/A606455H.

[91] J. Stadler, R. Mikulla, H.-R. Trebin, IMD: A Software Package for Molecular Dynamics Studies on Parallel Computers, Int. J. Mod. Phys. C. 08 (1997) 1131–1140, https://doi.org/10.1142/S0129183197000990.

[92] H. Watanabe, M. Suzuki, N. Ito, Efficient Implementations of Molecular Dynamics Simulations for Lennard-Jones Systems, Prog. Theor. Phys. 126 (2011) 203–235, https://doi.org/10.1143/PTP.126.203.

[93] J.C. Phillips, R. Braun, W. Wang, J. Gumbart, E. Tajkhorshid, E. Villa, C. Chipot, R.D. Skeel, L. Kalé, K. Schulten, Scalable molecular dynamics with NAMD, J. Comput. Chem. 26 (2005) 1781–1802, https://doi.org/10.1002/jcc.20289.

[94] F.H. Stillinger, T.A. Weber, Computer simulation of local order in condensed phases of silicon, Phys. Rev. B. 31 (1985) 5262–5271, https://doi.org/10.1103/PhysRevB.31.5262.

[95] F.F. Abraham, I.P. Batra, Theoretical interpretation of atomic-force-microscope images of graphite, Surf. Sci. 209 (1989) L125–L132, https://doi.org/10.1016/0039-6028(89)90053-8.

[96] P. Mahon, B.A. Pailthorpe, G.B. Bacskay, A quantum mechanical calculation of interatomic interactions in diamond, Philos. Mag. B. 63 (1991) 1419–1430, https://doi.org/10.1080/13642819108205571.

[97] P.B. Rasband, P. Clancy, B.W. Roberts, Tight-binding studies of the tendency for boron to cluster in c-Si. I. Development of an improved boron–boron model, J. Appl. Phys. 84 (1998) 2471–2475, https://doi.org/10.1063/1.368408.

[98] W.H. Moon, H.J. Hwang, A modified Stillinger–Weber empirical potential for boron nitride, Appl. Surf. Sci. 239 (2005) 376–380, https://doi.org/10.1016/J.APSUSC.2004.05.284.

[99] X. Deng, Y. Song, J. Li, Y. Pu, Parametrization of the Stillinger-Weber potential for Si/N/H system and its application to simulations of silicon nitride film deposition with

SiH_4/NH_3, J. Appl. Phys. 115 (2014) 54902, https://doi.org/10.1063/1.4863841.

[100] X.W. Zhou, R.E. Jones, K. Chu, Polymorphic improvement of Stillinger-Weber potential for InGaN, J. Appl. Phys. 122 (2017) 235703, https://doi.org/10.1063/1.5001339.

[101] X.W. Zhou, D.K. Ward, J.E. Martin, F.B. van Swol, J.L. Cruz-Campa, D. Zubia, Stillinger-Weber potential for the II-VI elements Zn-Cd-Hg-S-Se-Te, Phys. Rev. B. 88 (2013) 85309, https://doi.org/10.1103/PhysRevB.88.085309.

[102] S. Plimpton, Fast Parallel Algorithms for Short-Range Molecular Dynamics, J. Comput. Phys. 117 (1995) 1–19, https://doi.org/10.1006/jcph.1995.1039.

[103] L. Pizzagalli, J. Godet, J. Guénolé, S. Brochard, E. Holmstrom, K. Nordlund, T. Albaret, A new parametrization of the Stillinger–Weber potential for an improved description of defects and plasticity of silicon, J. Phys. Condens. Matter. 25 (2013) 55801, https://doi.org/10.1088/0953-8984/25/5/055801.

[104] A.C.T. Van Duin, S. Dasgupta, F. Lorant, W.A. Goddard, ReaxFF: a reactive force field for hydrocarbons, J. Phys. Chem. A. 105 (2001) 9396–9409.

[105] A.C.T. van Duin, A. Strachan, S. Stewman, Q. Zhang, X. Xu, W.A. Goddard, ReaxFFSiO Reactive Force Field for Silicon and Silicon Oxide Systems, J. Phys. Chem. A. 107 (2003) 3803–3811, https://doi.org/10.1021/jp0276303.

[106] K. Chenoweth, A.C.T. Van Duin, W.A. Goddard, ReaxFF reactive force field for molecular dynamics simulations of hydrocarbon oxidation, J. Phys. Chem. A. 112 (2008) 1040–1053.

[107] M.F. Russo, A.C.T. van Duin, Atomistic-scale simulations of chemical reactions: Bridging from quantum chemistry to engineering, Nucl. Instruments Methods Phys. Res. Sect. B Beam Interact. with Mater. Atoms. 269 (2011) 1549–1554, https://doi.org/10.1016/j.nimb.2010.12.053.

[108] S.-Y. Kim, N. Kumar, P. Persson, J. Sofo, A.C.T. van Duin, J.D. Kubicki, Development of a ReaxFF Reactive Force Field for Titanium Dioxide/Water Systems, Langmuir. 29 (2013) 7838–7846, https://doi.org/10.1021/la4006983.

[109] T.P. Senftle, S. Hong, M.M. Islam, S.B. Kylasa, Y. Zheng, Y.K. Shin, C. Junkermeier, R. Engel-Herbert, M.J. Janik, H.M. Aktulga, The ReaxFF reactive force-field: development, applications and future directions, Npj Comput. Mater. 2 (2016) 15011.

[110] Q. An, W.A. Goddard, Atomistic Origin of Brittle Failure of Boron Carbide from Large-Scale Reactive Dynamics Simulations: Suggestions toward Improved Ductility, Phys. Rev. Lett. 115 (2015) 105501, https://doi.org/10.1103/PhysRevLett.115.105501.

[111] A.C.T. van Duin, J.M.A. Baas, B. van de Graaf, Delft molecular mechanics: a new approach to hydrocarbon force fields. Inclusion of a geometry-dependent charge calculation, J. Chem. Soc. Faraday Trans. 90 (1994) 2881–2895, https://doi.org/10.1039/FT9949002881.

[112] LAMMPS User Documentation, (n.d.). https://lammps.sandia.gov/doc/minimize.html.

[113] P. Comba, T. Hambley, B. Martin, Computation, Mol. Model. Inorg. Compd. (2009) 61–68, https://doi.org/doi:10.1002/9783527628124.ch4.

[114] A. Antoniou, W.-S. Lu, eds., The Optimization Problem BT - Practical Optimization: Algorithms and Engineering Applications, in: Springer US, Boston, MA, 2007: pp. 1–26, https://doi.org/10.1007/978-0-387-71107-2_1.

[115] R. Fletcher, Practical Methods of Optimization, 2nd ed., Wiley & Sons, New York, NY, USA, 1980.

[116] W.H. Press, S.A. Teukolsky, W.T. Vetterling, B.P. Flannery, The Art of Scientific Computing, 3rd ed., New York, NY, USA, 2007.

[117] G. Opletal, T.C. Petersen, B. O'Malley, I.K. Snook, D.G. McCulloch, I. Yarovsky, HRMC_1.1: Hybrid Reverse Monte Carlo method with silicon and carbon potentials, Comput. Phys. Commun. 182 (2011) 542, https://doi.org/10.1016/J.CPC.2010.10.023.

[118] T. Petersen, B. O'Malley, I. Snook, D.G. McCulloch, N.A. Marks, I. Yarovsky, Hybrid approach for generating realistic amorphous carbon structure using metropolis and reverse Monte Carlo AU - Opletal, George, Mol. Simul. 28 (2002) 927–938, https://doi.org/10.1080/089270204000002584.

[119] T. Petersen, I. Yarovsky, I. Snook, D.G. McCulloch, G. Opletal, Structural analysis of carbonaceous solids using an adapted reverse Monte Carlo algorithm, Carbon N. Y. 41 (2003) 2403–2411, https://doi.org/10.1016/S0008-6223(03)00296-3.

[120] G. Opletal, T.C. Petersen, D.G. McCulloch, I.K. Snook, I. Yarovsky, The structure of disordered carbon solids studied using a hybrid reverse Monte Carlo algorithm, J. Phys. Condens. Matter. 17 (2005) 2605–2616, https://doi.org/10.1088/0953-8984/17/17/008.

[121] G. Opletal, T.C. Petersen, I.K. Snook, D.G. McCulloch, Modeling of structure and porosity in amorphous silicon systems using Monte Carlo methods, J. Chem. Phys. 126 (2007) 214705, https://doi.org/10.1063/1.2743029.

[122] G. Opletal, T.C. Petersen, I.K. Snook, S.P. Russo, HRMC_2.0: Hybrid Reverse Monte Carlo method with silicon, carbon and germanium potentials, Comput. Phys. Commun. 184 (2013) 1946–1957, https://doi.org/10.1016/j.cpc.2013.03.004.

[123] G. Opletal, T.C. Petersen, B. O'Malley, I.K. Snook, D.G. McCulloch, I. Yarovsky, HRMC: Hybrid Reverse Monte Carlo method with silicon and carbon potentials, Comput. Phys. Commun. 178 (2008) 777–787, https://doi.org/10.1016/J.CPC.2007.12.007.

[124] P.B. Rasband, P. Clancy, M.O. Thompson, Equilibrium concentrations of defects in pure and B-doped silicon, J. Appl. Phys. 79 (1996) 8998–9011, https://doi.org/10.1063/1.362632.

[125] Y. Şimsek, Ş. Erkoç, Structural Properties of Monolayer Boron Carbide Nanoribbons Under Strain: Molecular Dynamics Simulations, J. Comput. Theor. Nanosci. 12 (n.d.) 2180–2188. https://www.ingentaconnect.com/content/asp/jctn/2015/00000012/00000009/art00025.

[126] L. Martínez, R. Andrade, E.G. Birgin, J.M. Martínez, PACKMOL: A package for building initial configurations for molecular dynamics simulations, J. Comput. Chem. 30 (2009) 2157–2164, https://doi.org/10.1002/jcc.21224.

[127] A.H. Farmahini, G. Opletal, S.K. Bhatia, Structural Modelling of Silicon Carbide-Derived Nanoporous Carbon by Hybrid Reverse Monte Carlo Simulation, J. Phys. Chem. C. 117 (2013) 14081–14094, https://doi.org/10.1021/jp403929r.

[128] T.X. Nguyen, S.K. Bhatia, S.K. Jain, K.E. Gubbins, Hybrid Reverse Monte Carlo Reconstruction and Simulation Studies, in: 2006 Int. Conf. Nanosci. Nanotechnol., 2006: p. 1, https://doi.org/10.1109/ICONN.2006.340708.

[129] G. Opletal, T.C. Petersen, A.S. Barnard, S.P. Russo, On reverse Monte Carlo constraints and model reproduction, J. Comput. Chem. 38 (2017) 1547–1551, https://doi.org/10.1002/jcc.24799.

[130] X. Wu, J. Dai, Y. Zhao, Z. Zhuo, J. Yang, X.C. Zeng, Two-Dimensional Boron Monolayer Sheets, ACS Nano. 6 (2012) 7443–7453, https://doi.org/10.1021/nn302696v.

[131] D.L.V.K. Prasad, E.D. Jemmis, Stuffing Improves the Stability of Fullerenelike Boron Clusters, Phys. Rev. Lett. 100 (2008) 165504, https://doi.org/10.1103/PhysRevLett.100.165504.

[132] T.B. Tai, M.T. Nguyen, A new chiral boron cluster B_{44} containing nonagonal holes, Chem. Commun. 52 (2016) 1653–1656, https://doi.org/10.1039/C5CC09111J.

[133] D. Berthelot, Sur le mélange des gaz, Comptes Rendus Hebd. Des Séances. 126 (1898) 1703–1855.

[134] LAMMPS Pair Styles, (2019). https://lammps.sandia.gov/doc/pair_sw.html (accessed January 5, 2019).

[135] K. Persson, Materials Data on B_4C (SG:166) by Materials Project, (2016), https://doi.org/10.17188/1285041.

[136] K. Persson, Materials Data on $B_{13}C_2$ (SG:166) by Materials Project, (2014), https://doi.org/10.17188/1276602.

[137] R. Bao, D.B. Chrisey, Short range order structure of amorphous B_4C boron carbide thin films, J. Mater. Sci. 46 (2011) 3952–3959, https://doi.org/10.1007/s10853-011-5320-3.

[138] A. Bouzid, S. Le Roux, G. Ori, M. Boero, C. Massobrio, Origin of structural analogies and differences between the atomic structures of $GeSe_4$ and GeS_4 glasses: A first

principles study, J. Chem. Phys. 143 (2015) 34504, https://doi.org/10.1063/1.4926830.

[139] M. Celino, S. Le Roux, G. Ori, B. Coasne, A. Bouzid, M. Boero, C. Massobrio, First-principles molecular dynamics study of glassy GeS_2:Atomic structure and bonding properties, Phys. Rev. B. 88 (2013) 174201, https://doi.org/10.1103/PhysRevB.88.174201.

[140] Z. Chaker, G. Ori, C. Tugène, S. Le Roux, M. Boero, C. Massobrio, E. Martin, A. Bouzid, The role of dispersion forces on the atomic structure of glassy chalcogenides: The case of $GeSe_4$ and GeS_4, J. Non. Cryst. Solids. 499 (2018) 167–172, https://doi.org/10.1016/j.jnoncrysol.2018.07.012.

[141] Y. Sakaguchi, T. Hanashima, K. Ohara, A.-A.A. Simon, M. Mitkova, Structural transformation in Ge_xS_{100-x} ($10<x<40$) network glasses: Structural varieties in short-range, medium-range, and nanoscopic scale, Phys. Rev. Mater. 3 (2019) 35601, https://doi.org/10.1103/PhysRevMaterials.3.035601.

[142] N. Baishnab, Synthesis of Amorphous Hydrogenated Boron Carbide from Orthocarborane Using Argon Bombardment: A Reaxff Molecular Dynamics Study, Missouri State University, 2019. https://bearworks.missouristate.edu/theses/3416.

[143] N. Fueki, T. Usuki, S. Tamaki, H. Okazaki, Y. Waseda, Structure of Amorphous Ge–S System by X-Ray Diffraction, J. Phys. Soc. Japan. 61 (1992) 2814–2820, https://doi.org/10.1143/JPSJ.61.2814.

[144] D. Simeone, C. Mallet, P. Dubuisson, G. Baldinozzi, C. Gervais, J. Maquet, Study of boron carbide evolution under neutron irradiation by Raman spectroscopy, J. Nucl. Mater. 277 (2000) 1.

[145] A.A. Babaev, Short- and medium-range order in disordered systems, Bull. Russ. Acad. Sci. Phys. 74 (2010) 677–679, https://doi.org/10.3103/S1062873810050266.

APPENDIX

SW Potential Optimization Scripts

Optimization Script

```
#!/bin/bash
#------------ Script for running energy minimization in LAMMPS for various values of sigma -
#------------ Using for loop to change the sigma values from 1.15 to 1.80 ----------------------------
for i in 1.15   1.16    1.17    1.18    1.19    1.20    1.21    1.22    1.23    1.24    1.25
1.26    1.27    1.28    1.29    1.30    1.31    1.32    1.33    1.34    1.35    1.36    1.37
1.38    1.39    1.40    1.41    1.418   1.42    1.43    1.44    1.45    1.46    1.47    1.48
1.49    1.50    1.51    1.52    1.53    1.54    1.55    1.56    1.57    1.58    1.59    1.60
1.61    1.62    1.63    1.64    1.65    1.66    1.67    1.68    1.69    1.70    1.71    1.72
1.73    1.74    1.75    1.76    1.77    1.78    1.79    1.80
do
cat >B4C_Dugan_et.al_Original_SW.sw <<!
#       eps   sigma   a     lambda gamma  cos(theta)  A     B      p       q    tol
B B B 1.0000 $i 1.8179 1.0007 0.3241 -0.33333 13.4487 0.0848  4.0000  0.0000  0.0000
!
#------------------------------------------- Run LAMMPS ----------------------------------------------
echo `lmp_daily -in in.BC >> logfile.dat`               # Execute LAMMPS in ubuntu
mv dump_minimized.dat dump_minimized.$i.dat     # Renaming each dump file
mv xyz_minimized.lmp xyz_minimized_$i.lmp       # Renaming each minimized structures
echo "Minimization process sigma=$i complete"       # Displaying no. of minimization process
done
```

```
mkdir DUMP                                          # Make a DUMP directory

mkdir Minimized_Structures                          # Make a Minimized_Structures directory

mv dump* DUMP                                       # Move all the dump files to DUMP

mv xyz_minimized* Minimized_Structures              # Move all the minimized structures

#---------------------------------------------- The End -----------------------------------------------------
```

SW Potential Energy Minimization Input File

```
#------------------- SW Potential energy minimization input file ---------------------------------------

units               metal                           # Unit type for SW

atom_style          atomic                          # Atomic style for SW

read_data           Structure_file_name.lmp         # Add data file


# ------------------------------------ Calling the potential file-------------------------------------------

pair_style           sw                             # SW potential style

pair_coeff           * * Potential_file_name.sw B   # Add potential file

mass                 1 10.811                       # Mass of Boron atom

velocity             all create 0 4928459 rot yes dist gaussian

#-----------------------------------------Thermo-------------------------------------------------------

thermo               1                              # Save every step

thermo_style         custom step fnorm pe etotal press vol temp

#-------------------------------------------------------------------------------------------------------

neighbor             0.3 bin

neigh_modify         every 2 delay 0 check no

# --------------------------- Running Energy minimization simulation-----------------------------------
```

```
timestep        0.0005                          # In picoseconds
dump            1 all atom 100 dump_minimized.dat
min_style       cg                              # Conjugate gradient
minimize        0.0 1.0e-8 100000 1000000       # Minimization criteria
write_data      xyz_minimized.lmp               # Write final structure
#---------------------------------- The End -------------------------------------------------------
```

LAMMPS Scripts

Amorphous Boron Carbide ReaxFF

```
#---------------- REAX potential for BC system-----------------------------------------------------
#----------------Defining_Units&atomic_style-----------------------------------------------------
units           real
atom_style      charge
#----------------Loading_structure---------------------------------------------------------------
read_data       BxC_Structure_input.lmp     # Input file name for B12-CCC
#                                             , B12-CBC, B11C-CBC
#----------------Reading_potential---------------------------------------------------------------
pair_style      reax/c control_file_name    # Add LAMMPS control file name
pair_coeff      * * ffield.reax.hcb B C     # Reax Potential file name
#----------------Masses_and_initial_velocity_for_atoms-------------------------------------------
mass 1          10.811                      # Mass of Boron
mass 2          12.0107                     # Mass of Carbon
velocity        all create 300.0 4928459 rot yes dist gaussian
#----------------Thermo--------------------------------------------------------------------------
```

```
thermo          100
thermo_style    custom step temp pe etotal press vol pxx pyy pzz lx ly lz xy xz yz
neighbor        0.3 bin
neigh_modify    every 10 delay 0 check no
restart         5000 restart.*.dens17
#----------------Dumping_the_movie_file-------------------------------------------------------------
timestep        0.25
dump            1 all atom 100 dump_file_name.xyz
#----------------Simulation scheme ------------------------------------------------------------------
fix             1 all qeq/reax 1 0.0 10.0 1e-6 param_bc.qeq
fix             2 all npt temp 10 300 100 iso 0.0 0.0 1000
run             170000
unfix           2
fix             3 all npt temp 300 300 100 iso 0.0 0.0 1000
run             330000
unfix           3
#-------------------------------------------The_End-----------------------------------------------
```

Amorphous Boron Carbide New SW

```
#-------------------------------------New SW potential for BC system-----------------------------
#-------------------------------------Defining_Units&atomic_style--------------------------------
units           metal
atom_style      atomic
#-------------------------------------Loading_structure------------------------------------------
```

```
read_data          BxC_Structure_input.lmp       # Input file name for B12-CCC, B12-CBC
#----------------------------------------Reading_potential-------------------------------------------------
pair_style         sw
pair_coeff         * * New_SW_Potential_file_name.sw B C
#-----------------------------------Masses_and_initial_velocity_for_atoms-----------------------------
mass               1 10.811                  # Mass of Boron
mass               2 12.0107                 # Mass of Carbon
velocity           all create 300 4928459 rot yes dist gaussian
#----------------------------------------Thermo-----------------------------------------------------------
thermo             100
thermo_style       custom step temp pe etotal press vol pxx pyy pzz lx ly lz xy xz yz
neighbor           0.3 bin
neigh_modify       every 2 delay 0 check no
restart            50000 restart.*.dens17
#---------------------------------------Time_is_in_picosecond---------------------------------------------
timestep           0.0001
dump               1 all atom 500 dump_Part_X1.dat
#-------------------------------------- Simulation Scheme ----------------------------------------------
fix                1 all nvt temp 300.0 300.0 100.0
run                500000
unfix              1
fix                2 all npt temp  500 500 100 aniso 0 0 1000
run                1500000
```

```
unfix           2
fix             3 all npt temp  500 500 100 aniso 100000 100000 1000
run             1000000
unfix           3
#---------------------------------------------Minimize-----------------------------------------------
min_style       cg
minimize        0.0 1.0e-8 5000 100000
#------------------------------------------------------------------------------------------------------
fix             4 all npt temp  500 500 100 aniso 0 0 1000
run             1500000
unfix           4
fix             5 all npt temp  500 500 100 aniso 200000 200000 1000
run             500000
unfix           5
#---------------------------------------------Minimize-----------------------------------------------
min_style       cg
minimize        0.0 1.0e-8 5000 100000
#------------------------------------------------------------------------------------------------------
fix             6 all npt temp  300 300 100 aniso 0 0 1000
run             1000000
unfix           6
#-----------------------------------------The_End----------------------------------------------------
```

Amorphous Hydrogenated Boron Carbide ReaxFF

```
#-----------------------------------REAX potential for BC system ------------------------------------
#-----------------------------------Defining_Units&atomic_style-------------------------------------
units               real
atom_style      charge
#-----------------------------------Loading_structure-----------------------------------------------
read_data       initial_starting_configuration.lmp
#-----------------------------------Reading_potential-----------------------------------------------
pair_style      reax/c lmp_control
pair_coeff      * * ffield.reax.hcb B C H
#-----------------------------------Masses_and_initial_velocity_for_atoms---------------------------
mass 1          10.811
mass 2          12.0107
mass 3          1.008
velocity        all create 300.0 4928459 rot yes dist gaussian
#-----------------------------------Thermo----------------------------------------------------------
thermo              100
thermo_style    custom step temp pe etotal press vol pxx pyy pzz lx ly lz xy xz yz
neighbor            0.3 bin
neigh_modify    every 10 delay 0 check no
restart             5000 restart.*.dens17
#-----------------------------------Dumping_the_movie_file------------------------------------------
timestep            0.25
dump                1 all atom 150 dump_Part-X.xyz
```

```
#-----------------------------------Simulation_type_NVT_Maintain_the_box-------------------------
fix             1 all nvt temp 300.0 300.0 100.0
fix             2 all qeq/reax 1 0.0 10.0 1e-6 param_bch.qeq
run             50000
unfix           1
#-----------------------------------Simulation_type_NPT-Densification----------------------------
fix             3 all npt temp  500 500 100 aniso 300000.0 300000.0 100
run             25000                           # Pressure varied from 80K to 700K
unfix           3
#-----------------------------------Potential_Energy_Minimization--------------------------------
min_style    cg
minimize     0.0 1.0e-8 5000 100000
#-----------------------------------NPT_Pressure_Release-----------------------------------------
fix             4 all npt temp  300 300 100 aniso 0.0 0.0 100
run             25000
unfix           4
#-----------------------------------------The_End------------------------------------------------
```

NCPac script

```
#!/bin/bash
################################################################################
# To use this script make 2 flolders named "xyz_files" and "Characterization"  #
# Put this script in the "Characterization" floder                             #
# Inside "xyz_files" put xyz files, NCPac.inp, NCPac.exe                       #
```

```
# Replace these two lines inside NCPac.inp                                                    #
# infile            - name of xyz input file                          [in_filexyz]           #
# nax nay naz       - x,y,z cell length (Angstrom) (used if in_pbc_option=1)   [in_xl,in_yl,in_zl]  #
# Now you can make this script executable using : chmod 777 name.sh                           #
# This script extracts g(r), S(Q), Bond length, bond count, bond angle, coordination no.      #
# Script by: Rajan Khadka, Bikash Timalsina                                                   #
#---------------------------------------------------------------------------------------------------------#
NO_OF_FILES=`ls ../xyz_files | grep xyz |  wc -l`
for (( i=1; i<=$NO_OF_FILES; i++ ))
do
file=`ls ../xyz_files | grep xyz | sed -n ${i}p`
folder=`echo $file | sed -r 's/.{4}$//'`
mkdir $folder
cp ../xyz_files/$file ./$folder
cp ../xyz_files/NCPac.inp ./$folder
cp ../xyz_files/NCPac.exe ./$folder
var1=`sed -n 2p ./$folder/$file | awk -F "\"" '{print $2}' | awk -F " " '{print $1}'`
var2=`sed -n 2p ./$folder/$file | awk -F "\"" '{print $2}' | awk -F " " '{print $5}'`
var3=`sed -n 2p ./$folder/$file | awk -F "\"" '{print $2}' | awk -F " " '{print $9}'`
var11=`echo "$var1+0.1" | bc -l`
var22=`echo "$var2+0.1" | bc -l`
var33=`echo "$var3+0.1" | bc -l`
sed -i "s/infile/$file/" ./$folder/NCPac.inp
```

```
sed -i "s/nax/$var11/" ./$folder/NCPac.inp
sed -i "s/nay/$var22/" ./$folder/NCPac.inp
sed -i "s/naz/$var33/" ./$folder/NCPac.inp
cd ./$folder
./NCPac.exe ./NCPac.inp > logs
echo "completed processing file: $i/$NO_OF_FILES"
sleep 2s
echo "Creating bond directories ..."
if [ ! -d "../Bond_Length" ];
then
mkdir ../Bond_Length
touch ../Bond_Length/od_BOND_length.dat
fi
if [ ! -d "../Bond_Types" ];
then
mkdir ../Bond_Types
touch ../Bond_Types/od_BOND_types.dat
fi
if [ ! -d "../Bond_Classify" ];
then
mkdir ../Bond_Classify
touch ../Bond_Classify/od_CLASSIFY.dat
fi
```

```
if [ ! -d "../Bond_COORD" ];
then
mkdir ../Bond_COORD
touch ../Bond_COORD/od_COORD.dat
fi
if [ ! -d "../Bond_SQ" ];
then
mkdir ../Bond_SQ
touch ../Bond_SQ/od_SQ.dat
fi
if [ ! -d "../Bond_G3" ];
then
mkdir ../Bond_G3
touch ../Bond_G3/od_G3.dat
touch ../Bond_G3/od_G3_Total.dat
touch ../Bond_G3/od_G3_111.dat
touch ../Bond_G3/od_G3_112.dat
touch ../Bond_G3/od_G3_113.dat
touch ../Bond_G3/od_G3_122.dat
touch ../Bond_G3/od_G3_123.dat
touch ../Bond_G3/od_G3_133.dat
touch ../Bond_G3/od_G3_211.dat
touch ../Bond_G3/od_G3_212.dat
```

```
touch ../Bond_G3/od_G3_213.dat
touch ../Bond_G3/od_G3_222.dat
touch ../Bond_G3/od_G3_223.dat
touch ../Bond_G3/od_G3_233.dat
touch ../Bond_G3/od_G3_311.dat
touch ../Bond_G3/od_G3_312.dat
touch ../Bond_G3/od_G3_313.dat
touch ../Bond_G3/od_G3_322.dat
touch ../Bond_G3/od_G3_323.dat
touch ../Bond_G3/od_G3_333.dat
fi
if [ ! -d "../Bond_G2" ];
then
mkdir ../Bond_G2
touch ../Bond_G2/od_G2.dat
touch ../Bond_G2/od_G2_Total.dat
touch ../Bond_G2/od_G2_11.dat
touch ../Bond_G2/od_G2_12.dat
touch ../Bond_G2/od_G2_13.dat
touch ../Bond_G2/od_G2_22.dat
touch ../Bond_G2/od_G2_23.dat
touch ../Bond_G2/od_G2_33.dat
fi
```

```
echo "Bond directories created. Writing to bond directories"
sed -n 3p ./od_BOND_length.dat >> ../Bond_Length/od_BOND_length.dat
sed -n 3p ./od_BOND_types.dat >> ../Bond_Types/od_BOND_types.dat
sed -n 3p ./od_CLASSIFY.dat >> ../Bond_Classify/od_CLASSIFY.dat
sed -n 3,6p ./od_COORD.dat >> ../Bond_COORD/od_COORD.dat
sed -n 3p ./od_SQ.dat >> ../Bond_SQ/od_SQ.dat
sed -n 3,21p ./od_G3.dat >> ../Bond_G3/od_G3.dat
sed -n 3p ./od_G3.dat >> ../Bond_G3/od_G3_Total.dat
sed -n 4p ./od_G3.dat >> ../Bond_G3/od_G3_111.dat
sed -n 5p ./od_G3.dat >> ../Bond_G3/od_G3_112.dat
sed -n 6p ./od_G3.dat >> ../Bond_G3/od_G3_113.dat
sed -n 7p ./od_G3.dat >> ../Bond_G3/od_G3_122.dat
sed -n 8p ./od_G3.dat >> ../Bond_G3/od_G3_123.dat
sed -n 9p ./od_G3.dat >> ../Bond_G3/od_G3_133.dat
sed -n 10p ./od_G3.dat >> ../Bond_G3/od_G3_211.dat
sed -n 11p ./od_G3.dat >> ../Bond_G3/od_G3_212.dat
sed -n 12p ./od_G3.dat >> ../Bond_G3/od_G3_213.dat
sed -n 13p ./od_G3.dat >> ../Bond_G3/od_G3_222.dat
sed -n 14p ./od_G3.dat >> ../Bond_G3/od_G3_223.dat
sed -n 15p ./od_G3.dat >> ../Bond_G3/od_G3_233.dat
sed -n 16p ./od_G3.dat >> ../Bond_G3/od_G3_311.dat
sed -n 17p ./od_G3.dat >> ../Bond_G3/od_G3_312.dat
sed -n 18p ./od_G3.dat >> ../Bond_G3/od_G3_313.dat
```

```
sed -n 19p ./od_G3.dat >> ../Bond_G3/od_G3_322.dat

sed -n 20p ./od_G3.dat >> ../Bond_G3/od_G3_323.dat

sed -n 21p ./od_G3.dat >> ../Bond_G3/od_G3_333.dat

sed -n 2,9p ./od_G2.dat >> ../Bond_G2/od_G2.dat

sed -n 3p ./od_G2.dat >> ../Bond_G2/od_G2_Total.dat

sed -n 4p ./od_G2.dat >> ../Bond_G2/od_G2_11.dat

sed -n 5p ./od_G2.dat >> ../Bond_G2/od_G2_12.dat

sed -n 6p ./od_G2.dat >> ../Bond_G2/od_G2_13.dat

sed -n 7p ./od_G2.dat >> ../Bond_G2/od_G2_22.dat

sed -n 8p ./od_G2.dat >> ../Bond_G2/od_G2_23.dat

sed -n 9p ./od_G2.dat >> ../Bond_G2/od_G2_33.dat

sleep 3s

cd ..

done

#-----------------------------------------------The End-----------------------------------------------------
```